Investigation of Effect of Temperature and Forming Speed on the Formability of AA3003 Brazing Sheets

by

Ekta Jain

A thesis

presented to the University of Waterloo

in fulfilment of the

thesis requirement for the degree of

Master of Applied Science

in

Mechanical Engineering

Waterloo, Ontario, Canada, 2016

Author’s Declaration

I hereby declare that I am the sole author of this thesis. This is a true copy of the thesis, including any required final revisions, as accepted by my examiners.

I understand that my thesis may be electronically available to the public.

Abstract

The present work investigates the effect of forming temperature and forming speed on the formability of AA3003 aluminum alloy brazing sheet in three temper conditions (O, H22 and H24) and two different thicknesses (0.2 and 0.5 mm). Limiting Dome Height (LDH) experiments were conducted from which Forming Limit Curves (FLCs) were developed using the "linear best fit time-dependent method" (due to Volk and Hora, 2010) at room temperature (RT), 150 °C, 200 °C and 250 °C and forming speeds of 0.4 and 1.6 mm/s.

Limiting dome height (LDH) experiments performed on 0.5 mm O temper AA3003 brazing sheet showed an increase in the biaxial dome height (from 29.3 mm to 38 mm) for an increase in temperature from RT to 250 °C, a 28% increase. For the thinner 0.2 mm material, the corresponding improvement in LDH for the same temperature increase was 30%, 29% and 26% for the O, H22 and H24 tempers, respectively.

The measured FLCs were found to decrease with a decrease in sheet thickness and with increases in the initial hardness (temper). The plane strain limit strain (FLC-0 strain) of the O temper materials decreased by 24% at RT and 35% at 250 °C, when the thickness is reduced from 0.5 mm to 0.2 mm. For the 0.2 mm H22 and H24 materials, the RT FLC-0 strains are observed to be 31% and 39% lower than that of 0.2 mm O temper sheet. At 250 °C the respective drop in FLC-0 for the two tempers are 39% and 48%, respectively.

The increase in forming speed from 0.4 mm/s to 1.6 mm/s had very little effect on forming limits at RT, but resulted in a 6-9% drop in the FLCs at 250 °C.

M-K analyses were used to predict the FLCs. It was found that the M-K model is able to capture the temperature dependent formability behavior for the considered brazing sheets when the forming temperature increased from RT to 250 °C. However, the effect of punch speed is not captured as well and this is thought to be a function of the adopted Voce-based material model.

Acknowledgements

I would like to thank and show my great regards to my supervisor Prof. Michael Worswick for his continuous encouragement and effective guidance throughout my program. His insight into project topic and related issues became a great driving force towards the completion of project. Working under him was a great learning experience for me, both academically and intellectually. He will always be my mentor in all aspects of my life.

Distinct recognition is due for Dr. Srihari Kurukuri, Research Associate at Forming and Impact Mechanics Research group for his endless patience and outstanding assistance during the project. The time-dependent methods and numerical modelling work presented in this thesis benefited immensely from his help and guidance.

My special thanks go to Eckhard Budziarek, Jeff Wemp, Tom Gavel and Andy Barber for their great support in the high pressure laboratory and helping me through diverse aspects of my experimental needs. I profusely thank to all my colleagues and group members: Dr. Clifford Butcher, Dr. Jose Imbert, Nikky Pathak, Sante DiCecco, Rohit Verma, Armin Abedini, Tamjeed Rahmaan and Kaab Omer, for maintaining a friendly and healthy working environment within our group. I will always be proud for being a part of this significant family.

I am very thankful to the financial support of this research provided by DANA Canada Corporation, CanmetMATERIALS, Automotive Partnership Canada (APC), the Natural Sciences and Engineering Research Council (NSERC), the Canada foundation for Innovation (CIF) and the Ontario Research Fund (ORF). I express my sincere thanks to Dr. Sooky Winkler and Dr. Mark Kozdras of DANA Canada for their industrial expertise, assistance and encouragement throughout the project.

Words fail when it comes to acknowledge my parents and my elder brother, who always showed a great faith over me for my best performance out from my capabilities. Their endless love and care always gave me the strength to reach my goals. Finally, I would like to give my warm regards to my other family members and friends for their enormous support. I will cherish forever the delightful and pleasurable moments from my Waterloo life.

Ekta Jain

Dedication

To my parents,

Table of Contents

List of Figures

List of Tables

Chapter 1
Introduction

In order to address increasing environmental concerns, the governments of North America and Europe have established specific targets for fuel efficiency, to reduce the exhaust emissions from vehicles. For instance, the U.S. government has directed an enhancement in the average automobile fuel efficiency from 27.5 miles per gallon in 2012 to 54.4 miles per gallon in 2025 (www.nhtsa.gov). Similarly, the aim of European governments is to reduce average vehicular emissions from 130 grams of carbon dioxide per kilometer in 2015 to 95 grams of carbon dioxide per kilometer by 2021 (www.aluminiumleader.com). Therefore, automotive manufacturers have been considering various approaches to generate more fuel efficiency and one of them is reducing the weight of their cars. Steel was known to be the leading candidate in the automotive applications since 1920s (Cole and Sherman, 1995). Recently, there has been an escalating debate over the use of steel versus aluminum alloys in the automotive manufacturing industry. Some of the prominent physical properties of aluminum alloys such as low density and moderate strength (as compared to steel) have encouraged the use of aluminum as a suitable replacement for mild steel (Miller et al., 2000). At present, aluminum and its alloys have been increasingly used to produce internal car parts such as wheels, bumpers, suspension parts, transmission bodies and also external body parts such as hoods, doors and frames and therefore the market share for aluminum in cars is increasing. Figure 1.1 shows several applications of aluminum alloys within passenger vehicles but one of the important applications of aluminum alloys lies within heat exchangers (Figure 1.2).

One application of aluminum alloys, the focus of the current research, is within automotive thermal management systems. Figure 1.2 shows a typical heat exchanger construction which comprises stamped "core plates" which are stacked and brazed to fabricate the heat exchanger assembly. Aluminum alloys have been the material of choice within heat exchangers because of their excellent corrosion resistance, high thermal conductivity and strong braze performance. They also have good recycling properties with high scrap value which can deliver significant environmental and commercial benefits. In the current scenario, a modified core 3003[1] aluminum alloy with AA4045 clad layer brazing sheet is commonly used for the fabrication of heat exchangers. The brazing sheet generally comprises of a core alloy clad on 1 or 2 sides with a lower melting aluminum-silicon (Al-Si) alloy, generally AA4045. The clad layer melts and flows during the brazing process to provide upon cooling a metallic bond between the components (Figure 1.3).

[1] Table 1.1 shows some common major alloying elements to aluminum

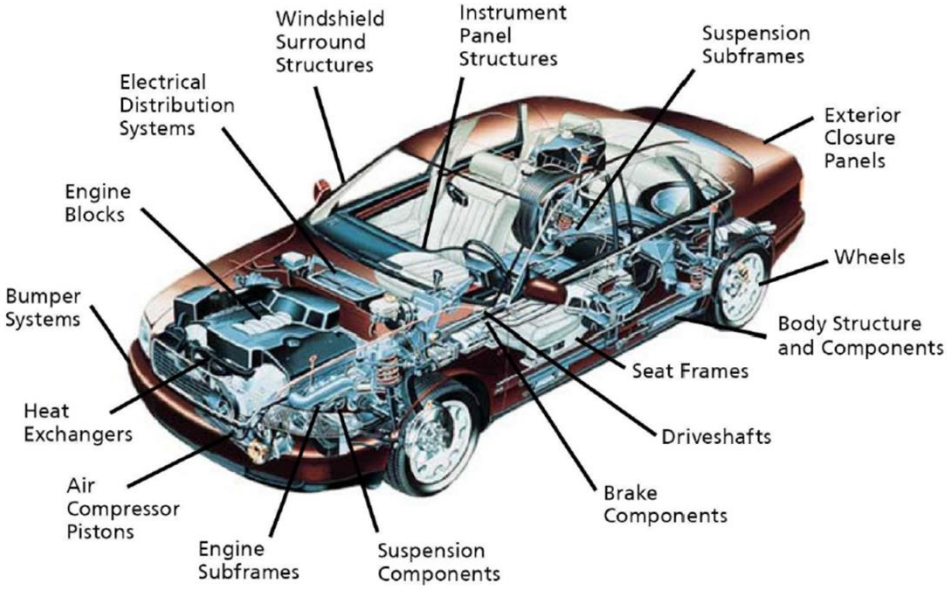

Figure 1.1 Applications of aluminum in passenger vehicles (www.drivealuminum.org).

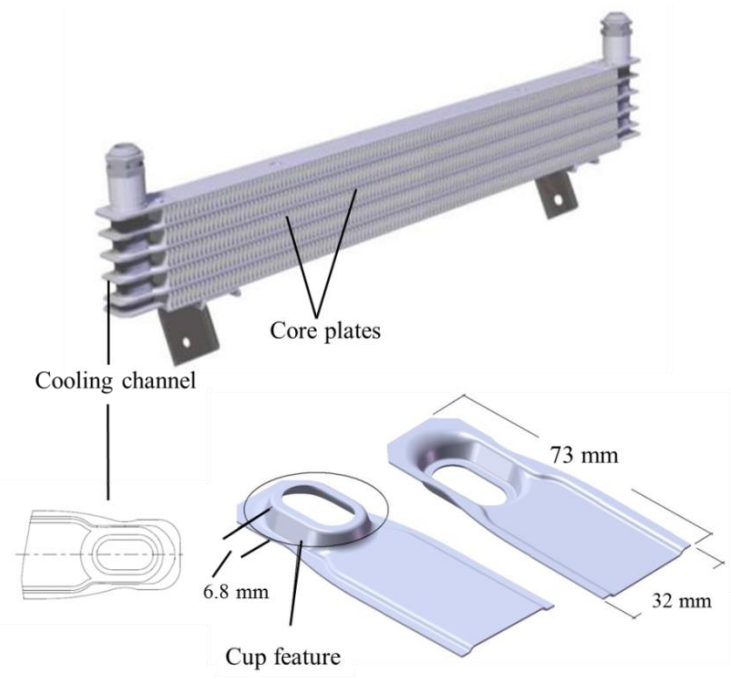

Figure 1.2 Schematic of a heat exchanger plate component incorporating the cup shape feature at the end (www.plateandfinheatexchanger.com; Bagheriasl et al., 2012).

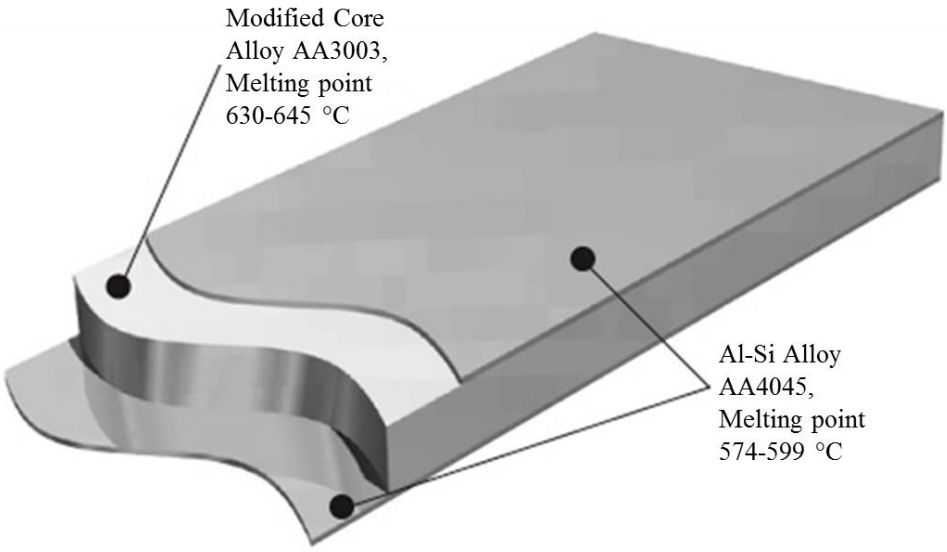

Figure 1.3 An example of a brazing sheet (www.aluminium-brazing.com).

Table 1.1 Common aluminum alloys and their applications

Aluminum Alloy	Main Alloy	Properties	Common Applications
AA 1100	None	High corrosion resistance, formability	Food and packaging industry
AA 2014	Copper	High strength, low corrosion resistance, non-weldable	Airframes, automotive parts
AA 3003	Manganese	High ductility, excellent corrosion resistance, Good brazability	Heat exchangers, motor vehicle radiators
AA 4043	Silicon	good weldability	Welding electrodes, brazing alloy
AA 5182	Magnesium	Good formability and corrosion resistance	Sheet metal work, appliances, automobile frames
AA 6063	Magnesium and Silicon	High strength, good corrosion resistance	Window frames, architectural extrusions
AA 7075	Zinc	Very high strength, good	Aircraft industries,

		corrosion resistance	recreation equipment

One drawback of aluminum alloys, particularly brazing sheet, it poor room temperature formability (ability to deform plastically without necking) which limits application over steels for complex shapes like automotive body parts where greater strength matters.

The current work is focused on the AA3003 brazing sheet which is used to fabricate the heat exchangers for passenger vehicles, in particular, examining the potential to increase the formability of these alloys by warm forming. The balance of this chapter provides a review of pertinent literature on warm forming of aluminum alloys.

1.1 Formability of Aluminum Alloy Sheets

Despite the high strength to weight ratio and excellent corrosion resistance offered by aluminum alloy sheet, its poor formability at room temperature compared with steel has created a major barrier to widespread adoption use in the automotive industry. Since, the inferior room temperature formability of aluminum alloys makes it more difficult and expensive to use in mass production of structural and body parts, i.e., the maximum attainable strain in one process step is less than that for mild steel along the same strain path (Kurukuri et al., 2009). One of the techniques to improve the formability of aluminum sheet is combining the mechanical loading with a thermal component. A particular example is warm forming, i.e. utilization of the increased formability of aluminum at elevated temperatures up to the recrystallization temperature. In this process, parts of the tools are heated and other parts are cooled which makes it possible to manipulate local flow behavior, in order to increase the formability (Li and Ghosh, 2004; van den Boogaard and Huétink, 2006; Abedrabbo et al., 2007; Kurukuri et al., 2009; Bagheriasl et al., 2014). Another example from the aerospace industry is stretch forming of aluminum (AA2024) parts in a number of stages with intermediate annealing steps and a final solution heat treatment, quenching and ageing (Kurukuri et al., 2011). It is widely accepted in several studies (Li and Ghosh, 2004; van den Boogaard and J. Huétink, 2006; Abedrabbo et al., 2007; Toros et al., 2008, Kurukuri et al., 2009; McKinley et al., 2010; Ghavam et al., 2014; Bagheriasl et al., 2014) that the formability of aluminum alloy sheet is strongly influenced by the deformation temperature and the forming speed; therefore, various forming techniques have been investigated to determine the appropriate conditions of temperature and deformation speed to achieve better forming capabilities.

The warm forming process has been studied for several years (Shehata et al., 1978; and Wilson, 1988) and this process has some significant advantages when compared with other conventional methods.

Firstly, the forming limit strains increase with increasing temperature (below recrystallizing temperature). Secondly, this method provides freedom to fabricate aluminum alloys into complex shapes with fewer die progressions to form a specified geometry. This process also offers the potential to reduce spring-back because forming is performed at lower stress levels.

1.2 Elevated temperature formability of aluminum alloys

There have been extensive studies by Shehata et al. (1978) with aluminum 5000 series Al-Mg alloys (AA5082 and AA5005) and by performing uniaxial tension testing and punch stretching tests. They observed that below 300 °C, the elongation to failure of Al-Mg alloy increases with increasing temperature at low strain rate (~1.7×10^{-4} s^{-1}). They also studied the effect of Mg weight percentage in the alloy and observed an increase in the elongation to failure with increasing Mg content at all temperatures and strain rates. The flow stress is observed to be reduced under warm conditions. The drawability of 5000-series alloys at elevated temperatures was tested by Schmoeckel (1994, 1995) and they observed a profound temperature influence on the stamping process. Further investigations in their experiments with uniform heating and partial non-uniform heating of the tool led them to conclude that that even the limiting drawing ratio (LDR) increases with increasing temperature, the material formability is much better in case of partial heating than that with uniform heating.

Naka and Yoshida (1999) have focused a particular type of Al-Mg alloy of aluminum 5000 series (AA5083) where they investigated the deep drawability (pressing on the inner region of the sheet by a punch tool, whereas the side material is held by a blank holder) at different forming temperatures and forming speeds. The range for forming temperature and forming speed was fixed between 20–180 °C and 0.2–500 mm/min, respectively. They observed that the limiting drawing ratio (LDR) increases with increasing die/punch temperature whereas it decreases with increasing forming speed at all temperatures (Figure 1.4). Figure 1.5 represents the relationship between the maximum drawing force (punch load) and the forming speed (punch speed) at different temperatures. It is evident from the figure that the drawing forces are nearly equal at high speed (higher than 100 mm/min), but decrease to an extent with forming temperature at lower punch speed.

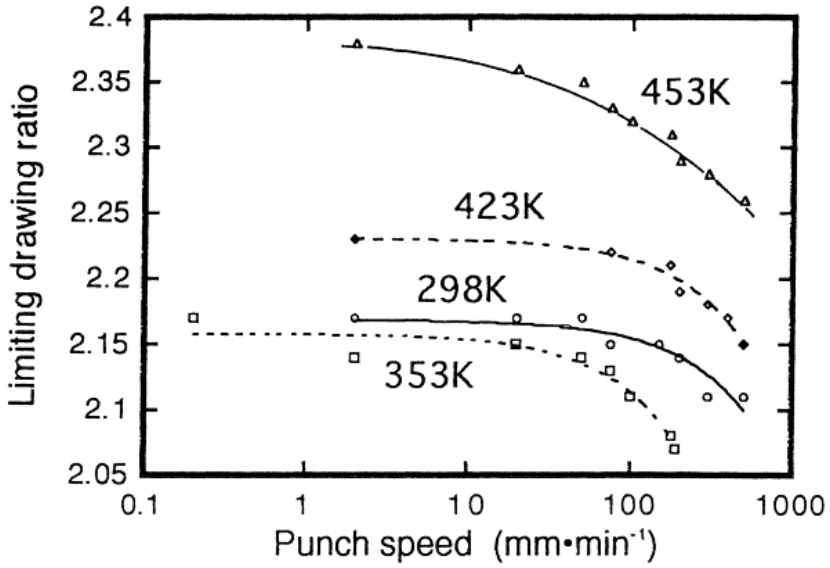

Figure 1.4 Influence of forming speed on the limiting drawing ratio at different forming temperatures (Naka and Yoshida, 1999).

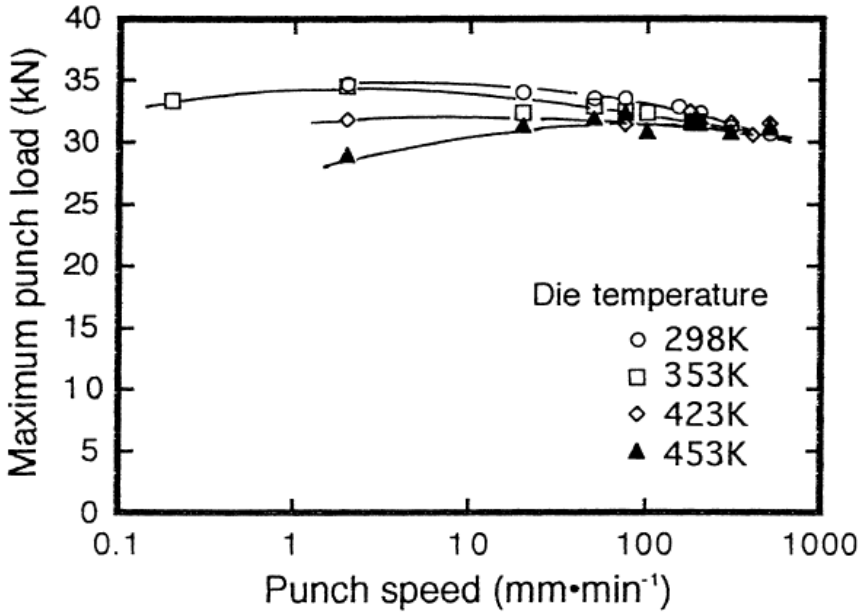

Figure 1.5 Relationship between the maximum punch force and punch speed at various forming temperatures (Naka and Yoshida, 1999).

Bolt et al. (2001) studied the feasibility of warm forming processes; they used three different aluminum alloy series (1050-H14 $Al_{99.5}$, 5754-O $AlMg_3$ and 6016-T4 $AlMg_{0.4}Si_{1.2}$) and did a comparative study of their formability, within the temperature range of 100-250 °C. Two different products have been analyzed in their work considering the application of deep drawing and stretching under 1000 kN hydraulic punch. They found a strong influence of temperature on the forming parameters in deep drawing experiments on box shaped and conical rectangular products and observed that the forming of aluminum at elevated temperature provides an increase in the product height (Figure 1.6).

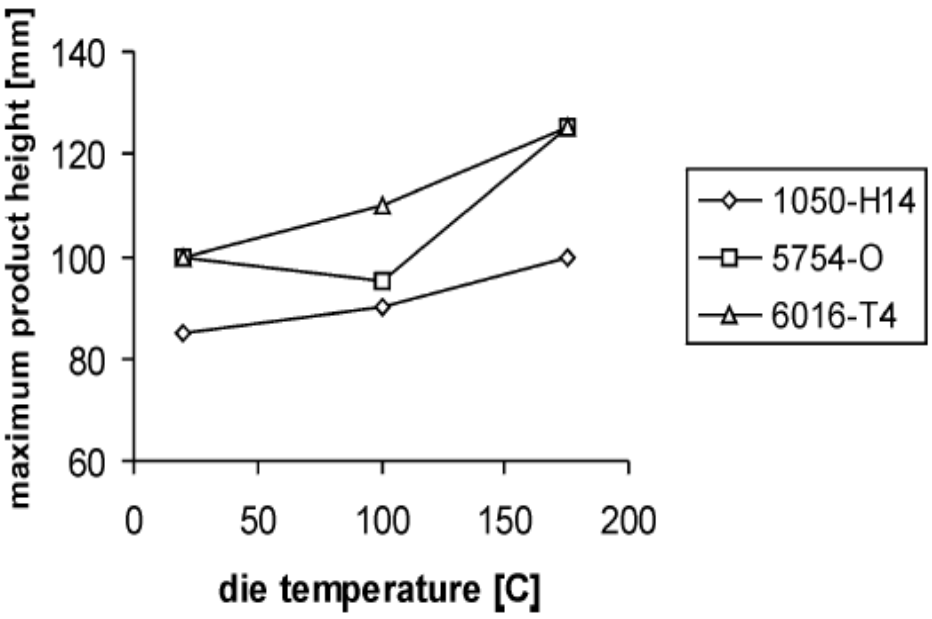

Figure 1.6 Effect of die temperature on the maximum attainable product height (Bolt et al., 2006).

Takuda et al. (2002) considered a cylindrical punch for their deep drawing experiments on AA5182-O aluminum alloy. A proper numerical simulation compared with the experimental results is described in this work. Their study shows that in order to achieve higher limiting drawing ratio (LDR), the temperature dependent flow stress should be uniformly distributed throughout the sheet. Both the experimental and numerical results showed that the LDR in warm deep drawing improves with die profile radius as shown in Figure 1.7.

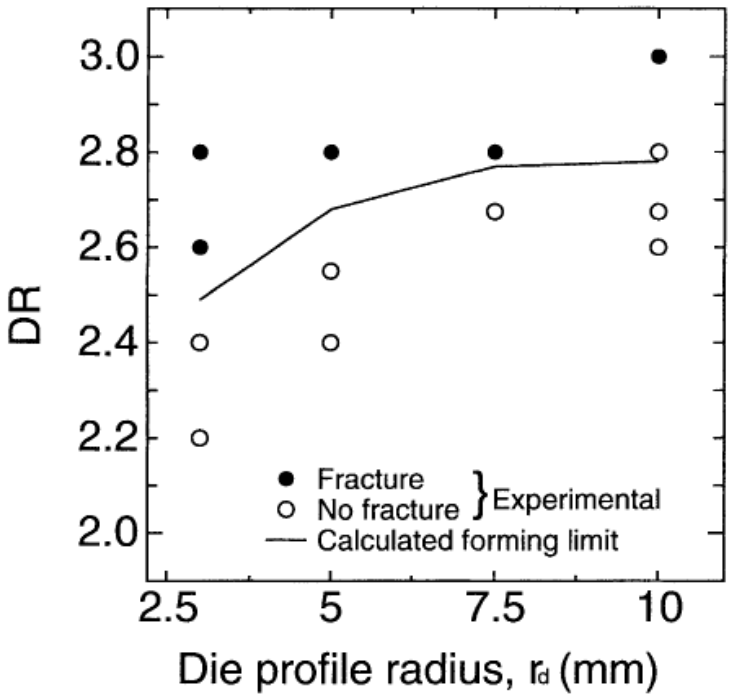

Figure 1.7 Forming limits in the warm deep drawing experiments at an elevated temperature of 250 °C (Takuda et al., 2002).

Li and Ghosh (2003) studied the uniaxial tensile deformation behavior of three different aluminum alloy sheets AA5182+1% Mn, AA5754 and AA6111-T4 in the temperature range of 200-350 °C and in the strain-rate range of 0.015–1.5 s^{-1}. They chose their forming process parameters carefully so that the post-forming properties don't deteriorate. The key finding of their work is the increase in the uniaxial tensile elongation with increasing temperature and decreasing strain-rate. They also observed an increase in strain rate sensitivity as well as decrease in the strain hardening with increasing temperature which accounts for the improvement in ductility at higher temperatures. The results depict that the warm formability for 5000 series is better than 6000 series.

Li and Ghosh (2004) have further extended their studies with a different approach to the biaxial warm forming process for the same alloys using a heated rectangular die/punch of cross-sectional area of 110 mm×50 mm, with all the other parameters kept the same as the previous study. In this second study, they investigated the formability of aluminum alloys by creating rectangular parts at a rapid rate of 1 s^{-1} using heated tooling under both isothermal and non-isothermal conditions and observed similar formability as previously reported for uniaxial forming for all three alloys where formability increases at elevated

temperatures and in similar fashion the 5000 series (AA5182+1% Mn, AA5754) alloys shows considerably greater improvement than AA6111-T4. Applying a gradient of temperature between the die and punch was favorable in promoting better formability. The forming limit curves (FLCs) under elevated temperature forming conditions were also derived and used specifically to predict the part depth (die cavity). The influence of temperature on the FLCs of all three alloys is shown in Figure 1.8. From the figure, it is observed that the formability of aluminum alloys increases with the increase in forming temperatures. It is also observed that the aluminum alloy AA5754 is more sensitive to forming temperature as compared to other two.

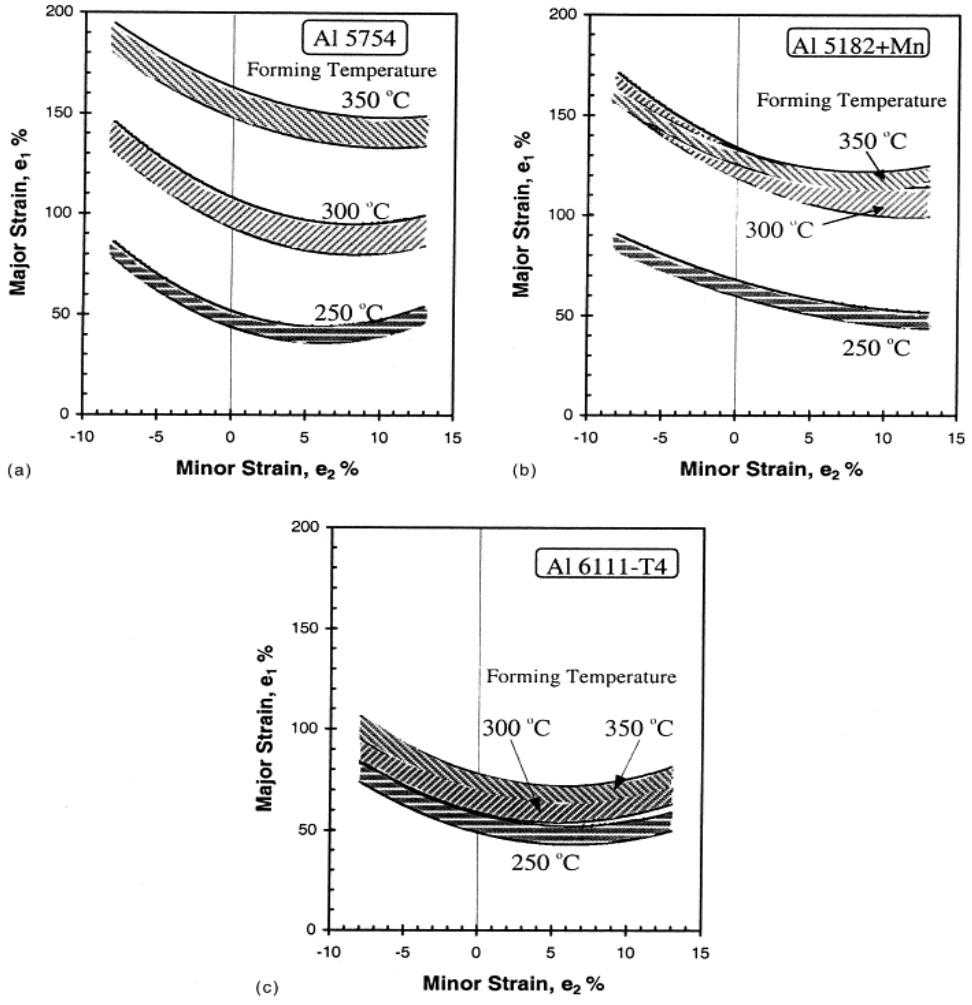

Figure 1.8 Influence of forming temperature on FLD (Li and Ghosh, 2004).

Using the material (Al5182+Mn) data published in Li and Gosh (2003; 2004) mentioned above, Kim et al. (2006) further extended their elevated temperature forming study using a thermo-mechanically coupled finite element analysis (FEA) considering the forming process with rectangular cups at different temperature levels (250, 300, 350 °C) and displayed the data using forming limit diagrams (FLDs), as shown in Figure 1.9. In this work, they mainly focused on parameters like maximum load, minimum thickness and thickness ratio to optimize the criteria for onset of failure. Their model predicted that a high temperature gradient between die and punch provides better formability and the strain limit increases with increasing the forming temperature, in general accord with the experiments.

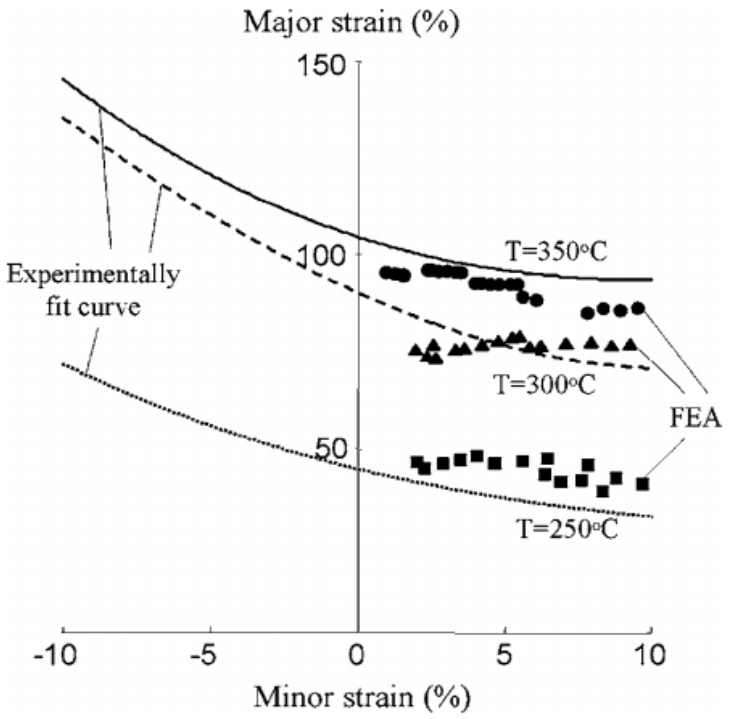

Figure 1.9 Influence of forming temperature on FLDs and contrast between FEA and experimental results (Kim et al., 2006).

Abedrabbo et al. (2007) performed LDH experiments on two aluminum alloys, AA5182-O and AA5754-O, using a double action hydraulic press. They used the experimental setup to form 101.6 mm diameter hemispherical cups from 177.8 mm diameter circular blanks. Pure stretch experiments were performed at elevated temperatures in the range of 25-260 °C. In their work they calculated strain based

FLD curves (ε-FLD) (Figure 1.10) at different temperatures for AA5182-O and observed that increasing the temperature effectively raises the forming limit curves.

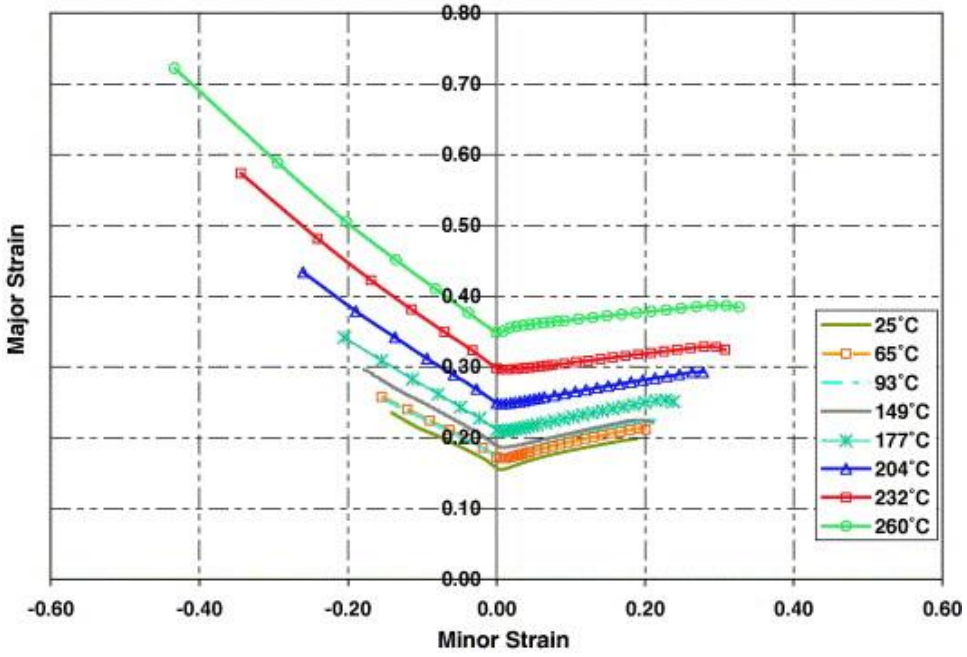

Figure 1.10 FLDs for AA5182-O at several elevated temperatures (Abedrabbo et al., 2007).

Palumbo and Tricarico (2007) studied the warm deep drawing (WDD) process using both experimental and numerical approaches and chose their specimen to be a 0.8 mm thick sheet of aluminum 5000 series alloy (AA5754-O). Temperature levels at the center of the blank specimen and the forming speed were selected as process parameters and the specimens were coated with a standard grease lubricant before the experiments. The key findings of their study are as stated below:

I. Punch speed greatly affects the warm deep drawing process.

II. Temperature in the blank center controls the process feasibility as well as formability in so much as the simulation results revealed the strong influence of the temperature gradient between the center and the flange on the strain concentration and failure as shown in Figure 1.11. The limiting drawing ratio (ratio of blank diameter D_b to punch diameter D_p, $= \frac{D_b}{D_p}$) is much greater (increased up to 44 %) at 110 °C for a punch speed of 1mm/min, as compared to that at room temperature.

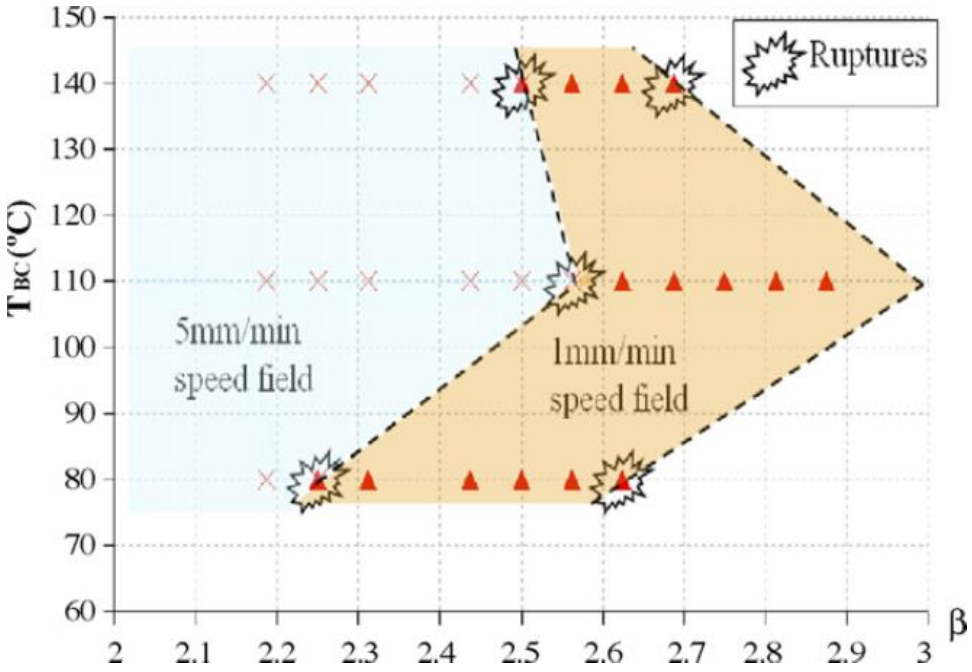

Figure 1.11 Test results showing both successes and failures for warm deep drawing operation (Palumbo and Tricarico, 2007).

Kaya et al. (2008) studied non-isothermal deep drawing of AA5754-O, AA5052-H32, and AZ31B-O sheets with sheet thicknesses of 1.3, 1.3, and 1.2 mm respectively. They investigated the effect of constant and variable punch velocity and temperature on the deformation mechanics. In their study the die and the blank holder were heated to 310 °C while the punch was cooled to 65 °C. The maximum punch velocities for the Al and Mg alloys were observed to be 35 mm/s at 300 °C and 300 mm/s at 275 °C, respectively. They concluded that increased temperature tends to reduce the thinning at the corner of the cup bottom reduces Al alloys but not for the Mg alloys. They also developed a numerical model using the finite element method (FEM) to correlate the process parameters such as strain-rate (punch velocity), temperature and physical properties of the material obtained from two different suppliers.

1.3 Formability of Aluminum Brazing Sheet

McKinley et al. (2010) investigated the effects of warm forming on Novelis X926 clad aluminum brazing sheet, the class of materials investigated in the current work, by performing deep drawing experiments. They observed no significant changes in material behavior between RT–150 °C, but the material

properties changed rapidly between 150–250 °C. When the temperature was increased from 150 °C to 250 °C the following observations were made:

– Elongation to failure increased by over 200%

– Flow stress decreased by 35% or greater

– With increasing strain rate, there was an increase in the flow stress and decrease in total elongation

– Very large post–uniform elongations occurred at 250 °C

Bagheriasl et al. (2011, 2012, 2014) studied the isothermal warm formability of a fully annealed 0.5 mm thick, AA3003 aluminum alloy brazing sheet. They developed forming limit curves (shown in Figure 1.12) using two different parameters such as forming temperature levels (RT, 100, 200, 250 and 300 °C) and forming speed/strain-rate levels (0.003, 0.018, 0.1 s^{-1}). In their study, they observed that the formability of the sheet can be improved significantly by increasing the temperature, with gains of up to 200% for this temperature range. They also observed that the forming speed has a mild effect on formability.

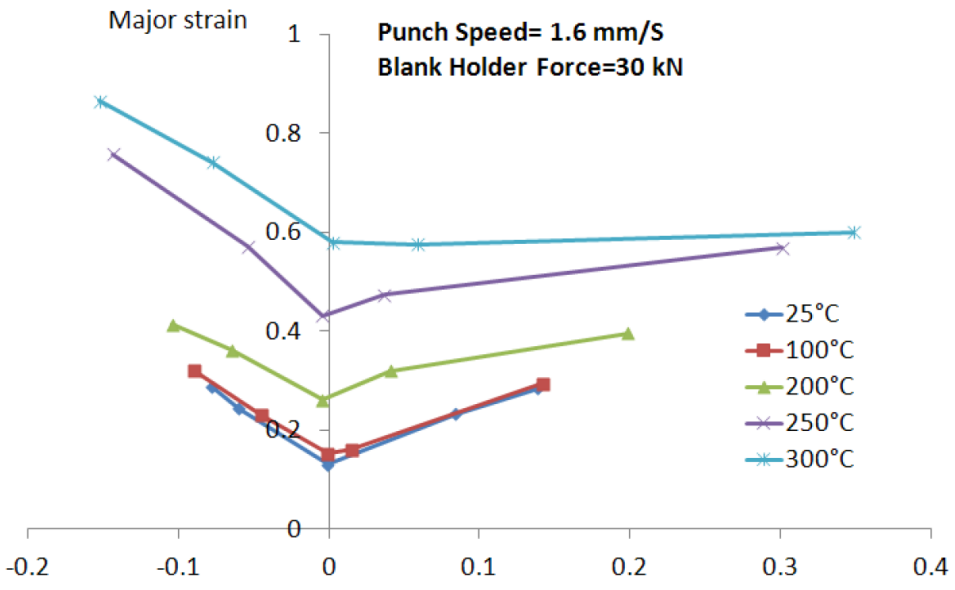

Figure 1.12 FLD of 0.5 mm thick AA3003 at 1.6 mm/s (Bagheriasl et al., 2012).

1.4 Influence of strain-rate on the formability of aluminum alloy sheet

Smerd et al. (2005) carried out experiments on AA5754 and AA5182 Al-Mg alloy sheets using a tensile split Hopkinson bar (TSHB) apparatus at room temperature and elevated temperatures in order to examine the constitutive response and damage evolution at strain-rates of 600, 1100 and 1500 s^{-1}. Despite of the low strain-rate sensitivity for both the alloys, AA5754 showed a mild increase in flow stress with strain-rate below 300 °C, while AA5182 was insensitive to strain-rate at room temperature. However, the final elongation was observed to decrease for both the alloys at 1500 s^{-1} and 300 °C (Figure 1.13).

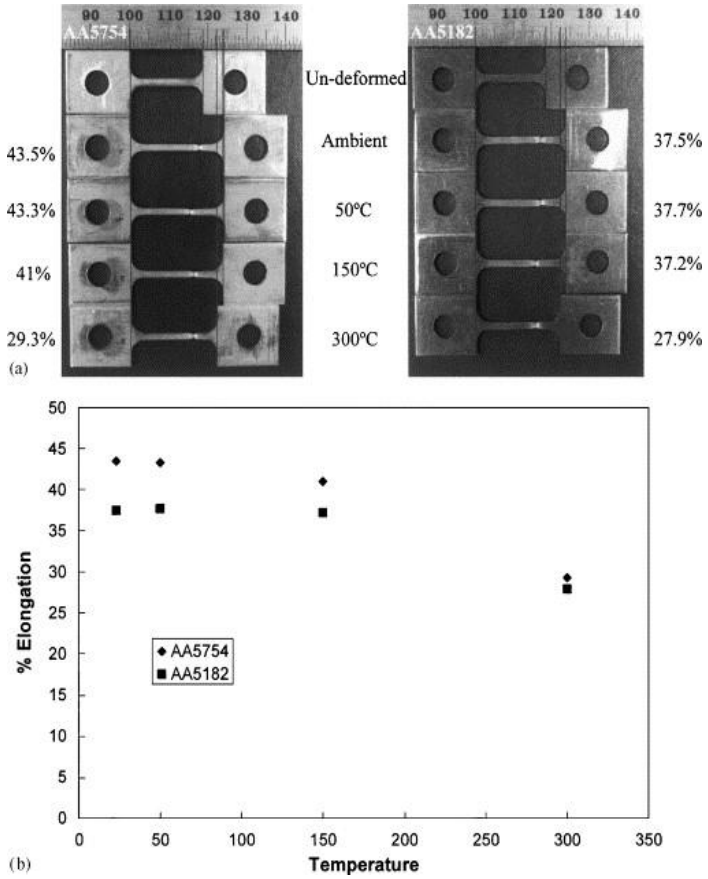

Figure 1.13 (a) Elongation versus temperature at a strain-rate of 1500 s^{-1} for AA 5754 (left) and AA 5182 (right) (b) Elongation versus temperature at a strain-rate of 1500 s^{-1} (Smerd et al., 2005).

Picu et al. (2005) studied the strain-rate sensitivity of 1 mm thick, non-heat treatable commercial AA5182-O aluminum alloy sheets at temperatures ranging from -120 to 150 °C and strain rates from 10^{-6} to 10^{-1} s^{-1} by performing uniaxial tension tests. They investigated the effect of dynamic strain aging on the

ductility and strain hardening by measuring the process parameters such as strain-rate sensitivity in constant and jump strain-rates which was observed to be negative for all strains at room temperature and 50 °C. They further developed a numerical model to compare with the experimental results. The variation of strain-rate sensitivity parameter (*m*) with strain at three different temperature levels is shown in Figure 1.14.

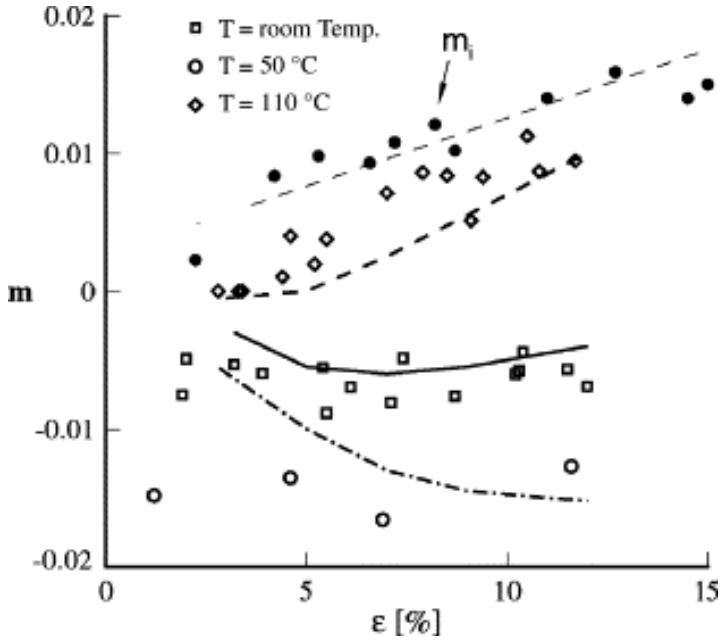

Figure 1.14 Strain-rate sensitivity (m) variations with strain at three different temperatures (Picu et al., 2005).

Lademo et al. (2010) carried out steady-state tensile tests for two different types of aluminum alloys, namely AA1200 and AA3103 at several strain-rates in range from 10^{-4} to 1 s^{-1} and investigated the instantaneous rate sensitivity and rate sensitivity of strain hardening during the constant strain-rate and strain-rate jump tests. From the test results shown in Figure 1.15, it was established that the instantaneous rate sensitivity is independent of strain while the rate sensitivity of strain hardening increase with increasing strain-rate for both the alloys. They also observed that the yield stress is nearly invariant to strain-rate, whereas strain hardening at low strains increases markedly with increasing strain-rate. Little effect of strain-rate on the strain at necking was observed because of the fact the work-hardening rate at these strains is mainly independent of the strain-rate.

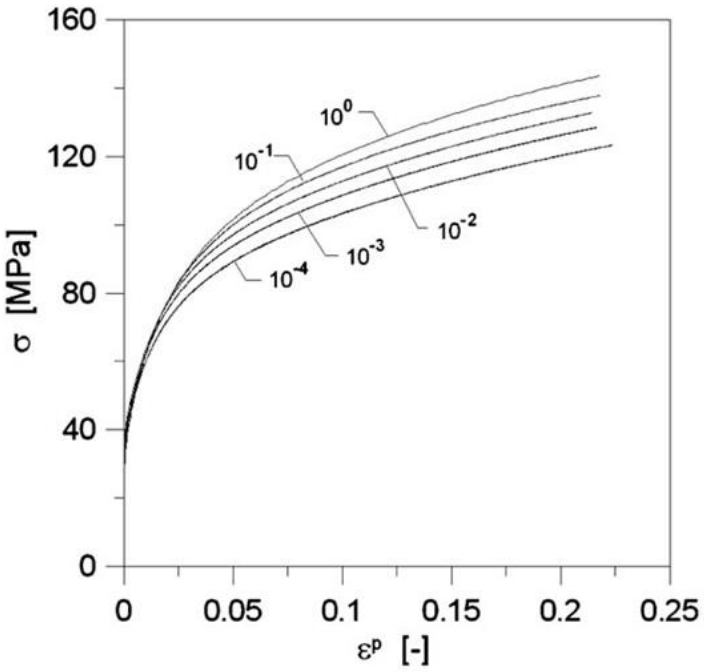

Figure 1.15 Tensile test results from the constant strain-rate tests for AA3103; Cauchy stress versus logarithmic plastic strain curves up to incipient necking from tensile tests at nominal strain-rates of 10^{-4} s^{-1} - 1 s^{-1} (Lademo et al., 2010).

Kabirian et al. (2014) investigated aluminum alloy AA5182-O in temperature range from 23-150 °C and strain-rate from 10^{-4} to 3500 s^{-1}. They summarized the AA5182-O stress-strain responses into three systems:

I. At temperatures lower than 100 °C and the quasi-static domain, negative strain-rate sensitivity dominates and turns into a positive number when loading rate comes into the dynamic domain.

II. At 100 °C, zero strain-rate sensitivity in quasi-static region is replaced by a positive number at dynamic loadings.

III. At temperatures more than 100 °C, positive strain-rate sensitivity dominates over the whole range of loading.

Rahmaan et al. (2015, 2016) performed room temperature tensile and shear tests at strain rates ranging from 0.01 s^{-1} to 600 s^{-1} for AA5182-O sheet using DIC techniques. AA5182 exhibited PLC bands (King

et al., 1981; Kang et al., 2006) leading to negative rate sensitivity for strain rates below 1 s^{-1}. Above this rate, PLC bands are suppressed and positive rate sensitivity is observed, which likely accounts for the increase in ductility at high rates reported by Hadianfard et al. (2008).

1.5 Forming Limit Diagram

The Forming Limit Diagram (FLD) was originally proposed by Keeler and Backofen (1963) for the tension–tension domain and extended by Goodwin (1968) to the tension–compression domain. It is broadly utilized for characterizing the extent to which metal sheets can be deformed without localized necking or fracture. Figure 1.16 is a representation of in-plane strain state of the material sheet and the FLD represents the boundary between safe deformations and the beginning of plastic instability, determined experimentally by varying the forming conditions and evaluating the forming limits. Some common parametric conditions are balanced biaxial tension, in-plane plane strain and combined tensile/compressive (draw) strain states. Previous research have shown the methods to determine the major forming limit strain and minor forming limit strain (limit strain is described as the maximum strain of the material before the necking onset) in order to develop FLD. Detailed explanation of different methods to determine forming limit strains is provided in section 1.7.

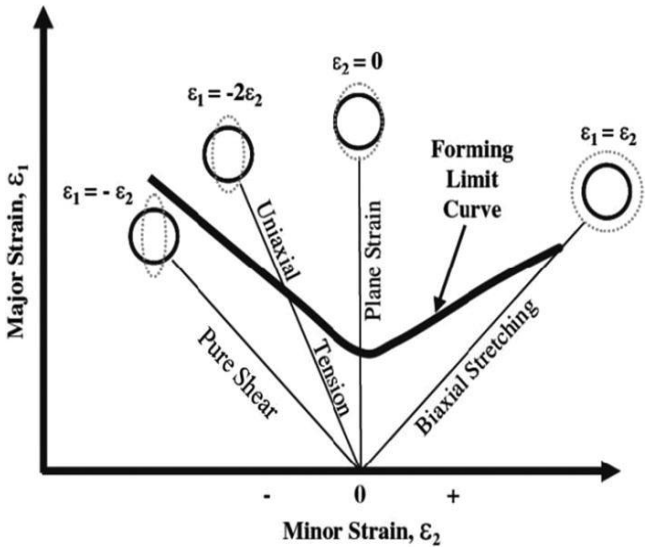

Figure 1.16 Representation of the forming limit curve (FLC) and typical strain paths obtained in sheet metal formability tests utilized for determining the FLC (Hasan et al., 2011).

Nakazima et al. (1968), for the first time, measured and compared the forming limit strains for strips of varying widths to measure forming limit strains. Hecker et al. (1978) further developed the method, using a specimen that is well lubricated and then firmly clamped and stretched over a 101.6 mm (4 inch) diameter punch. The load is applied to the strip through the punch until localized necking is detected and thus the maximum load is identified. The strain ratios and limit strains are measured near the necking area using etched circles or grids which deform during deformation from which the forming limit curve (FLC) can be constructed. Dinda et al. (1981) combined the above two techniques of Nakazima and Hecker and developed a method to generate FLDs. Harvey et al. (1984) presented a computer-image analysis method to avoid the uncertainties during the manual measurements.

1.6 Formability experiments

Formability can be defined as the ability of the metal work piece (sheet in this case) to undergo plastic deformation (stamped/formed) without any damage. The forming behavior of any metal sheet is analyzed by performing many different mechanical tests such as bulging and uniaxial or biaxial tensile experiments (Marciniak et al., 1965; Hasek, 1973; Ghosh et al., 1985). There are various factors which can cause uncertainty in the results, including variations in material flow properties, die material, die/punch shape, press speed, lubricants etc. (Cockroft et al., 1968; Marciniak, 1984; Banabic et al., 1992). Each of these can cause failure in the material separately; therefore, it is rare to develop a single formability test to quantify all other forming applications. One of the basic parameters to analyze formability and ductility during the formability test is fracture strain. Some of the parameters contributing high drawability (by resisting thinning) include high strain hardening exponent (n) and high value of strain-rate sensitivity index (m). Lower yield strength promotes lower spring back. Different methods have been considered to provide insight into material performance under actual forming/stamping conditions; some of these are discussed in the following.

1.6.1 Formability evaluation experiments

Stretching and drawing are the two primary modes of sheet metal deformation used in industrial stamping processes. The Swift cup test (Chung and Swift, 1951), the Erichsen/ Olsen dome tests (Erichsen, 1912; Olsen 1920), and Limiting Dome Height (LDH) test (Hecker, 1974 and Ghosh, 1975) are tests frequently used for formability characterization. The details of these experiments are discussed in the following sections.

- Swift Cup test (Chung and Swift, 1951)

This experiment investigates the drawability of a well lubricated sheet metal by forming a vertical cylindrical drawing using a small flat-bottomed cup (Figure 1.17) with differing blank diameters to determine the limiting drawing ratio (LDR). The LDR is defined as the ratio of the maximum diameter of the blank that can be drawn without fracturing to the diameter of the punch. This test is suitable to predict the performance of sheet metals in deep-drawn products, however, it is inaccurate when predicting the behavior in stretching processes and it is also time consuming.

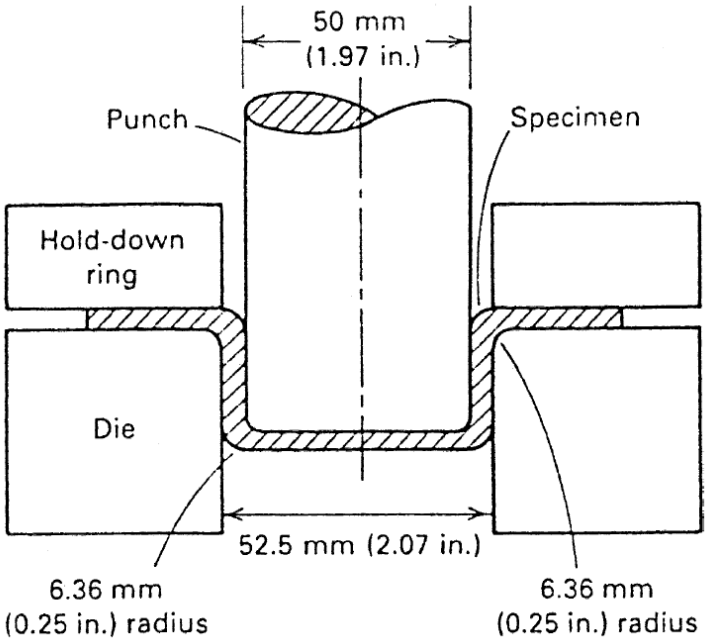

Figure 1.17 Swift's cup drawing test (Narasimhan et al., 1996).

- The Erichsen (1914) and the Olsen (1920) tests

Erichsen (1912) was the first to develop tests for evaluating the forming behavior of sheet metal in stretching conditions. Hemispherical punch was used to press the sheet metal (clamped between two polished flat plates with a hole of 25.4 mm diameter) until failure occurs as shown in Figure 1.18. Olsen (1920) then introduced a test similar to that proposed by Erichsen (1914) but with a different size of tools.

Because of the poor reproducibility and lack of correlation with other mechanical properties these tests were not widely accepted.

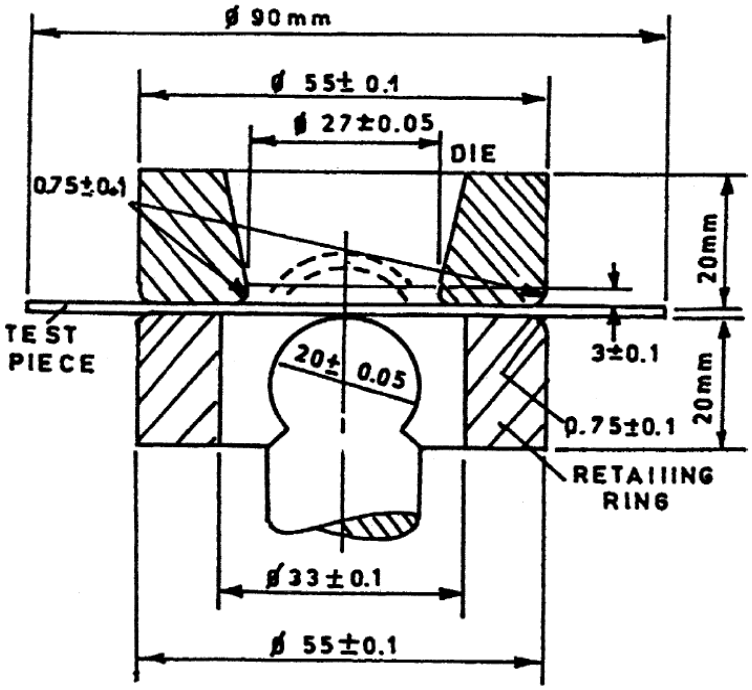

Figure 1.18 Schematic of Erichsen and Olsen tests (Ghosh et al., 1975).

- Limiting Dome Height test (Hecker, 1974 and Ghosh, 1975)

Hecker (1974) attributed the poor reproducibility of the Erichsen/Olsen test to the high bending strains using such a small punch and insufficient clamping using small, smooth dies. He recommended using a bigger hemispherical punch and dies (102 mm diameter) with a lock bead to prevent draw-in. Later Ghosh (1975) modified the Hecker test in order to simulate plane-strain conditions (under which most of metal forming failure occurs) by using varying-width strip specimens. This test is known as the Limiting dome height (LDH) test.

This method uses a 102 mm hemispherical punch to press the sheet-metal specimen with different strip widths, rigidly clamped in a blank-holder and stretched over the punch (Figure 1.19). The metal strips are marked with a grid of small circles (2.5 mm diameter) and the width strain at the fracture site is measured

from the closest intact circle to the fracture. The width strain is smallest at a critical blank-width and the height where the fracture occurs in the dome is called limiting dome height. LDH test is one of the most popular tests in the industry because of its ability to simulate the most critical strain state (plane-strain conditions) observed during stamping but still comes with some drawbacks. Recently, this technique has been losing interest because of its inconsistency and large scatter in the dome height values. Story (1982) analyzed and explained the significant effect of the sheet thickness and the punch radius ratio on the limit strain. Therefore, the LDH values should not be compared for sheets of completely different thicknesses. Vegter et al., (1985) proposed the use of smaller punch (other than normally used 102 mm punch) and they observed an increase in the limit strain by decreasing the punch diameter. This encouraged an important supportive effort by the North American Deep Drawing Research Group (NADDRG, 1987), leading to a recommended standard practice. The lock bead is also an important component, which has a vital role to ensure a pure stretching operation during the formability test.

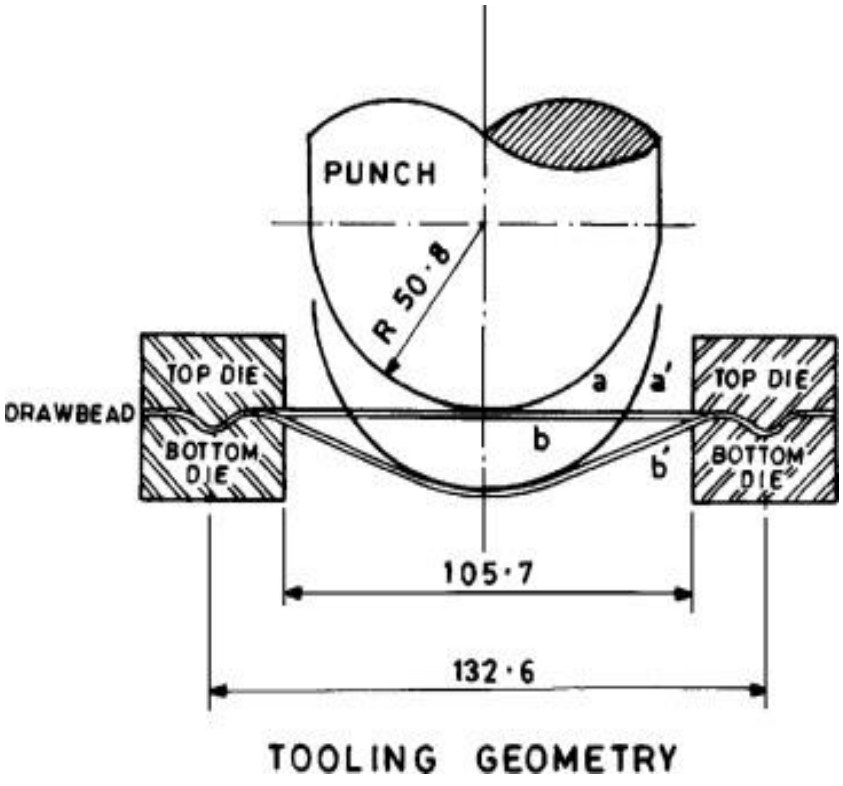

Figure 1.19 Schematic of dome height test, where a and a′ indicate the positions of punch before and after deformation of the sheet corresponding to b and b′ (Ayers et al., 1975).

1.7 Different methods for forming limit strain evaluation

Considerable effort has been expended to develop reliable procedures to quantify the limit strains of different sheet metals (Hayashi, 1997; Montfort and Novello, 1999; Hotz et al., 2001; Geoffrey, 2003). In the late 60's, Takashina (1968) presented a simple three circle method to determine the limit strains which was then improved further by Veerman et al. (1972), but the most precise method for measuring the limit strains was developed by Bragard et al. (1972) who incubated the interpolation technique (Figure 1.20).

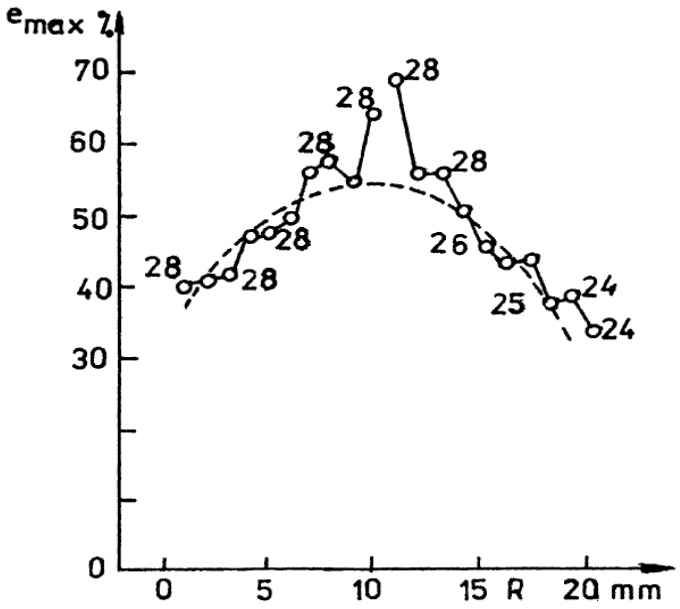

Figure 1.20 Interpolation method (Bragard method) to determine the limit strain (Bragard et al., 1972).

Hecker (1974, 1975) recommended a technique based on the determination of three types of ellipses around the fracture as shown in Figure 1.21. In this method, the major and minor strains of different types of ellipses were determined near the fracture on the deformed specimen and then transposed onto FLC.

Hotz et al. (2006) has introduced a new method which is termed an 'in-process measurement' method (Figure 1.22) to determine the forming limit curve which was explained in detail by Libertz et al. (2004). A similar process is applied as the Bragard method where they used a video camera system to film the forming process and the fracture analysis and strain distribution was observed based on the film.

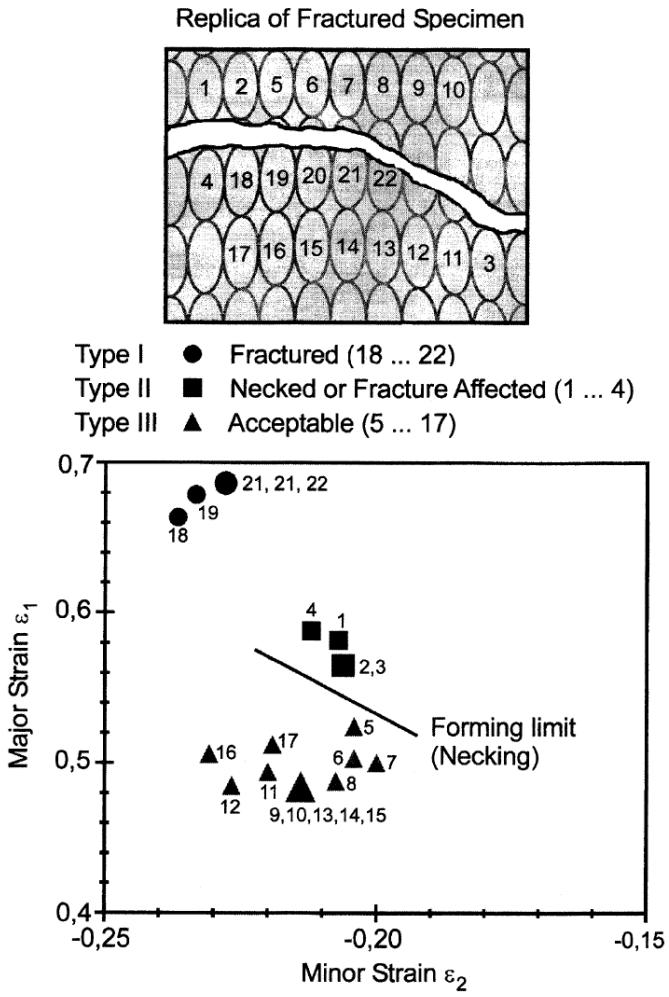

Figure 1.21 Hecker method to measure the limit strain (Hecker, 1975).

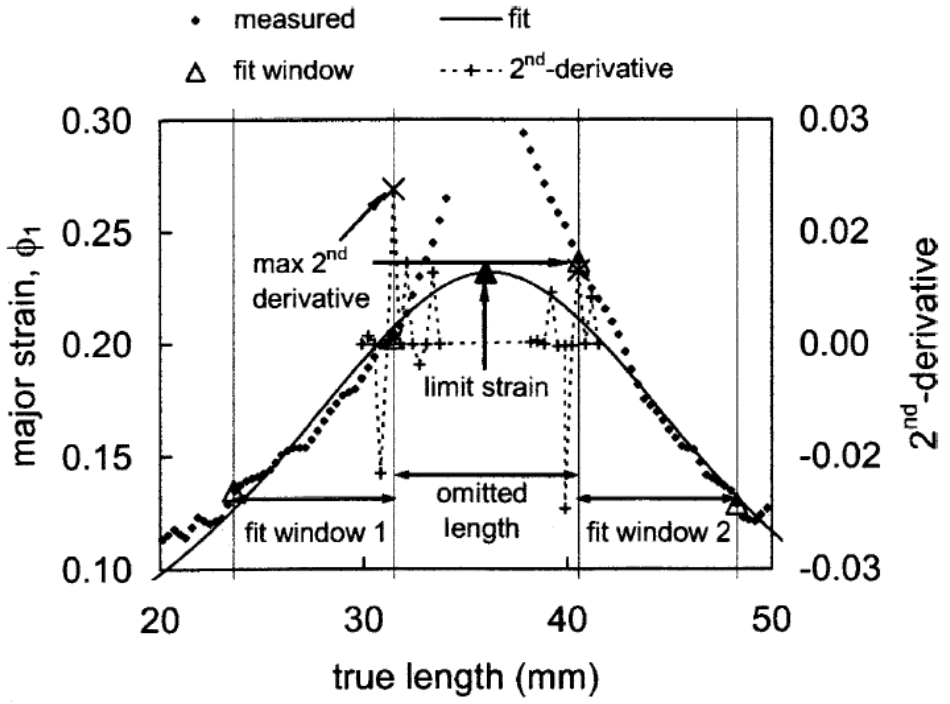

Figure 1.22 IDDRG method to determine the limit strain (Hotz et al., 2006).

Later the determination of FLDs was standardized within the International Standard Organization ISO 12004-2 (2008) "Metallic materials - sheet and strip - Determination of forming-limit curves". This standardized method identifies the testing conditions to be used when generating forming limit curves at room temperature, by using linear strain paths. This procedure is recommended for flat metallic sheets with thicknesses between 0.3 mm and 4 mm as proposed in the Marciniak (1965) and Nakazima (1967) methods. In this technique, the strain across the deformed specimen is calculated and the measured strains are sorted in a way that the failed area is eliminated from the results. By removing the strain points in the necked area, the strain distribution just before the onset of necking is created again in this region by curve fitting on both sides of the neck (Figure 1.23). The maximum strain that can be imposed on the material without failing is determined through interpolation and the maximum of the interpolated curve is called the forming limit.

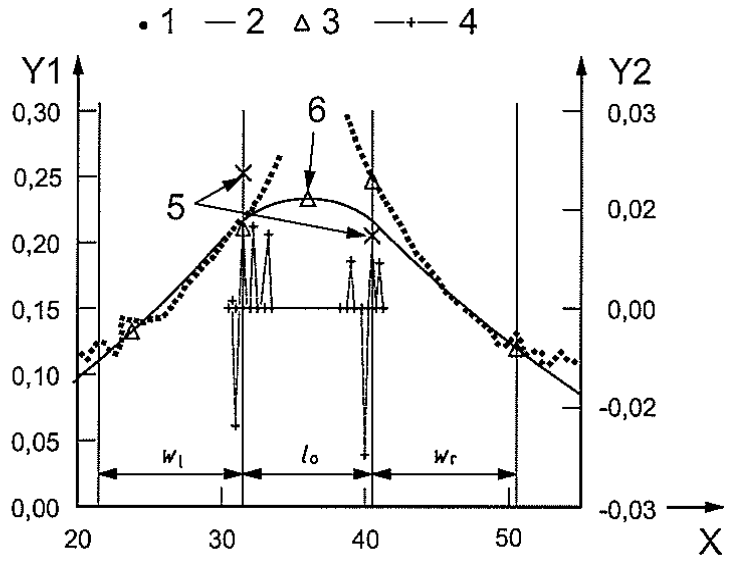

Key

X arc length, in millimetres
Y1 major true strain, ε_1
Y2 second derivative of major true strain ε_1 to arc length
1 measured strain distribution
2 an inverse parabola over the fit windows 5, 7 and 9
3 marking points of the fit window on the strain distribution
4 second derivative over a distance of 6 times the original thickness
5 maximum points of the second derivative, marking the inner limits of the regression
6 major forming-limit strain, ε_1
w_l left fit window width
l_o omitted length between the inner fit limits left and right to crack
w_r right fit window width

Figure 1.23 ISO 12004 – cross section method to determine the limit strain.

Some instances of measured strain distributions which lead to unrealistic forming limit values can occur when using the ISO method. For example, if friction conditions are such that necking does not occur at the center of the dome, the strain distribution will no longer by symmetrical leading to a distortion of the interpolation shown in Figure 1.23. In such cases, the ISO method will not provide a good representation of the strain conditions at onset of necking.

1.7.1 Time-dependent methods

Optical strain measurement methods, such as the Digital Image Correlation (DIC) technique due to Smith (1998) are have been widely adopted to measure the strain distribution over the entire surface of the sample for the complete duration of the test. In the DIC method, a high contrast random speckle pattern is applied to the specimen surface which is tracked during deformation using stereo cameras from which the strain distribution history can be extracted. The drawbacks of the ISO method discussed above as well as the new ability to obtain continuous strain data through DIC have prompted the establishment of time-dependent methods for determining the FLC, as an alternative to position-dependent methods for which the onset of necking is determined by studying a single instant in the process (ISO 12004 method). Time-dependent methods include those developed by Volk and Hora (2010), Merklein et al. (2010) and Martínez-Donaire et al. (2014), as described in the following text.

- Linear best fit time-dependent method (Volk and Hora, 2010)

The linear best fit method was proposed by Volk and Hora (2010) based on the temporal analysis of the thickness strain, ε_3 and its first derivative (the thickness strain rate, $\dot{\varepsilon}_3$) at locations within the failure region (Figure 1.24). Two straight lines are calculated using regression analysis along the representative thinning rate evolution, one through the stable deformation stage and the other through the last stage just before specimen failure. The intersection of these two lines is identified as the onset of the plastic instability, as shown in Figure 1.24. In order to reduce the noise in the time derivative of thickness strain, a least squares parabolic fit is made for seven points and the time derivative of thickness strain is calculated from this parabolic equation at the given time step, as described in ISO 12004-2 (2016). Similar to the ISO 12004-2 (2016) approach, the method described above is applied to five adjacent locations in the localized necking zone and the final limit strain is considered as the average value of the strains determined in the aforementioned locations.

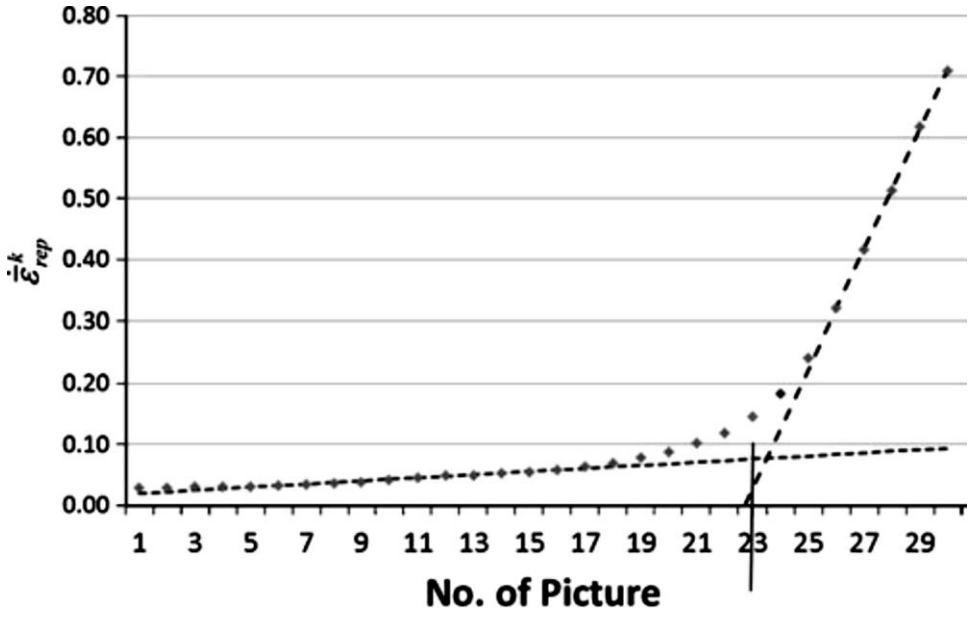

Figure 1.24 Determination of onset of instability by linear curve fitting method with least square method where "No. of picture" refers to the image number just prior to fracture (Volk and Hora, 2010).

- Moving correlation coefficient method (Merklein et al., 2010, Merklein et al., 2014)

The moving correlation coefficient method due to Merklein et al. (2010) is based on the analysis of the rate of change of the major strain of selected positions in the area where the unstable necking will happen. The time history of the second time derivative of the major strain, averaged over all points inside the selected area around the necking zone, is analyzed to detect the instant of the beginning of the unstable necking. In this method, the major and minor limit strains are objectively determined by a mathematical function called the coefficient of correlation as follows:

$$r = \frac{\sum(t - \bar{t})(\ddot{\varepsilon}_1 - \bar{\ddot{\varepsilon}}_1)}{\sqrt{\sum(t - \bar{t})^2 \sum(\ddot{\varepsilon}_1 - \bar{\ddot{\varepsilon}}_1)^2}}$$

where *t* (x-axis) represents the time in seconds and $\ddot{\varepsilon}_1$ (y-axis) represents the second derivative with respect to time (acceleration) of the principal strain. The correlation coefficient should be close $+1$ when the data are distributed near a line and should tend to *0* when randomly distributed like a cloud of points. However, for the correlation coefficient calculated from the rate of major strain rate versus time data, the inverse is happening since the data at the beginning of the experiment is horizontal and the correlation coefficient r is undefined for horizontal and for vertical distributions since those conditions correspond to $0/0$ condition. To eliminate the starting correlation coefficient at $r = 0$, Merklein et al. (2014)

proposed a linear time function with slope n between 0.1 and 1 which is added to the rate of major strain rate curve and the correlation coefficient becomes $r > 0$. In this method, the correlation coefficient is calculated by taking a series of different subsets of constant size over the full data set (using a selected area around the necking zone) in a manner similar to a moving or gliding average data filter. The correlation coefficient is nearly 1 when it is far away from the necking zone and the coefficient becomes smaller than 1 when the acceleration deflects to high values and grows again towards 1 when the acceleration is tending to infinity (Figure 1.25). The instant when the correlation coefficient traces a minimum is indicative of the onset of necking, as shown in Figure 1.25, and the corresponding major and minor strain values represent the data point for the FLC.

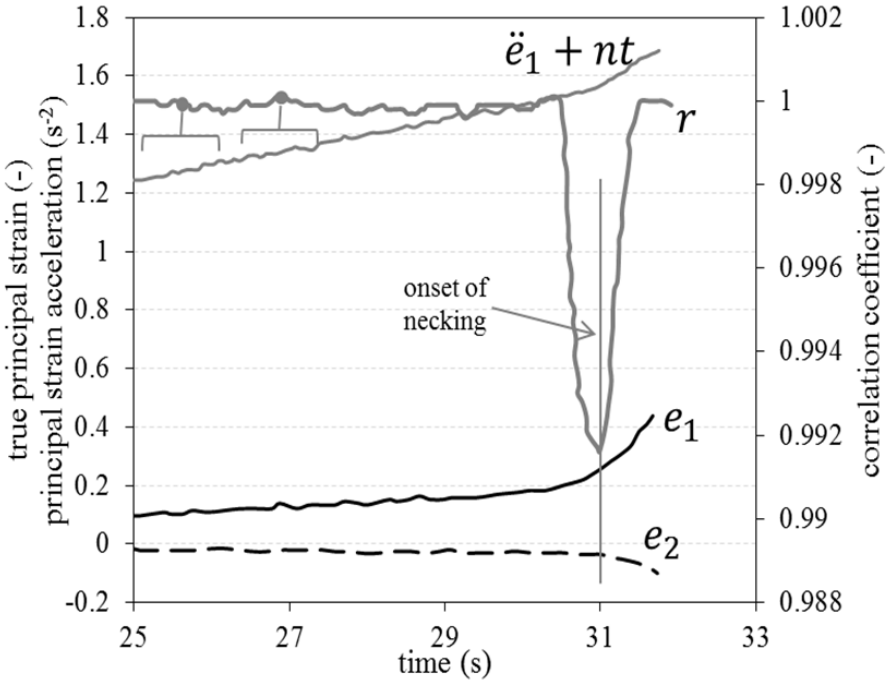

Figure 1.25 Determination of onset of necking using the coefficient correlation time-dependent method (Kurukuri et al., 2015).

- Necking zone method (Martínez-Donaire et al., 2014)

Martinez-Donaire (2014) proposed a time-dependent methodology called the "necking zone method". First, the width of the necking region is identified from the deformed sample by calculating the major strain rates at various locations near to the final fracture location, as illustrated in Figure 1.26. During

loading, the first time derivative of (ε_1) in the necking zone (Point B, in Figure 1.26) monotonically increases until fracture occurs. The onset of necking is associated with a decreasing strain rate in the material adjacent to the necking region, which vanishes before fracture occurs. Therefore, the necking process begins when the strain rate at the boundary of the instability region (point A in Figure 1.26) reaches a local maximum value ($\dot{\varepsilon}^{A}_{1,max}$). From this moment, the strain rate at the limit of the necking region begins to decrease to zero, signaling the start of the strain localization process inside the region. The corresponding major and minor strains in the necking zone are considered as limit strains.

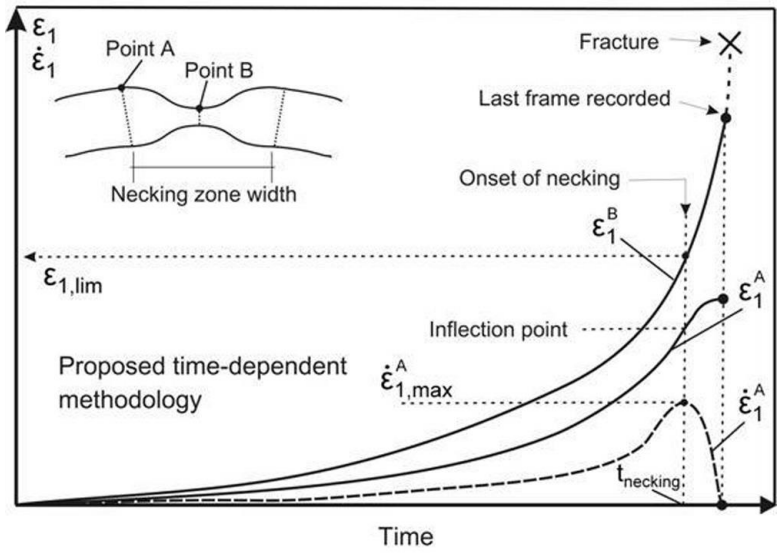

Figure 1.26 Determination of onset of necking using the necking zone time-dependent method (Martínez-Donaire et al., 2014).

1.8 Lubrication in warm forming conditions

Lubricants properties are generally affected by die/sheet interfaces and temperatures during warm forming. Hence it is essential for a warm forming lubricant to provide enough lubricity at temperature ranges from 25 °C to 250 °C or higher. Very little research has been reported on the warm forming lubricants; therefore ideal lubricants for the warm forming of aluminum alloy sheet are yet to be discovered. Biaxial deformation experiments of 5083 Al alloy sheet into a rectangular die cavity with or without lubrication were conducted by Wu et al. (2006). They observed that decreasing the interfacial friction by the lubricant enhanced the metal flow when the die surface touches the deformed sheet.

Kaya et al. (2008) performed deep drawing experiments on three different aluminum alloys namely, AA1050, AA5754 and AA6016 as well as AZ31 magnesium sheet using Teflon (PTFE) film, a grease with 7.5% boron nitride and a grease without boron nitride as lubricants. They reported that:

- Teflon sheet resulted in a more uniform sheet thickness than the other non-PTFE lubricants.

- Non-PTFE lubricants caused smoke and left a burnt residue on the tooling.

Bagheriasl et al. (2012) reported the influence of lubricant on the formability of aluminum alloy sheet at temperatures greater than or equal to 150 °C by conducting LDH experiments on 0.5 mm thick AA3003 brazing sheet. They compared two different lubricants (Dasco Cast and Teflon sheet) by measuring the coefficients of friction using the Twist Compression Test (TCT) at three sliding velocities of 1.6, 8 and 40 mm/s (Figure 1.27). They observed that Dasco Cast lubricant shows better performance in the higher temperature range while Teflon sheet lubricant enhances the performance over the entire range of temperatures tested.

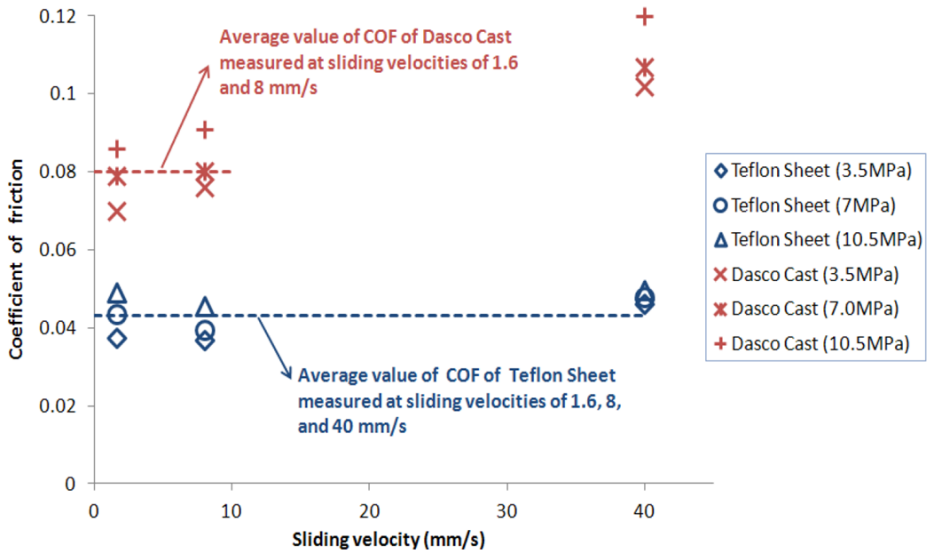

Figure 1.27 Comparison of Dasco Cast and Teflon sheet for the sliding velocities of 1.6, 8 and 40 mm/s (Bagheriasl et al., 2012).

Boba et al. (2012, 2014) conducted cylindrical cup deep drawing experiments on 1.6 mm thick AZ31B and ZEK100 magnesium sheets using Teflon sheet and dry film lubricant (Forge Ease AL 278 from FUCHS) on a 203 mm blank at temperatures ranges from 100-250 °C. Figure 1.28 shows the measured

load-displacement response from punch. They observed that the punch force was 5% greater for dry film lubricant than Teflon sheet for all tested temperatures.

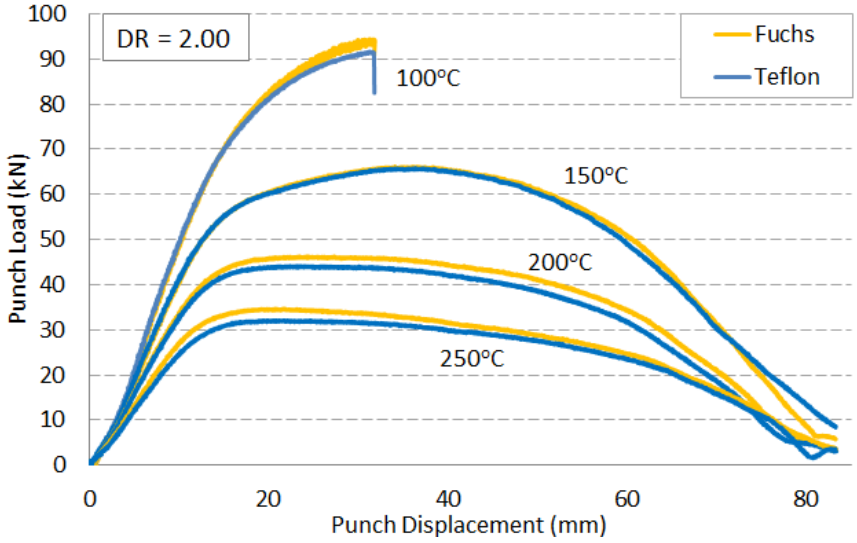

Figure 1.28 Punch load plotted against displacement for a draw ratio (DR) of 2.0 comparing Teflon and Fuchs dry lubricant (Boba et al., 2014).

1.9 Current research

An extensive body of research has been reported on the room temperature formability of aluminum alloys; however, the literature review presented in this chapter indicates that less information exists regarding the warm formability of aluminum alloy sheet. Moreover, studies considering the warm forming of AA3003 brazing sheet, the focus of the current research, are limited.

Prior research by McKinley et al. (2010) and Bagheriasl et al. (2011, 2012, 2014) on formability of brazing sheet focused on sheet thickness on the order of 0.5 mm, which corresponds to that used in so-called “core plates” used to fabricate heat exchangers for automotive engine and transmission thermal management systems. Recent application of brazing sheet materials has expanded to include battery cooler assemblies for use in electric vehicle applications. Such applications utilize much thinner sheet, on the order of 0.2 mm, mandating characterization of brazing sheet in this thickness range and understanding the influence of thickness on formability of this class of aluminum sheet.

Current practice mandates use of brazing sheet in a fully annealed O-temper condition in order to increase formability and to reduce springback (Verma, 2016). For heat exchanger applications, the rather thin nature of the sheet material (0.2 mm) makes it very difficult to handle without causing indentation or damage to the sheet; hence, there exists a strong motivation to form heat exchanger components at higher hardness levels such as the strain hardened tempers H22 or H24, referred to as "half hard" or "fully hard", respectively. Such tempers would also increase the strength of the as-formed product (Cobden et al., 1994).

Hence, the objective of the current research is to experimentally investigate the influence of forming temperature and forming speed on the formability of AA3003 brazing sheet, comprising an AA3003 core with a clad layer of AA4045. Two thickness/cladding configurations were considered, one a double side cladded 0.5 mm thick sheet in O temper condition used in core plate applications and the other a single side cladded 0.2 mm thick sheet used in batter plate applications. The core plate material was tested in the O temper condition and was used as a baseline material to assess the influence of sheet thickness. The battery plate material was tested in in the O, H22 and H24 temper conditions to assess the effect of initial temper on formability. Due to the rather low formability of O temper material reported by Bagheriasl et al. (2012), the current work focusses on characterization of the warm formability of these sheet materials under warm conditions in the range of room temperature to 250 °C. Given the strong rate sensitivity of aluminum alloy sheet at elevated temperature, the effect of forming speed is also examined.

The balance of this thesis is organized as follows. Chapter 2 presents a description of the tested materials and experimental techniques, whereas Chapter 3 includes the results of the limiting dome height experiments and forming limit curves generated for all the materials considered. Chapter 4 presents predicted FLC results obtained using the Marciniak-Kuczynski (Marciniak and Kuczynski, 1967) analysis software developed by Kurukuri (2016) and comparison with the measured FLCs from Chapter 3. Chapter 5 lays out the conclusions from the current study and Chapter 6 proposes next steps for future work.

Chapter 2

Limiting Dome Height Experimental techniques

2.1 Materials Studied

The materials considered in the current research were AA3003 brazing sheet in three different temper conditions, namely O (0.5 mm, 0.2 mm), H22 (0.2 mm) and H24 (0.2 mm). The 0.2 mm thick aluminum brazing sheet has a single side clad layer and the 0.5 mm thick O temper sheet is clad on both sides.

Some basic temper conditions are *F* (As-Fabricated), *O* (Annealed), *H* (Strain-Hardened), *W* (Solution Heat Treated) and *T* (Thermally treated to produce stable tempers other than *F*, *O*, or *H*). In the current research, tempers *O* (Annealed) and *H* (Strain-Hardened) were studied. Some divisions of the H temper are listed in Table 2.1. The nominal chemical compositions of the AA3003 alloy sheet and AA4045 clad layer are shown in Table 2.2 and Table 2.3.

Table 2.1 Subdivisions of *H* temper (Strain Hardened)

First digit indicates basic operations:	Second digit indicates degree of strain hardening:
H1 – Strain Hardened only	HX2 – Quarter hard
H2 – Strain hardened and partially annealed	HX4 – Half hard
H3 – Strain hardened and stabilized	HX8 – Full hard
H4 – Strain hardened, lacquered or coated	HX9 – Extra hard

Table 2.2 Nominal chemical composition of AA3003 alloy sheet

Weight (%)	Al	Cu	Si	Fe	Mn	Zn	Others
AA3003	Remaining	0.05-0.20	0.60	0.70	1.0-1.5	0.10	0.05 each

Table 2.3 Nominal chemical composition of AA4045 sheet

Weight (%)	Al	Cu	Si	Fe	Mn	Zn	Others
AA4045	Remaining	0.30	0.09-0.11	0.80	0.05	0.10	0.05 each

2.2 Tensile Properties

Detailed characterization of the sheet materials considered in this research was performed by Verma (2016) and Kurukuri (2016) as part of related work on the same batches of material. Verma (2016) considered the 0.2 mm O, H22 and H24 temper sheet, while Kurukuri (2016) considered the 0.5 mm O temper sheet. Both studies comprised uniaxial tensile experiments at strain rates of 0.002 or 0.02 s^{-1} and temperatures ranging from 25-250 °C. The tests were conducted on an Instron universal testing machine located at the CanmetMATERIALS facility in Hamilton, Ontario. The test set-up is shown in Figure 2.1, while the specimen geometry used in both studies is shown in Figure 2.2. A biaxial video extensometer was used to measure the longitudinal and transverse strain in the specimen during testing, as shown in Figure 2.3, which shows the specimen mounted in the grips with the extensometer markers. The experiments were started once the temperature had stabilized to the desired test temperature (10, 15 and 20 minutes to reach 150, 200, and 250 °C, respectively).

Figure 2.1 The test set-up for the tensile experiments at CanmetMATERIALS (Verma, 2016).

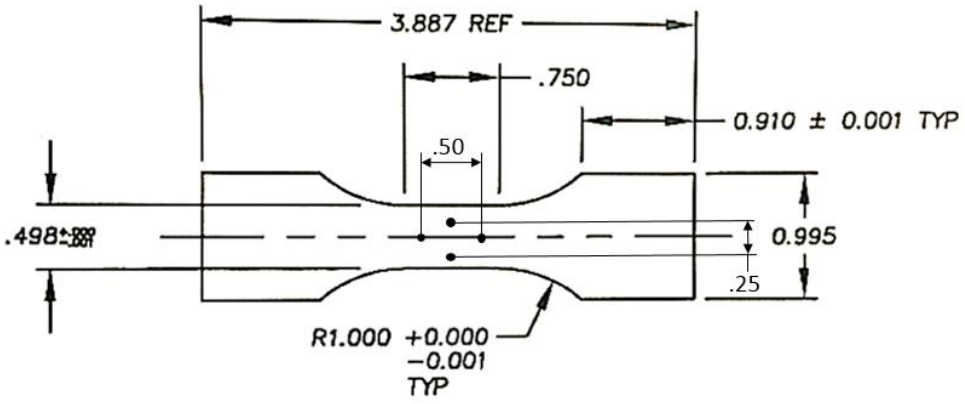

Figure 2.2 Schematic of the tensile test specimen used by Verma (2016) and Kurukuri (2016). All dimensions are in inches.

Figure 2.3 Tensile test specimen mounted on the experimental set-up (Verma, 2016).

Figure 2.4 shows the effect of material temper on the true stress-strain curves at RT, 0.02 s^{-1} in the rolling direction (RD) (Verma, 2016; Kurukuri, 2016). As seen from the figure, the H24 temper showed higher yield strength of ~210 MPa as compared to the H22, O temper materials. The H22 and H24 tempers also showed lower ductility as compared to both fully annealed O temper sheet materials (0.5 and 0.2 mm). The two O temper sheets had similar behavior and strong work hardening relative to the H22 and H24 tempers.

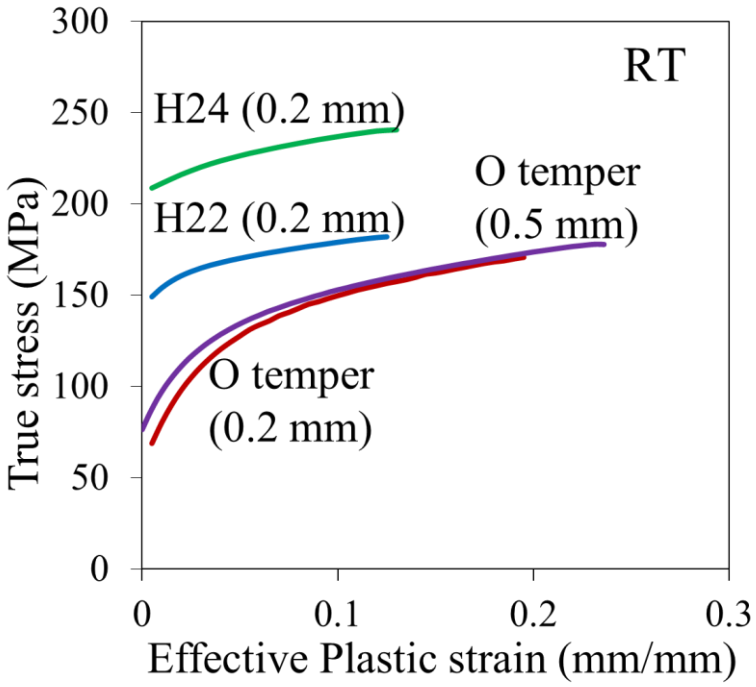

Figure 2.4 Comparison of flow curves for different material tempers at RT, 0.02 s^{-1}.

Verma (2016) and Kurukuri (2016) examined the effect of temperature and strain rate on the tensile response of these materials, as shown Figure 2.5. They observed that all three temper conditions exhibited an increase in the ductility and reduction in strength with an increase in the temperature. The fully annealed O temper sheets maintained a positive work hardening over the entire temperature range, whereas the H22 and H24 sheet showed negative hardening behavior at elevated temperatures. The materials were not very sensitive to strain rate at RT; however, Verma (2016) and Kurukuri (2016) observed strong positive strain rate sensitivity at elevated temperatures.

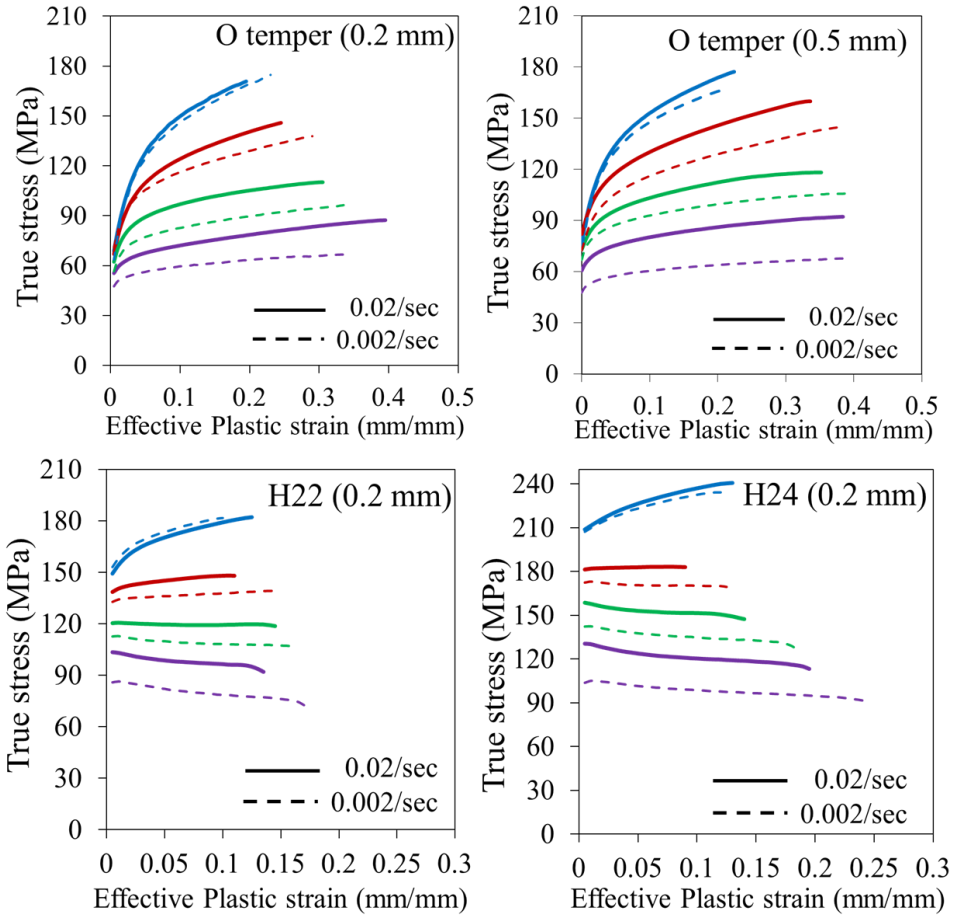

Figure 2.5 Flow curves comparing two strain rates of 0.002 s^{-1} and 0.02 s^{-1} for different temper conditions at RT, 150 °C, 200 °C and 250 °C.

2.3 Experimental Apparatus and Tooling

All LDH experiments performed as part of this research were conducted on a servo-controlled hydraulic press located in the High Pressure Laboratory, at the University of Waterloo (Figure 2.6). The tooling was affixed within a die set mounted on the sliding platens on the hydraulic press to ensure the alignment.

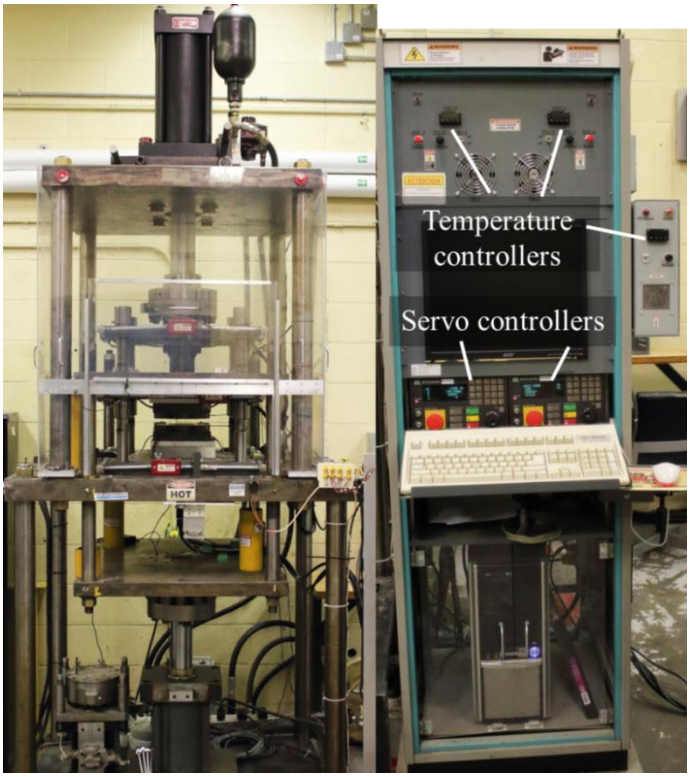

Figure 2.6 Photograph of the LDH experimental setup (left) and computer control rack (right).

The warm tooling, shown in Figure 2.7, was developed by Bagheriasl et al. (2012) and was used in the current work to perform the high temperature LDH experiments. Each tooling component was equipped with cartridge heaters capable of heating the tooling to 400 °C. The punch contains six 9.5 mm diameter, 600 Watt resistance cartridge heaters. Ceramic insulation is used to limit the heat transfer between tooling and the rest of the frame. Figure 2.8 shows a close up schematic view of the warm forming tooling. During the experiments, the punch and blank holder were moved by two hydraulic actuators and the die was fixed. Load cells inserted between the actuators and their respective tooling measured the actuator force which has a maximum capacity of 890 kN (200 kip). The displacements were measured using linear variable differential transformer (LVDT) transducers.

The maximum clamp and punch force capacities are 750 kN (168 kip) and 890 kN (200 kip). Thermocouples were attached to the tooling near the tooling surface to permit more accurate temperature control via temperature controllers (Omega CNi3254-C24). The punch was under displacement control and both displacement and load were recorded; the blank holder was under load control and displacement and load were recorded. The actuators were controlled via MTS 407 servo controllers and a customized

LabView program controls the function of the entire apparatus. A data acquisition card (DAQ) by National instruments was attached to PC to record experimental data, such as binder and punch force and displacement, and provide program signals to the servo controllers.

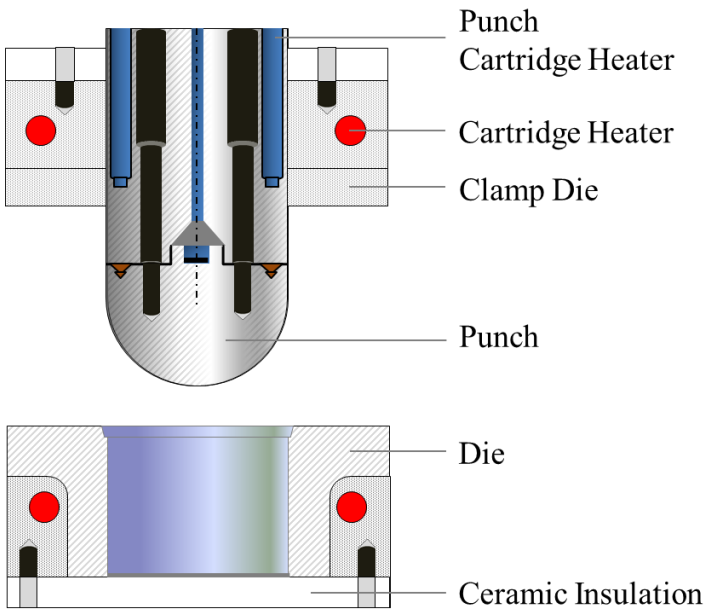

Figure 2.7 Schematic diagram of the LDH tooling set (Bagheriasl et al., 2013).

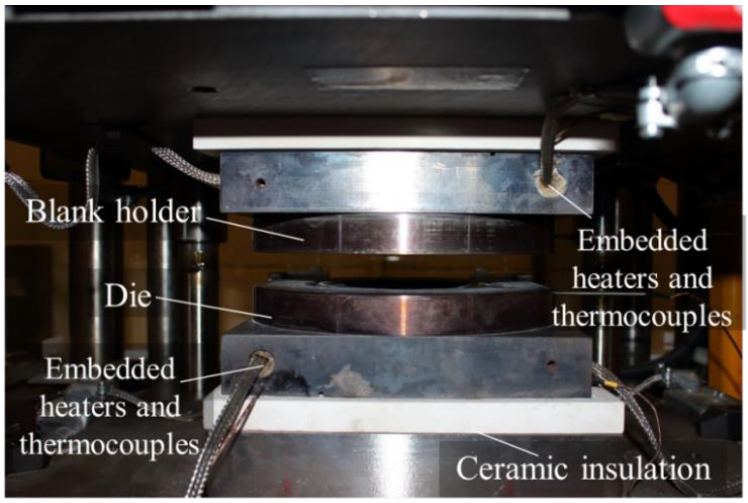

Figure 2.8 Close up view of the warm forming tooling.

2.3.1 Lubrication

All testing was done using 0.05 mm thick Teflon sheet as a lubricant. The Teflon sheet was placed between the punch and the blank for all of the LDH experiments. From the previous studies by Bagheriasl et al. (2013), the room temperature coefficient of friction for the Teflon sheet was found as 0.043 for AA3003 brazing sheet. The elevated temperature coefficients are yet to be ascertained. As there is a difference in the sheet thicknesses and the considered temperature ranges involved in the current research, the number of Teflon sheets needed between the samples also varies. By conducting series of experiments with different number of Teflon sheets, it was observed that placing 4-5 layers of Teflon sheet promotes near center failure, especially for soft tempered (O temper) biaxial specimens (203.2 mm x 203.2 mm). Table 2.4 shows the number of Teflon sheet used for the various temperatures and sheet thicknesses. In general, it was found that additional Teflon layers were needed for soft (O temper) brazing sheet material at higher temperatures in order to promote failure near the center of the punch.

Table 2.4 Comparison of amount of Teflon sheets required for various temperatures and thicknesses

Thickness of the sheet	Number of Teflon sheets used at			
	RT	150 °C	200 °C	250 °C
0.2 mm (H22, H24 and O temper)	4	4	4	5
0.5 mm (O temper)	4	4	5	5

Teflon film is not a widely accepted lubricant material in industrial production processes because of cost and complexity of its use in those processes. It is used often for formability studies, however, due to the low friction coefficient it provides which promotes failure of the sheet material at the center of the punch region, in accord with ISO 12004 formability testing standards.

To investigate alternate lubricants for high temperature forming, a number of experiments were performed using water/oil-based lubricants that have a higher potential for use in industrial production processes since they are applied directly on to the surface of the material to be formed. A limited study was done to compare the influence of friction on the dome height of an O temper (0.5 mm) 203.2 mm x 203.2 mm biaxial stretch specimen at 0.4 mm/s, 200 °C. Five types of dry film lubricants, namely OKS 536, Lubrodal F 400, Diacut NCL, MXC 2187 and Teflon (referred as 3T - 3 sheets of Teflon), were considered in the study, shown in Figure 2.9. The dome height at failure measured for Teflon sheet was lower by up to 3% for all tested lubricants except for the OKS and Lubrodal. In spite of having higher

dome heights, Diacut and MXC were found to be too smoky at higher temperatures whereas Lubrodal and OKS evaporated and had too high friction at higher temperatures. Therefore, Teflon was considered the best choice as a lubricant to use for the balance of the current research.

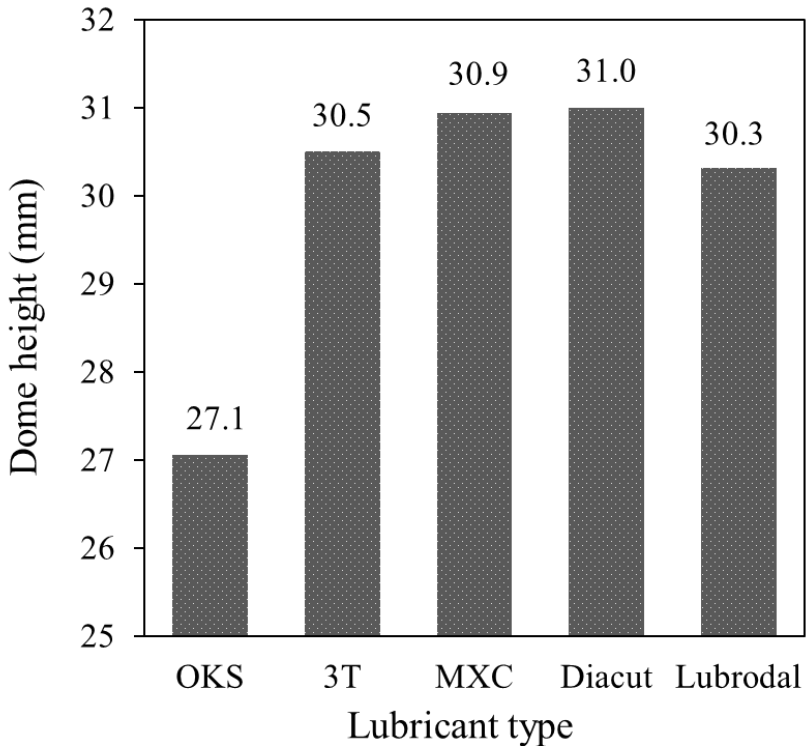

Figure 2.9 Effect of friction on the dome height at failure of an O temper biaxial specimen at 200 °C.

2.3.2 Specimen geometry

As per ISO-12004, it is necessary to use the blanks with different widths to obtain different strain paths (different ratios between major and minor true strain, ε_1 and ε_2, respectively) to produce the FLDs. Figure 2.10 shows the different specimen geometries (ISO-12004-2) used in the current investigation, namely 25.4 mm (1 in.) dog-bone, 50.8 mm (2 in.) dog-bone, 76.2 mm (3 in.) dog-bone, and 203.2 mm x 203.2 mm (8 in. x 8 in.) biaxial stretch. A 25.4 mm (1 in.) dog-bone specimen when placed on the die, along with the inner and outer radii of the die is shown schematically in Figure 2.11. The specimen geometries represented uniaxial stretching (25.4 mm dog-bone, $\varepsilon_1 = -2\varepsilon_2$), intermediate tensile strain (50.8 mm dog-bone), plane strain (76.2 mm dog-bone, $\varepsilon_2 = 0$) and biaxial stretching (203.2 mm x 203.2 mm, $\varepsilon_1 = \varepsilon_2$). All

the samples considered in this work were machined by aligning the specimen major axis with the rolling direction.

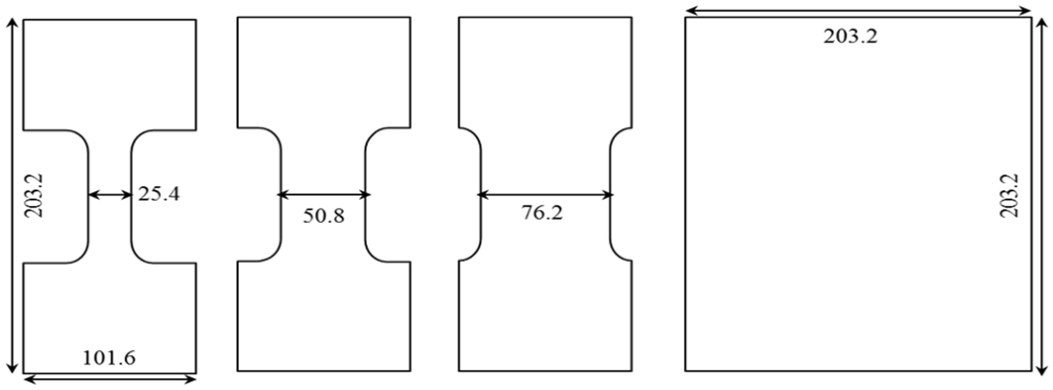

Figure 2.10 Schematic of the Limiting dome height (LDH) test geometries as per ISO-12004-2 (All dimensions are in mm).

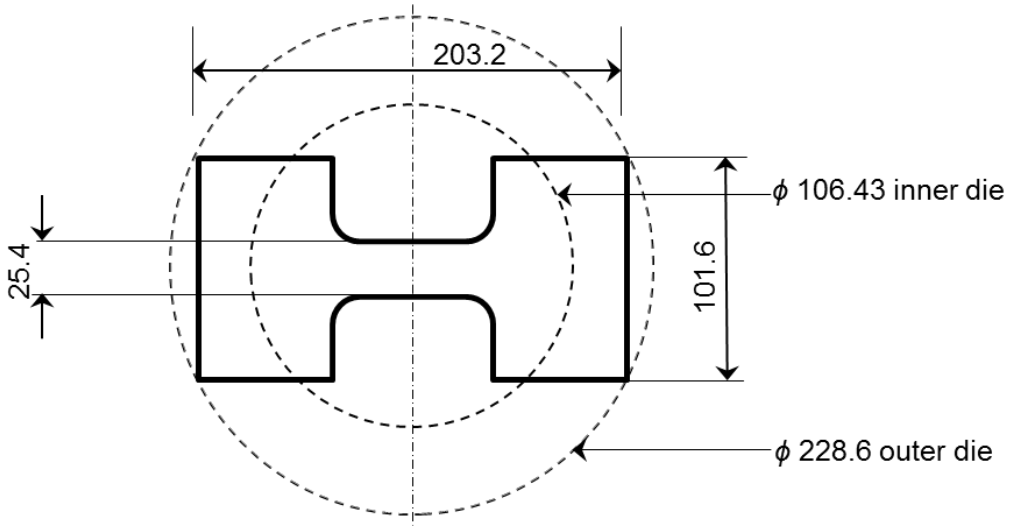

Figure 2.11 Schematic showing the positioning of the 25.4 mm (1 in.) dog-bone specimen relative to the die outline (all dimensions are in mm).

2.4 Experiments

Limiting Dome Height (LDH) experiments were performed to obtain formability data for the AA3003-O, AA3003-H22, and AA3003-H24 brazing sheet alloys. The LDH test involves stretching of a sheet specimen over a hemispherical punch until necking and failure/fracture occurs. The dome height of the stretched sample is then recorded as the Limiting Dome Height (LDH) for that particular material and specimen width (strain state). All of the LDH experiments carried out for this thesis, involved different specimen geometries and Digital Image Correlation (DIC) techniques were used for strain measurements on deformed specimens. These experiments were used to produce Forming Limit Curves (FLCs) for the considered range of temperatures and forming speeds.

2.4.1 Binder force

Initially the LDH tooling used a die and blank holder that incorporated a set of lock beads (Figure 2.12) to minimize the effect of material draw in. Unfortunately, the lock bead resulted in tearing of the sheet at the lock bead. Instead, the LDH experiments were performed using flat dies without lock beads in order to avoid tearing of these rather thin (0.2-0.5 mm), soft specimens.

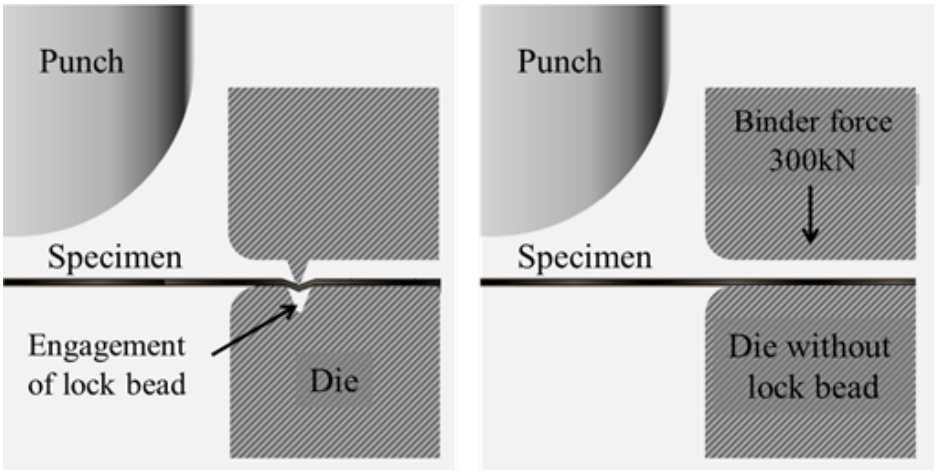

Figure 2.12 Initial LDH tooling with the engagement of lock bead (left); LDH tooling used in the current investigation without lock bead (right).

Preliminary experiments were performed to select the appropriate binder force (also known as the Blank Holder Force, BHF) prior to performing the LDH experiments. Excessive binder force can cause cracking at the dome edge due to tearing whereas low binder forces can result in wrinkling of sheet material in the flange area. The following criteria were applied used to select the appropriate Blank Holder Force (BHF):

- BHF should be high enough to stop the specimen from drawing into the dome
- BHF should be low enough to not cause fracture at the edge of the dome.

A series of experiments were conducted to evaluate suitable binder forces for each specimen geometry, sheet thickness and temperature condition, from which it was concluded that binder forces higher than 320 kN caused fracture at the dome edge, while forces lower than 280 kN resulted in the increased dome height and draw in (Figure 2.13). Therefore, for all the specimen geometries, thicknesses and temperatures, a BHF of 300 kN was adopted.

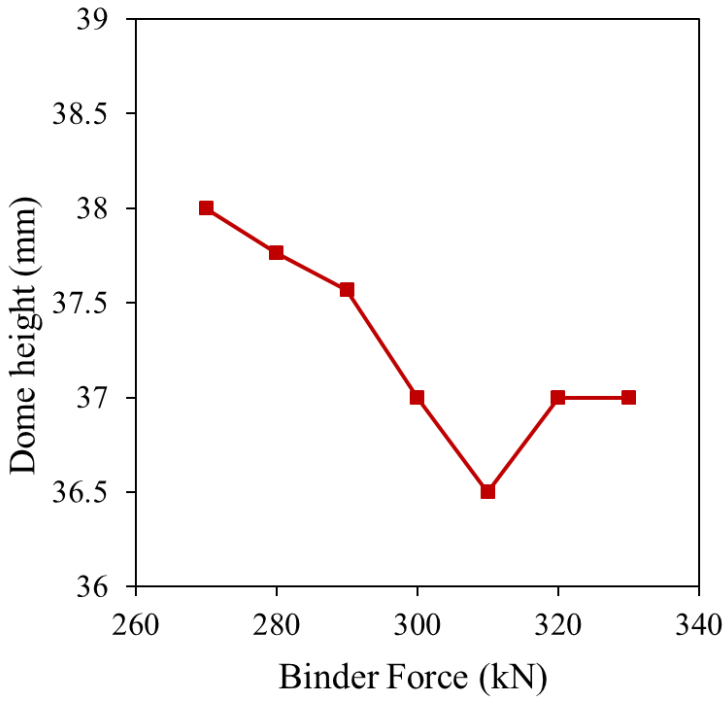

Figure 2.13 Graphical representation of the effect of binder force on dome height at 250 °C for O temper, 0.5 mm thick sheet.

2.4.2 Temperature distribution

Experiments were performed to identify the time required for the specimen to reach the desired test temperature. These experiments were performed using specimens instrumented with thermocouples to record the temperature transients during heating (Figure 2.14). For this study, thermocouple wires were attached to the specimen using screws. It is recognized that the thermal mass of the screws could delay the specimen temperature reaching the desired temperature (locally); however, it is thought that the time to reach temperature determined in this manner should be conservative. The instrumented specimens had thermocouple wires positioned at C_1, C_2 (center of the specimen) and C_3 (as shown in Figure 2.14), that were connected to an Omega OMB-DAQ-55 personal DAQ system.

Figure 2.14 Photograph of a 203.2 mm x 203.2 mm specimen used in the temperature distribution study.

Firstly, the LDH tooling set was heated to the desired temperature (confirmed by thermocouples installed on each tooling component) and the instrumented specimen was loaded onto the die. At this point, the recording of the temperature begins using the thermocouples and DAQ system. The specimen was then clamped by the blank holder and the punch was lowered to engage the specimen with an offset

of 0.5 or 0.2 mm, corresponding to the sheet thickness. Figure 2.15 shows the temperature time histories for a range of blank thicknesses and die temperature conditions. The times at which the punch first contacts the blank and when the blank holder and die were closed together are indicated in Figure 2.15 by the vertical dashed lines. After the tools closed, the specimen was then given time to reach the desired test temperature (100 seconds for the 0.2 mm material and 120 seconds for the 0.5 mm material). As seen from Figure 2.15, the heating curves start at room temperature and then there was a rise in the temperature between the times at which the specimen was clamped and the punch was positioned before forming starts.

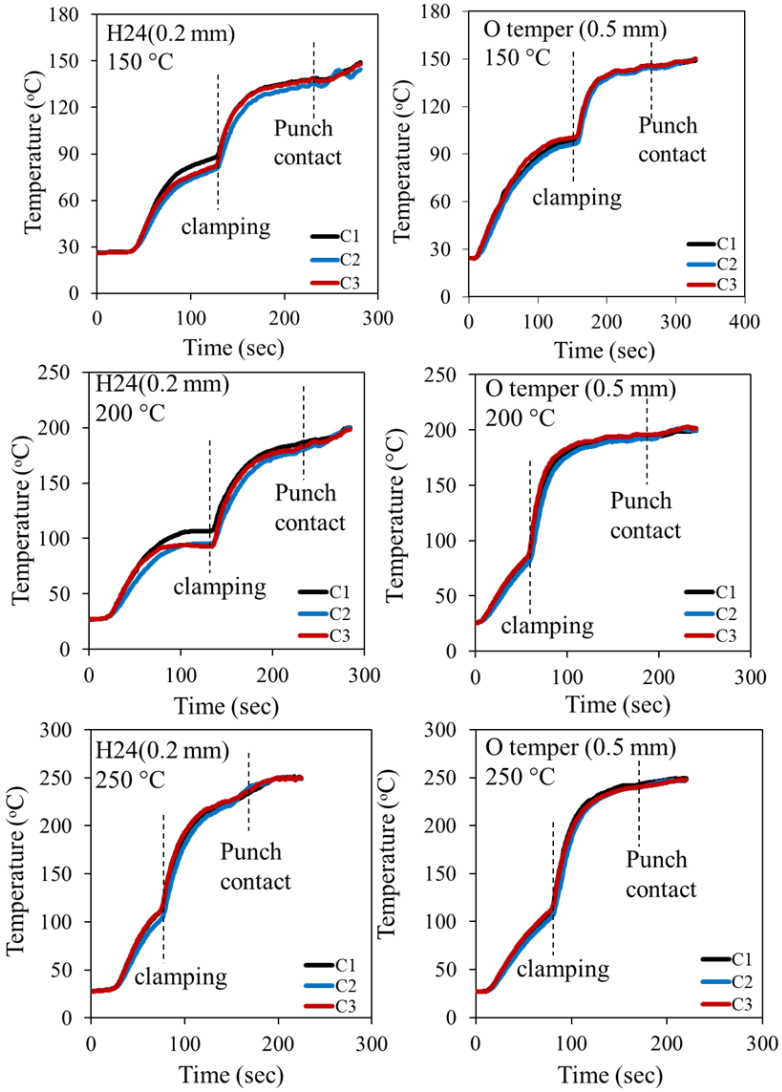

Figure 2.15 The heating time profile for a 203.2 mm x 203.2 mm specimen.

2.5 Experimental procedure

The warm formability experiments require heating of the tooling to isothermal conditions. The die, blank holder and punch are heated prior to each test to the targeted temperature and allowed sufficient time to attain equilibrium temperature and become stable. The temperature level was confirmed prior to every test. For each of the LDH experiments, the following procedure was followed:

- Load the blank into the press and start the LabView program.
- Clamp the dies to a predetermined binder force.
- Lower the punch to contact the blank in place and apply a pre-displacement equal to sheet thickness to heat the central region of the blank.
- Allow adequate heating time (100 seconds for the 0.2 mm material and 120 seconds for the 0.5 mm material) to reach the targeted temperature.
- Initiate punch movement at the specified speed (0.4 or 1.6 mm/s) to deform the sheet specimen. Simultaneously start the DIC data collection system.
- Stop the test upon visible failure of the specimen occurs.

Forming speeds of 0.4 and 1.6 mm/s and temperature values of 25 °C, 150 °C, 200 °C and 250 °C were investigated in the current work. LDH tests for each condition considered were repeated three times to check the repeatability of the results. Teflon sheets were placed on the uncoated side of the brazing sheet (except O temper-0.5 mm thick sheet which was coated on both sides) for all experiments.

2.6 Digital Image Correlation (DIC) technique

The three dimensional DIC technique is an optical in-situ strain measurement method, which capture images during mechanical testing and analyzes them using the mathematical correlation method (Sutton et al., 2009). In the present work, two high-resolution 4.1 MP Point Grey Gazelle cameras (Model: GZL-CL-41C6M-C) with a maximum resolution of 2048x2048 pixels and maximum framing rate of 150 frames per second (fps) were used to capture images of the speckled specimens during deformation (Figure 2.16). The cameras were situated underneath the die opening to capture images of the blank throughout the forming process (Figure 2.17). After testing, DIC analysis using the Vic-3D software, from Correlated Solutions Inc., was used to calculate the forming strain history. The specimen was illuminated using LED lights which were adjusted to deliver even illumination across the entire specimen. The DIC system allows for adjusting processing parameters like subset size and step size at the start of

each analysis which allows balance between processing speed and resolution. The subset size of the DIC system indicates the pixel quantities used for comparison of two consecutive images and corresponds to a size of 2.5 mm on the blank surface which is equivalent to the size of the grid used in the circle grid analysis technique for measuring strains in forming experiments. The step size is related to the resolution of the analysis; a step size of 1 means correlation analysis will be performed on every pixel of the area of interest and a step size of 7 means it will be performed on every 7^{th} pixel in the area of interest. The DIC analysis conducted on the current work used a subset and step size of 29 pixels and 7 pixels, respectively, chosen to provide an acceptable projection error in the range of 0.007-0.034. The "exhaustive search option" was adopted which causes the DIC software Vic-3D to repeat a coarse search for matches after each time the correlation fails and results in more data recovery but increased processing time. The deformation history recorded using the DIC system for each specimen was later used to determine the failure strains and the onset of necking (detailed description is provided in chapter 3).

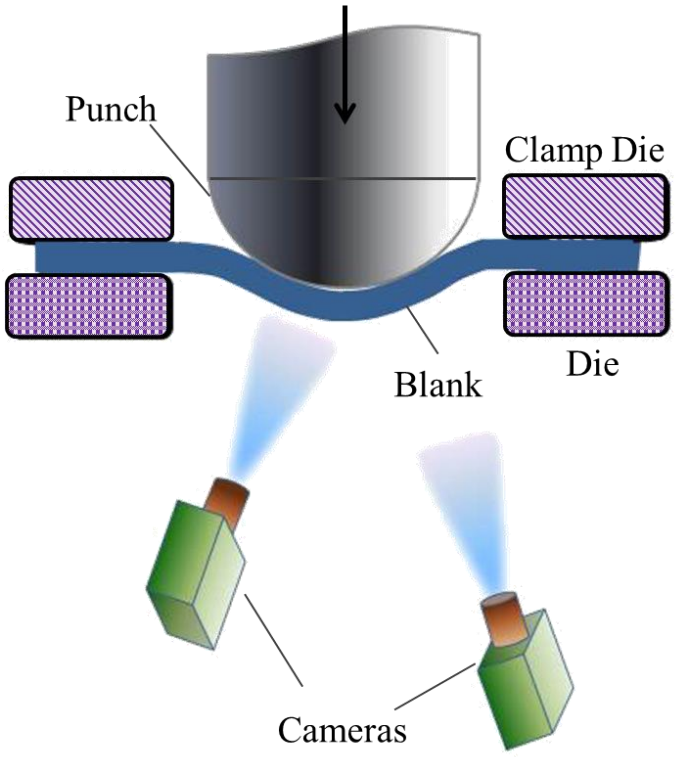

Figure 2.16: Schematic image of the DIC cameras and LDH tooling arrangement.

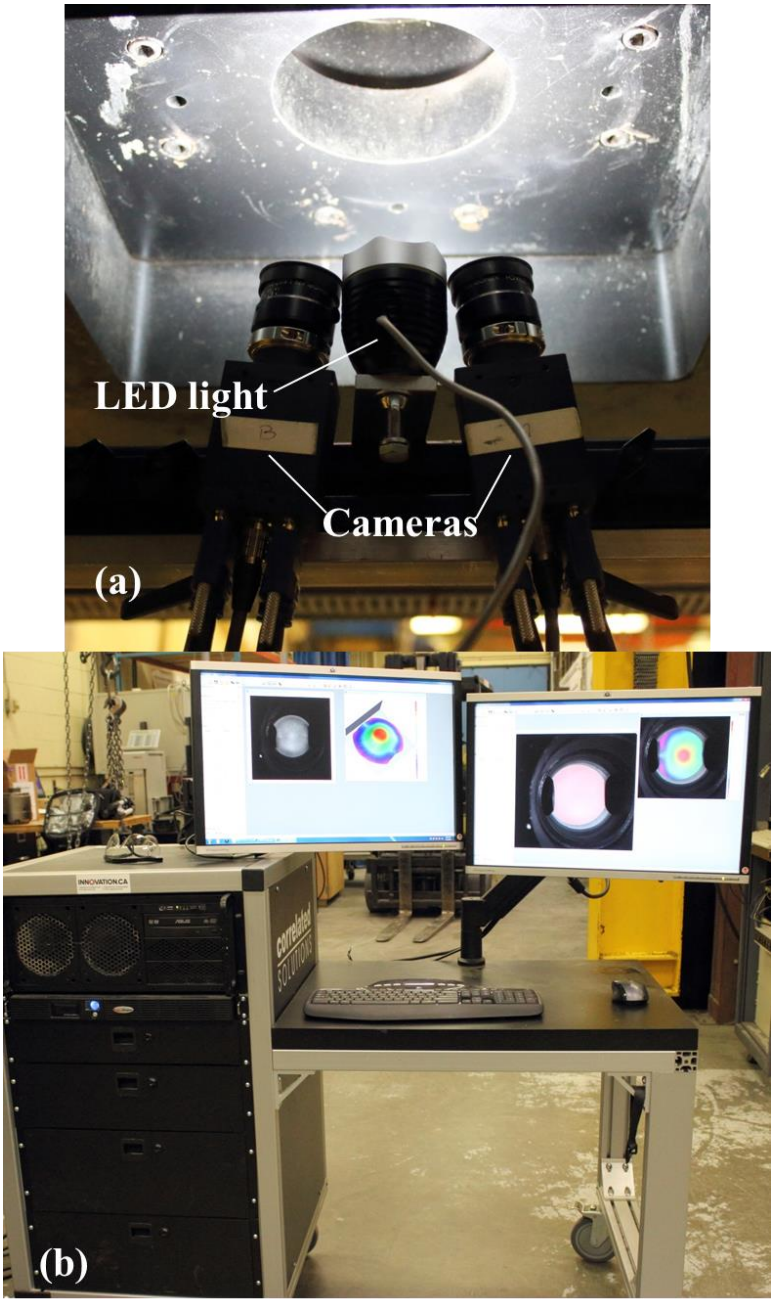

Figure 2.17 (a) Picture of the DIC cameras mounted under the LDH tooling, (b) Photograph of the DIC computer control rack.

2.6.1 Specimen preparation

The DIC system detects the geometrical changes on the area of interest which is speckled to provide a high contrast image with randomly distributed black dots over a white background. The speckle pattern was applied by coating the AA3003 sample with a layer of white paint (high temperature white paint was used for elevated temperature). Later, black speckles were applied by spraying a black paint. Figure 2.18 shows images of the four specimen geometries after speckling.

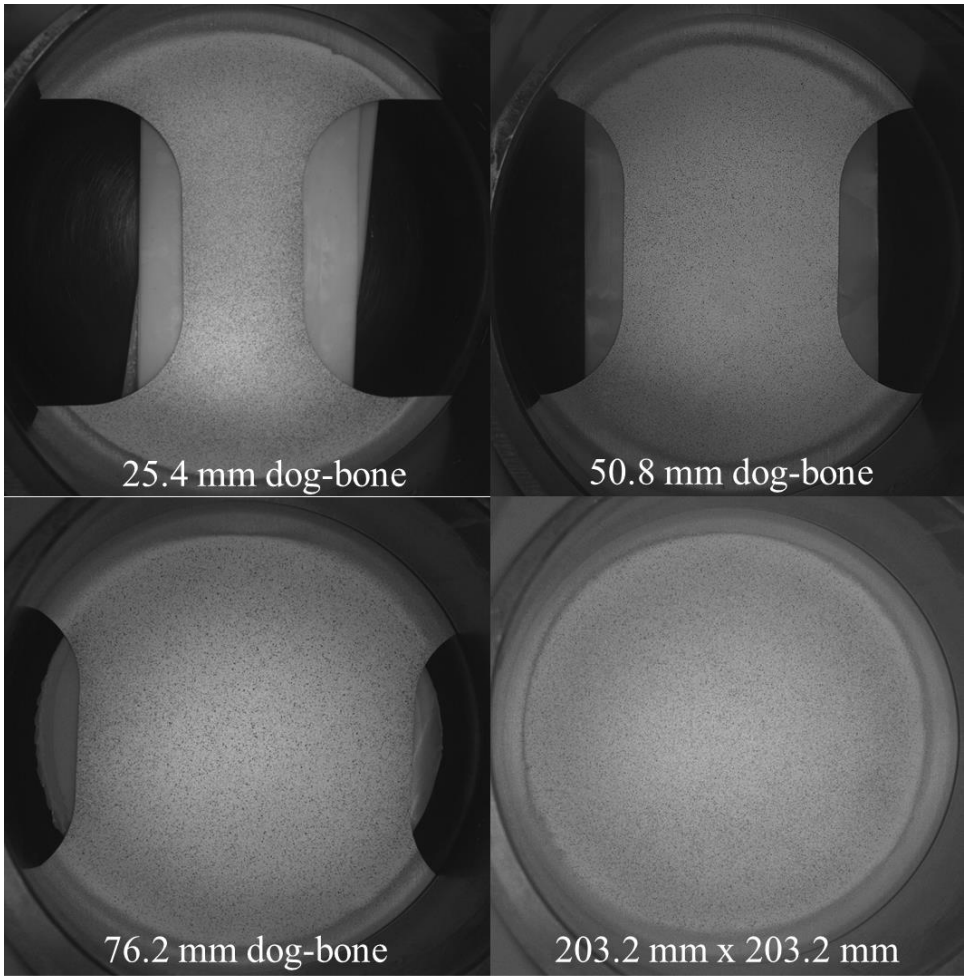

Figure 2.18 Photograph of the speckled specimens.

Chapter 3
Forming Results and Discussions

Experimental results from warm formability characterization of the AA3003 brazing sheet for the three temper conditions and two thicknesses considered in this work are presented in this chapter. The materials considered include 0.5 mm O-temper sheet and 0.2 mm sheet in the O- H22- and H24-temper conditions. Formability data was acquired at temperatures ranging from room temperature (RT) to 250°C, at forming speeds of 0.4 and 1.6 mm/s.

Measured Limiting dome height (LDH) values are presented first, after which the results from the limit strain determination is presented. Forming limit curves (FLCs) were developed using limit strain values extracted using the linear best fit time-dependent method (Volk and Hora, 2010).

3.1 Experimental data processing – detection of limit strains

In the LDH experiments, the different sample geometries used to develop the FLDs were deformed until fracture. The onset of necking was determined using the strain measurements obtained from the DIC system as outlined in the following. Figure 3.1 shows the images of fractured (a) biaxial specimens, (b) 50.8 mm (2 in.) wide dog-bone specimens deformed at RT, 0.4 mm/s with a clamping force of 300 kN. Figure 3.2 shows the images of fractured (a) biaxial specimens (b) 50.8 mm (2 in.) wide dog-bone specimens deformed at 250 °C with a punch speed of 0.4 mm/s and clamping force of 300 kN. In general, fracture occurred near the pole of the punch, but was often offset from the pole by 13-15 mm. These observations suggest that the lubrication scheme was working relatively well.

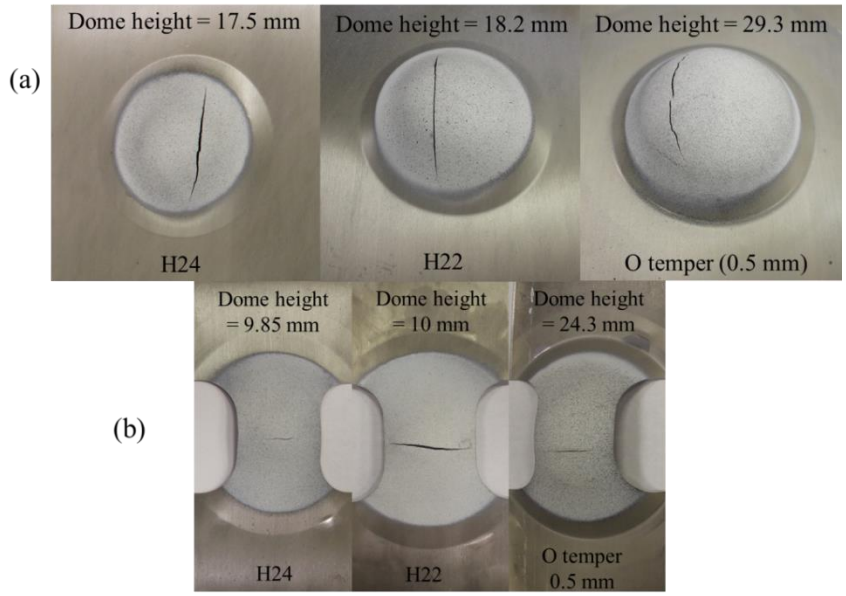

Figure 3.1 Image showing fracture of (a) 203.2 mm x 203.2 mm (biaxial) specimens, (b) 50.8 mm (2in.) dog-bone specimens formed at RT, 0.4 mm/s for different materials.

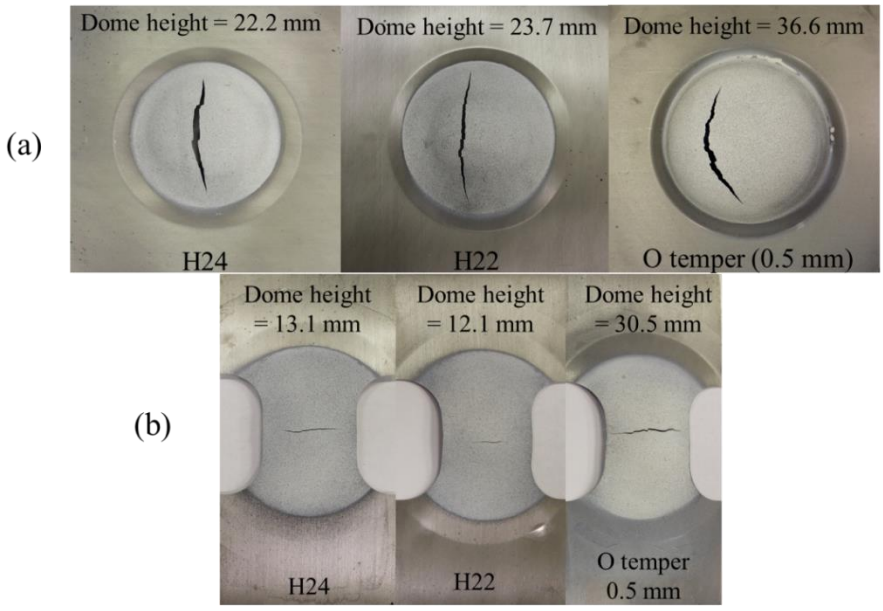

Figure 3.2 Image showing fracture of (a) 203.2 mm x 203.2 mm (biaxial) specimens, (b) 50.8 mm (2in.) dog-bone specimens formed at 250 °C, 0.4 mm/s for different materials.

The strains are calculated, the major and minor strain fields were determined for all the captured images and results such as major and minor strain components and displacements can be presented in 2-D and 3-D contour plots. Figure 3.3 shows typical 2-D and 3-D plots of displacement for a 76.2 mm (3 in.) wide dog-bone specimen.

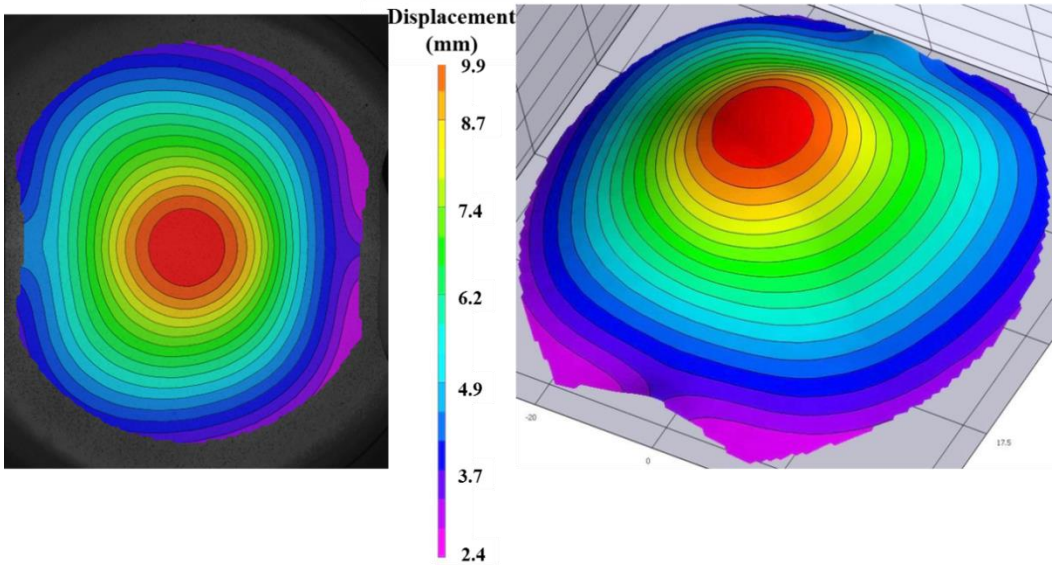

Figure 3.3 2-D and 3-D displacement contour plots for 0.2 mm thick H24 plane strain (76.2 mm wide dog-bone) specimen.

The DIC system records the history of the field variables throughout the forming process. The contour plots of major strain (e_1) distribution for a 76.2 mm (3 in.) wide dog-bone specimen formed at RT and 250 °C with a punch speed of 1.6 mm/s and clamping force of 300 kN are presented in Figure 3.4. For both temperatures, the contour plots are presented at dome heights of 7 mm, 15 mm and 19.9 mm. As seen from Figure 3.4, the major strain distributions at RT localized earlier in the deformation process and presented a lower dome height at failure relative to the 250 °C sample. On the whole, increasing the temperature to 250 °C increased the dome height and formability for AA3003 brazing sheet.

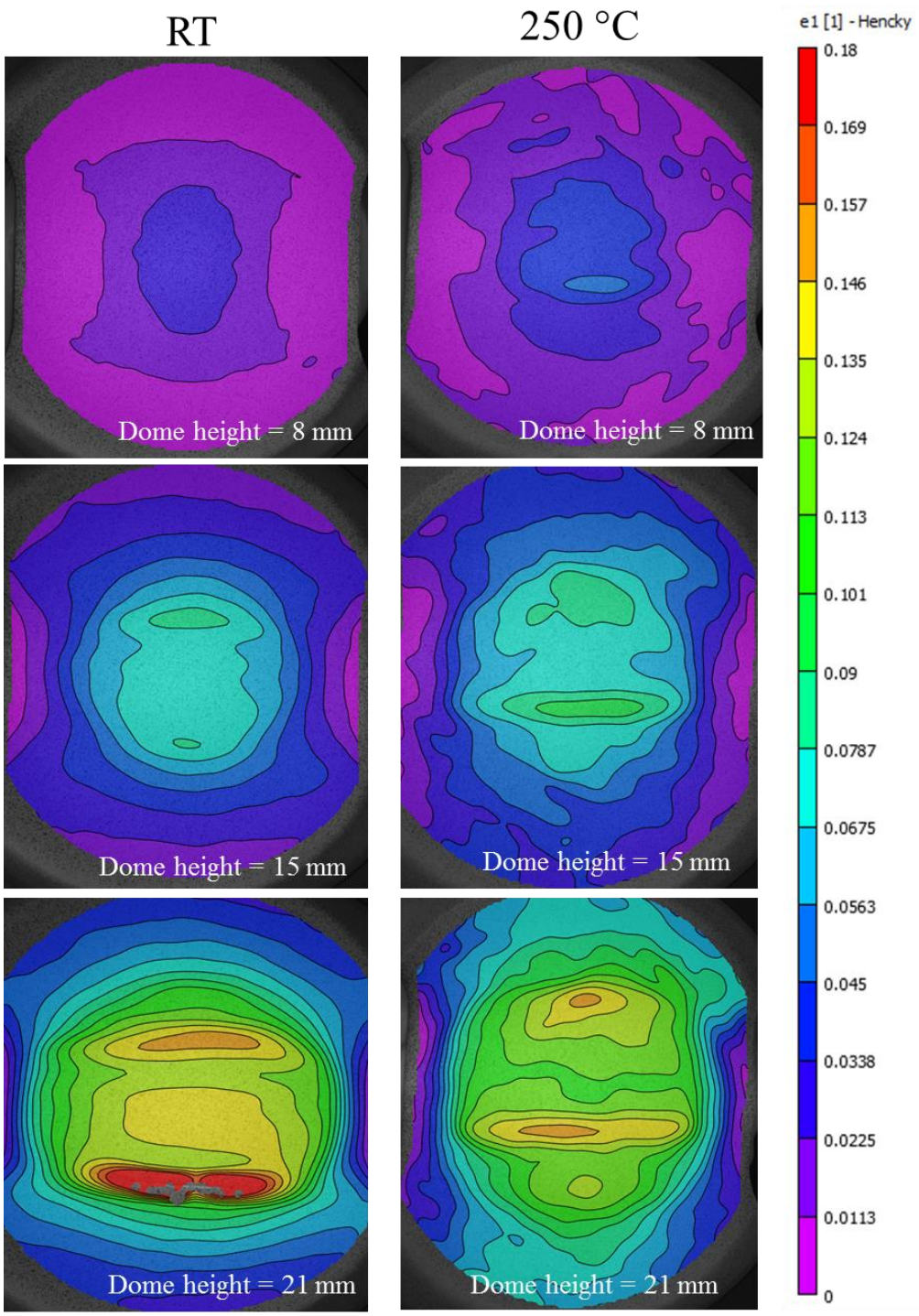

Figure 3.4 Contour plots of major strain distribution for an O temper (0.5 mm thick), 76.2 mm wide dog-bone sample at a forming speed of 1.6 mm/s.

The measured major versus strains from the formability tests were plotted in strain space to produce a strain path history. Figure 3.5 shows detailed strain path histories for 0.2 mm thick O-temper samples tested at 250 °C as extracted by the DIC system. Three repeat experiments were performed for each condition and the median curve is shown in Figure 3.5. Similar strain path histories were observed for other tested materials (H22, H24 and 0.5 mm thick O temper).

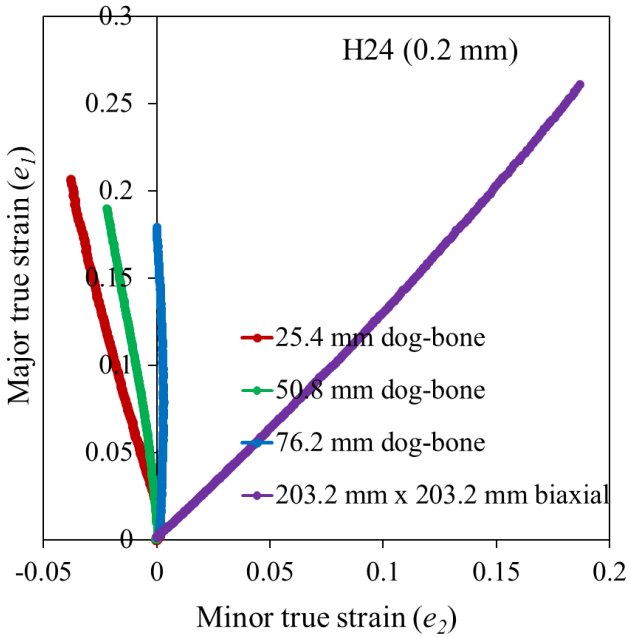

Figure 3.5 Strain path histories for O-temper (0.2 mm thick) samples at 250 °C, 0.4 mm/s.

Initially the ISO method (cross-section method) was adopted in the present work to measure the forming limit strains. The steps followed in the ISO method are given in section 1.7.1. As seen in Figure 3.6, due to multiple peaks in the specimen, the left best-fit window can contain a part of the second peak leading to an incorrect or skewed fit of the inverse parabola. Therefore, the major limit strain obtained in this case was greater than the actual fracture strain at the crack location which is not correct. To avoid this issue, time-dependent FLC determination methods based on the time history of measured strains were considered to determine the forming limits. One of the time-dependent FLC evaluation methods termed the “linear best fit method” proposed by Volk and Hora (2010) was adopted (a detailed description is given in section 1.7.1).

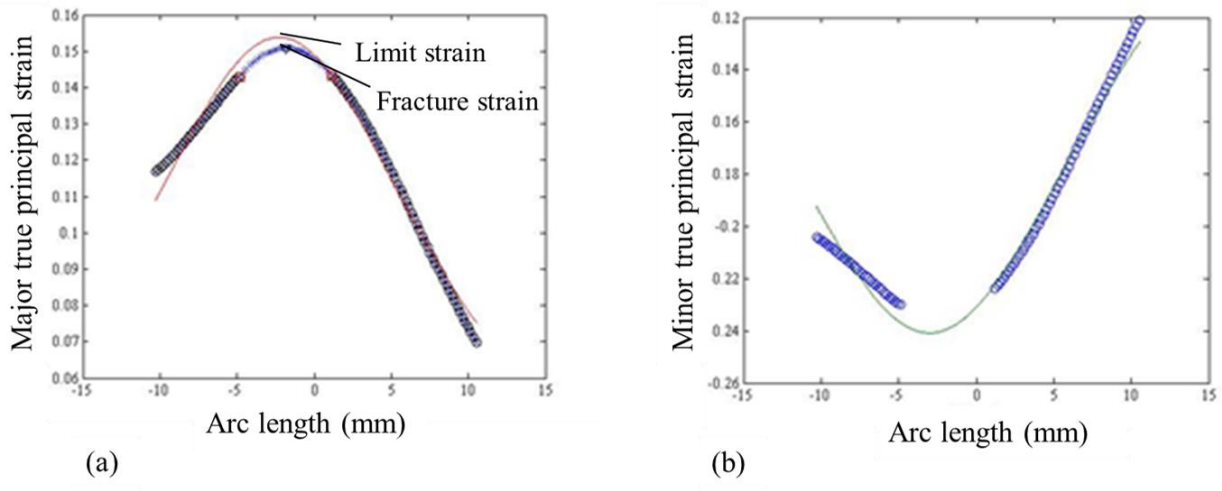

Figure 3.6 ISO method showing (a) Major limit, and (b) Minor limit identification for a 76.2 mm dog-bone 0.2 mm, H24 material.

The linear best fit method is based on the temporal analysis of the thickness strain, e_3 and its first derivative (the thickness strain rate, $\dot{e}_3$) at positions in the failure region. The thickness stain is determined from the measured in-plane strain components using a volume constancy assumption; thickness strain, e_3 = - (major strain, e_1 + minor strain, e_2), due to volume constancy $e_1 + e_2 + e_3 = 0$.

Two straight lines are calculated using regression analysis along the representative thinning rate evolution over the last 30 images before specimen failure for a punch speed of 1.6 mm/s and 60 images for 0.4 mm/s. One line is fit to the data from the stable deformation stage and the other through the last stage just before specimen failure. The intersection of these two lines is identified as the onset of the plastic instability as shown in Figure 3.7. In order to reduce the noise in the time derivative of thickness strain, a least squares parabolic fit is made for seven points in a manner similar to a moving or running average data smoothing. The time derivative of thickness strain is calculated from this parabolic equation at the given time step, as described in ISO 12004-2 (2008). Similar to the ISO 12004-2 (2008) approach, the method described above is applied to five adjacent locations in the localized necking zone and the final limit strain is considered as the average value of the strains determined in the aforementioned locations.

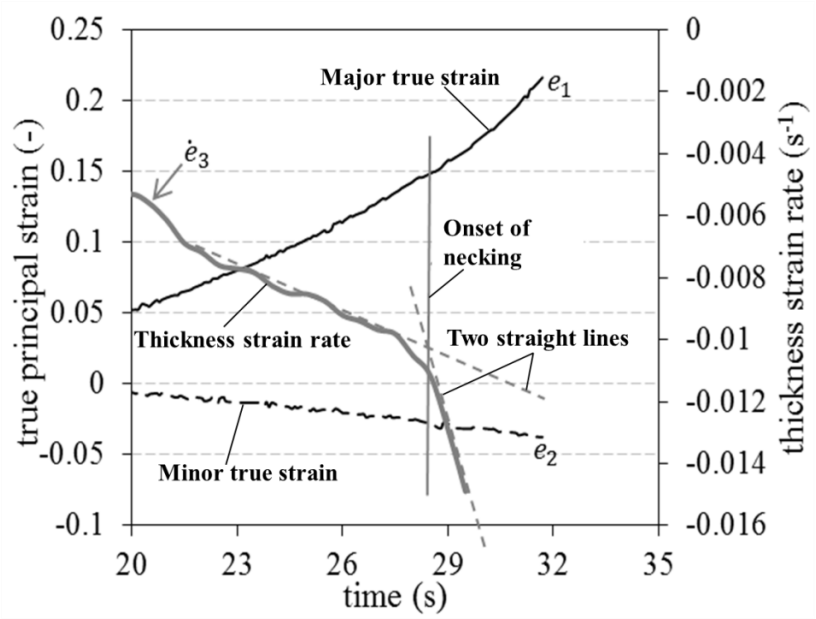

Figure 3.7 Procedure for the identification of onset of plastic instability of a 25.4 mm wide dog-bone sample using the linear best fit time–dependent method.

3.2 Influence of temperature on limiting dome height

LDH experiments were conducted on the 0.5 mm O-temper and 0.2 mm O-, H22-, and H24-temper material at RT, 150 °C, 200 °C and 250 °C to observe the effect of temperature on dome height. The experiments were performed using a clamping force of 300 kN, forming speed of 0.4 mm/s and Teflon film as a lubricant. Dome heights at necking were recorded from the images captured by the DIC system during the forming. The dome heights are reported for the image that was identified as the onset of necking. These dome height measurements showed good agreement with the measured punch force versus punch displacement data (Figure 3.8) recorded using the Labview program during the forming experiments at each temperature and material condition. The sharp decline in load seen in Figure 3.8 indicated the fracture of the specimen, whereas, the slope reduction during forming at elevated temperatures was found to be related to the material softening and necking. Similar trends were observed in the punch force versus punch displacement data for other tested material tempers and thickness.

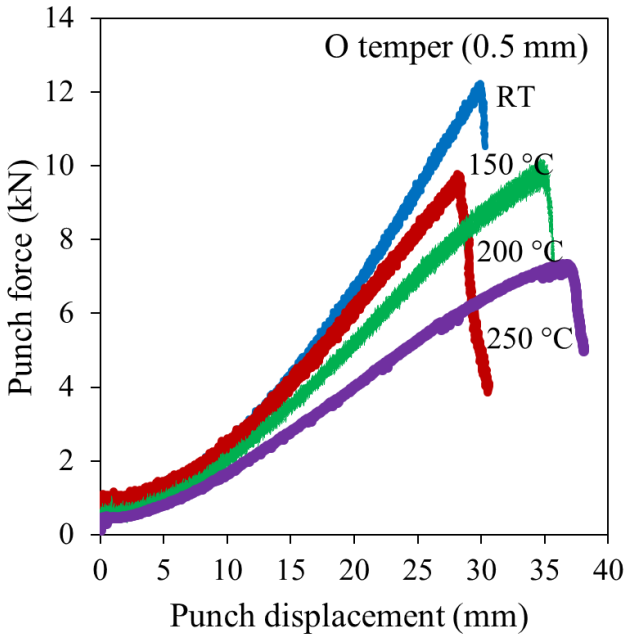

Figure 3.8 Punch force against the punch displacement of a 203.2 mm x 203.2 mm biaxial sample at a forming speed of 0.4 mm/s for different temperatures.

Figure 3.9 shows the average measured dome height plotted against the considered range of forming temperatures. Dome height measurements at the onset of necking were repeated three times for each condition to examine the scatter for three repeat tests which was judged acceptable. As seen from Figure 3.9, larger dome heights were obtained by increasing the forming temperature to 250 °C. In general, the thinner sheet exhibited lower formability compared to the thicker O temper material. The maximum dome height of 38 mm was measured for the 0.5 mm thick O temper sheet at 250 °C. Overall, the improvement in dome height with an increase in temperature from RT to 250 °C was 26-30% for the range of materials and thicknesses considered. An increase in hardness from O-temper to H24-temper resulted in a drop in LDH of 38% at RT and 40% at 250 °C.

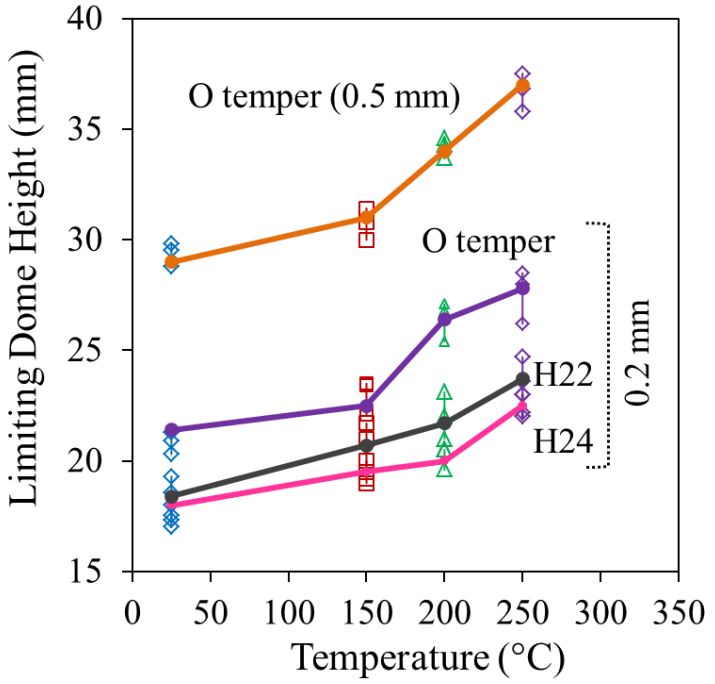

Figure 3.9 Influence of temperature on LDH for 203.2 mm x 203.2 mm biaxial sample at a forming speed of 0.4 mm/s for different temperatures, material thickness and temper.

3.3 Influence of forming speed on limiting dome height

In order to study the effect of forming speed on the dome height of formed specimens, the RT and 250 °C LDH experiments in Section 3.2 performed at 0.4 mm/s were repeated at a speed of 1.6 mm/s. Figure 3.10 shows the average of the measured dome heights at two temperatures, RT and 250 °C, for all four sheet conditions. In general, there was a decrease in dome height to failure of approximately 1.5-3 mm as the punch speed increased from 0.4 to 1.6 mm/s for all temperatures and material conditions. The effect of punch speed was somewhat higher at elevated temperature versus RT conditions.

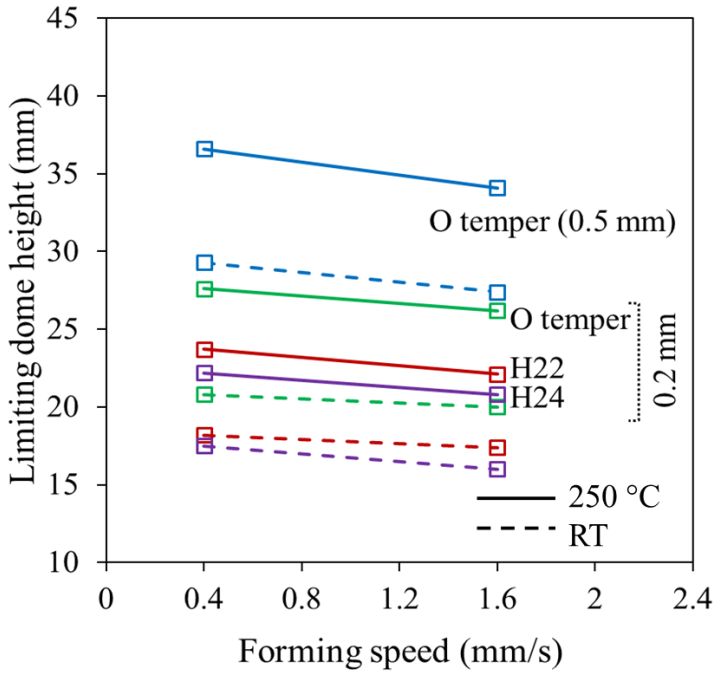

Figure 3.10 Influence of forming speed on the measured dome heights at RT and 250 °C for all four material conditions using a 203.2 mm x 203.2 mm (biaxial sample) at a forming speed of 0.4 and 1.6 mm/s.

3.4 Influence of sample geometry on limiting dome height

Figures 3.11-3.14 shows the LDH values recorded for each specimen geometry as a function of temperature. As described in Section 3.2, four geometries were considered, 25.4 mm (1 in.), 50.8 mm (2 in.) and 76.2 mm (3 in.) dog-bones and 203.2 mm x 203.2 mm square biaxial samples. As observed in Figure 3.11, dome height increased with increasing sample width for the 0.5 mm O-temper samples. The thinner samples exhibited lower dome heights and the higher hardness samples had relatively lower variation in the measured dome height with sample width (Figures 3.12-3.14).

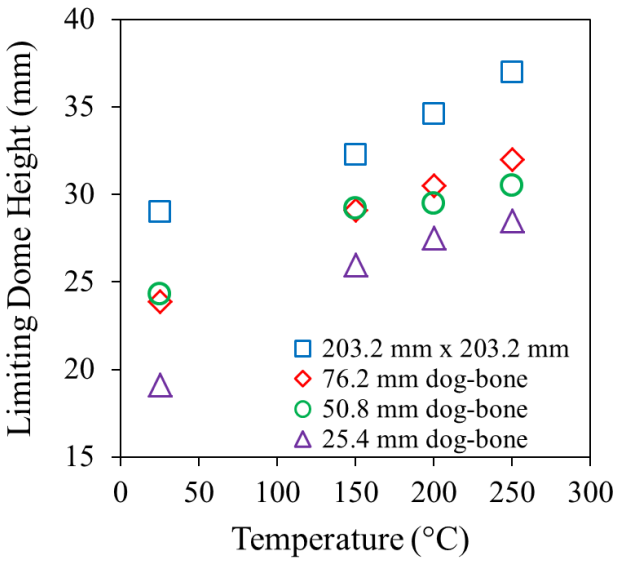

Figure 3.11 Influence of different sample geometries on the measured dome heights at different temperatures for O temper (0.5 mm) at a forming speed of 0.4 mm/s.

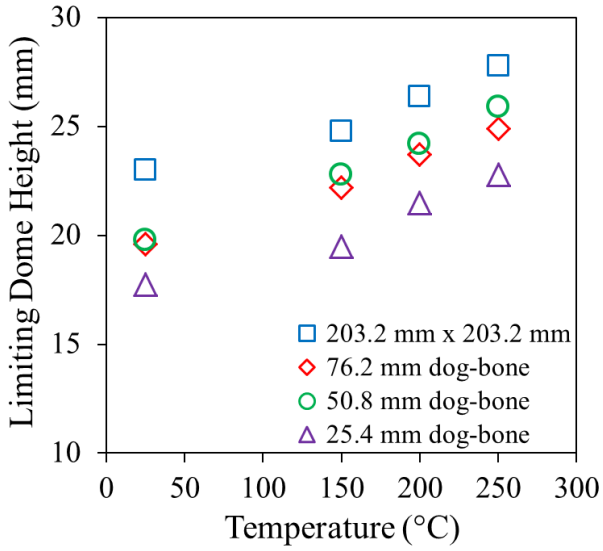

Figure 3.12 Influence of different sample geometries on the measured dome heights at different temperatures for O temper (0.2 mm) at a forming speed of 0.4 mm/s.

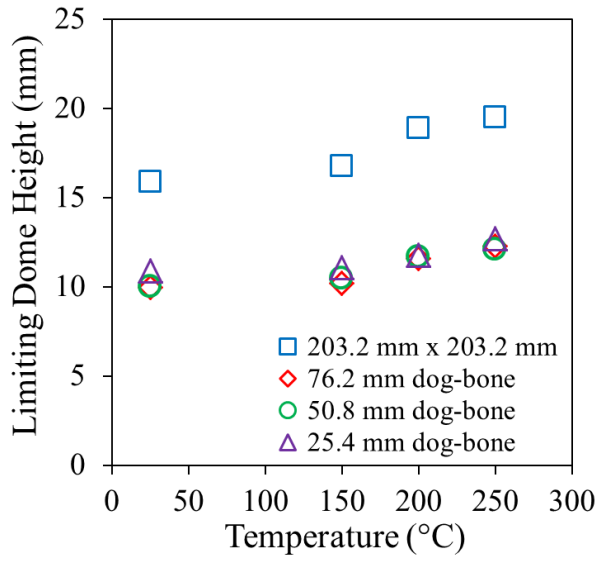

Figure 3.13 Influence of different sample geometries on the measured dome heights at different temperatures for H22 (0.2 mm) at a forming speed of 0.4 mm/s.

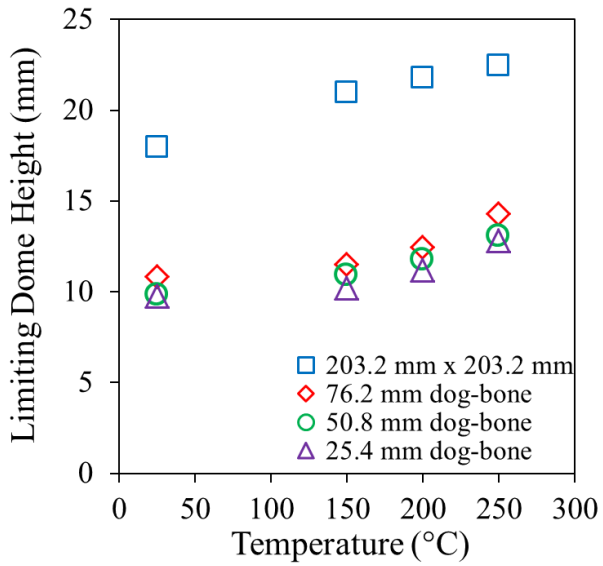

Figure 3.14 Influence of different sample geometries on the measured dome heights at different temperatures for H24 (0.2 mm) at a forming speed of 0.4 mm/s.

3.5 Influence of lubrication condition on dome height

Limiting dome height experiments were conducted without lubricant to investigate the effect of lubrication on the measured dome heights. The experiments considered 0.5 mm O-temper and 0.2 mm H-24 biaxial samples (203.2x203.2mm) and the forming speed was 0.4 mm/s. Figure 3.15 and Figure 3.16 show the dome height values measured for the two sample types as a function of temperature, with or without Teflon sheet lubricant. As can be seen from these figures, the limiting dome height was reduced for the samples without Teflon sheet lubricant for all temperatures tested. Increases in forming temperature were still seen to provide a positive effect on formability even without lubrication. The average dome height of the non-lubricated samples was 21% lower than that of the lubricated samples formed at RT for O temper (0.5 mm). At 250 °C, the dome height of the non-lubricated samples was 25% lower than the height of the lubricated samples.

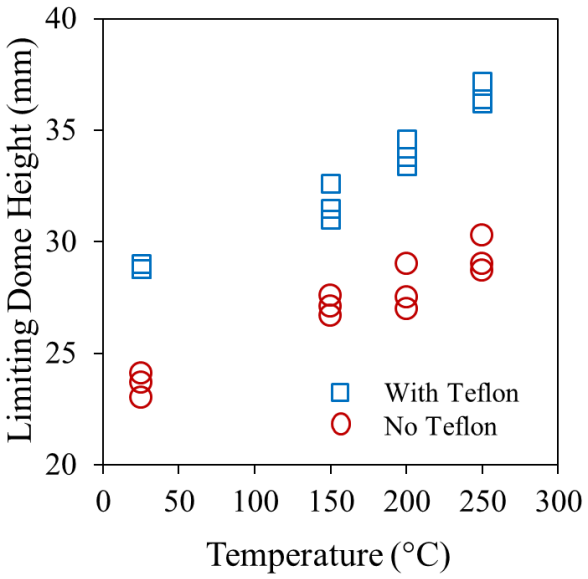

Figure 3.15 Influence of friction on the measured dome heights at different temperatures for O temper (0.5 mm), 203.2 mm x 203.2 mm biaxial sample at a forming speed of 0.4 mm/s.

In the same way for the 0.2 mm H24 samples (Figure 3.16), the average dome height of the non-lubricated samples reduced by nearly 11% when compared to the lubricated samples. At 250 °C, dome height of the non-lubricated samples was only 7% lower as compared to the dome height of lubricated samples.

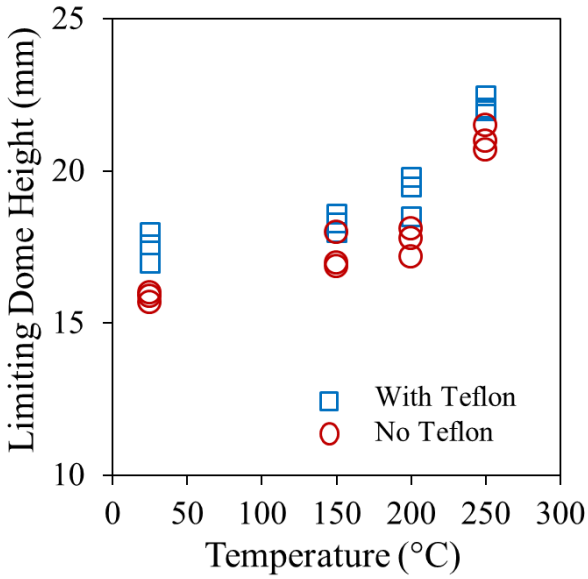

Figure 3.16 Influence of friction on the measured dome heights at different temperatures for H24 (0.2 mm), 203.2 mm x 203.2 mm biaxial sample at a forming speed of 0.4 mm/s.

3.6 Forming limit curves (FLCs)

Major and minor limit strains (e_1 and e_2) were calculated for the 0.5 mm and 0.2 mm AA3003 brazing sheet over a range of temperatures (RT, 150 °C, 200 °C and 250 °C) and forming speeds (0.4 mm/s and 1.6 mm/s). Figures 3.16-3.19 depict the FLCs obtained for a forming speed of 0.4 mm/s for the 0.5 mm O-temper, and 0.2 mm O-temper, H22 and H24 samples, respectively. As observed from the four graphs, formability improved significantly for all cases with an increase in temperature from RT to 250 °C.

The effect of temperature is most pronounced for the O-temper, 0.5 mm FLCs at 200 and 250 °C FLCs (Figure 3.17) which are 94% and 129% higher than the RT levels (based on percentage increase of the plane strain intercept). There is also a "flattening" of the FLCs at the two higher temperatures relative to RT as seen in the smaller difference between the plane strain forming limit (referred to herein as the "FLC-0 strain") versus the biaxial or draw limit strains. The benefit of forming at a temperature of 150 °C is not as strong, with only a 23.5% increase in the plane strain intercept over the RT value. Similar gains in formability with temperature increase are achieved for the thinner (0.2 mm) O-temper sheet. The higher hardness tempers show less relative increase in formability with temperature (Figures 3.18-3.20).

For example, the increase in the plane strain intercept for the 0.2 mm H24 material was 62.5% compared to 92.3% for the O-temper material of the same gauge from RT to 250 °C.

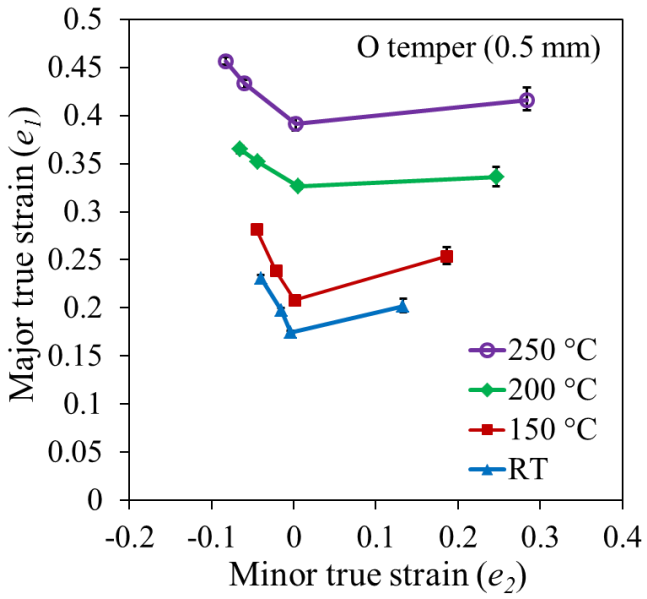

Figure 3.17 FLD for 0.5 mm O-temper AA3003 brazing sheet at 0.4 mm/s for different temperatures.

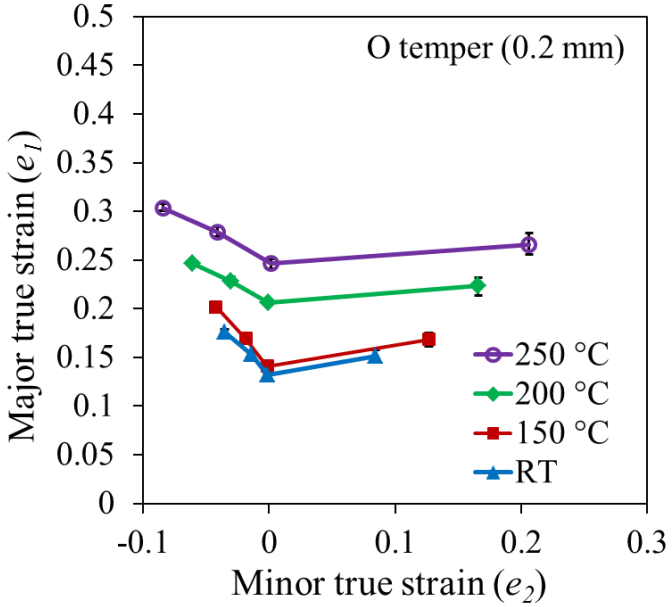

Figure 3.18 FLD for 0.2 mm O-temper AA3003 brazing sheet at 0.4 mm/s for different temperatures.

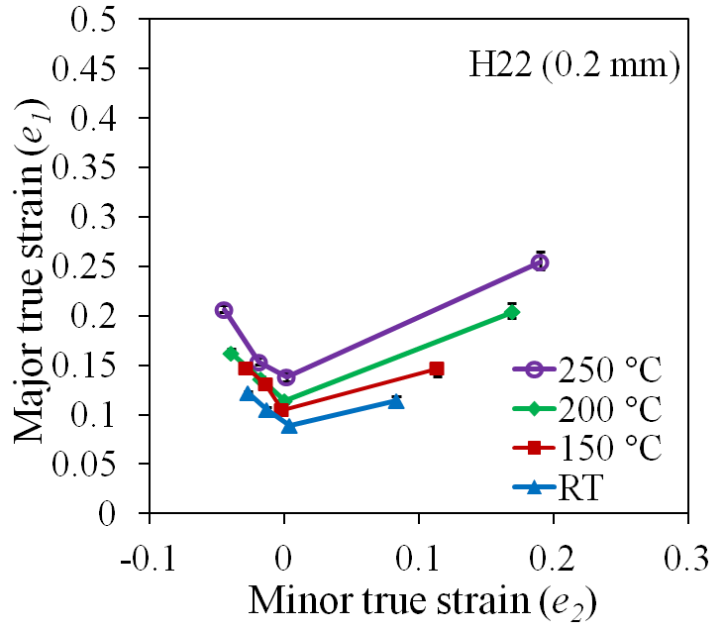

Figure 3.19 FLD for 0.2 mm H22 AA3003 brazing sheet at 0.4 mm/s for different temperatures.

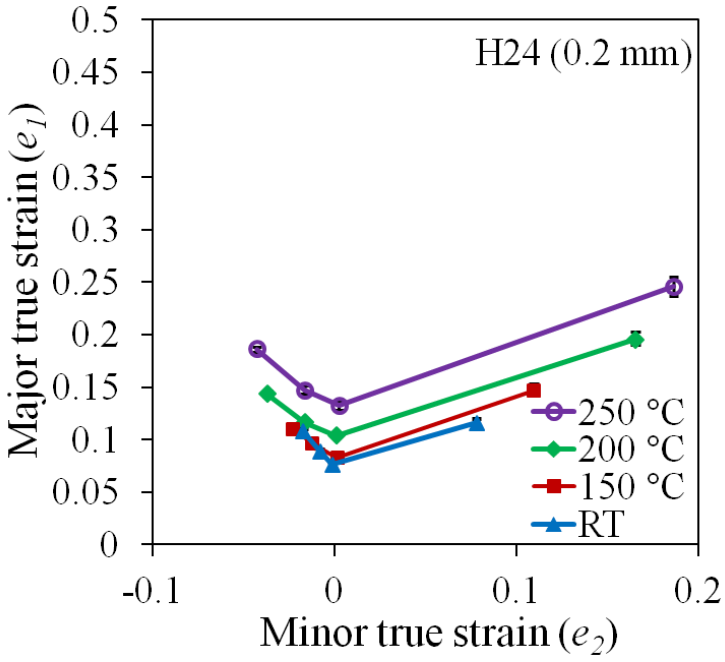

Figure 3.20 FLD for 0.2 mm H24 AA3003 brazing sheet at 0.4 mm/s for different temperatures.

3.6.1 Influence of material thickness and temper on FLC

Figure 3.21 present comparisons of FLC-0 major limit strain for all four sheet materials at different temperatures for forming speeds of 0.4 mm/s. It can be seen that the 0.5 mm O-temper material exhibits higher FLC-0 limit strains at all temperatures when compared to the 0.2 mm O-temper material. The effect of initial hardness in reducing formability is quite pronounced at both RT and at elevated temperature; the 0.2 mm H24 sheet has a 48% lower FLC-0 major strain than the 0.2 mm O-temper material at 250 °C. Interestingly, the FLC-0 strains for the H22 and H24 conditions are similar. The reduction in formability of the H-tempers versus the O-temper condition can largely be attributed to the loss in work hardening due to cold rolling (see Figure 2.4 and Figure 2.5 for stress-strain curves for these sheet materials). The similar formability of the H22 (half hard) and H24 (fully hard) conditions is consistent with the similar hardening rates observed in their stress-strain behavior.

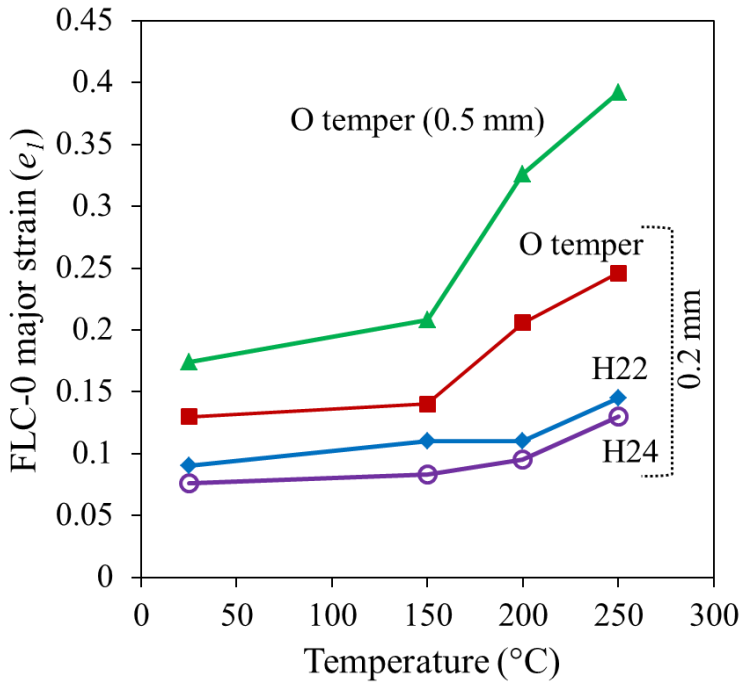

Figure 3.21 Comparison of FLC-0 major limit strain for the four different AA3003 brazing sheet materials at different temperatures, 0.4 mm/s.

3.6.2 Influence of forming speed (punch velocity) on FLC

Figure 3.22 and Figure 3.23 show the effect of punch velocity on the FLCs evaluated for RT and 250 °C. At RT (Figure 3.22), the effect of punch speed is rather small, with only a slight decrease in formability at the higher punch speed of 1.6 mm/s versus 0.4 mm/s. However at 250 °C (Figure 3.23), a significant decrease in the limit strains was observed at the higher forming speed of 1.6 mm/s for all temper conditions. The increased effect of punch speed at higher temperatures is consistent with the coupled nature of strain rate and temperature sensitivity for aluminum alloys. As seen in Figure 2.6, at RT rate sensitivity is low, whereas at elevated temperature strain rate sensitivity increases (Verma, 2016; Kurukuri, 2016); these trends are consistent with the formability results report herein.

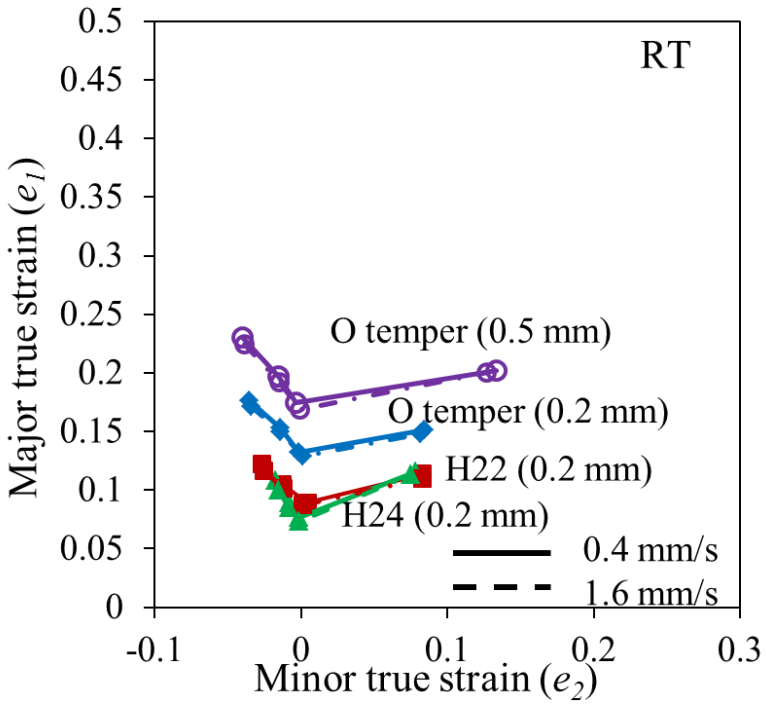

Figure 3.22 Influence of forming speed on the RT FLCs for the four different AA3003 brazing sheet materials.

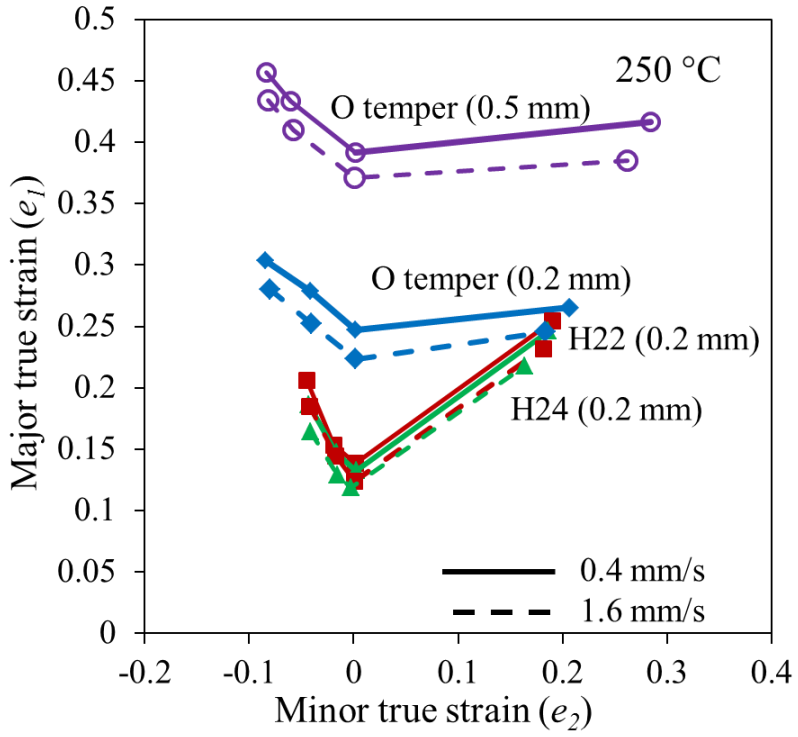

Figure 3.23 Influence of forming speed on the 250 °C FLCs for the four different AA3003 brazing sheet materials.

Chapter 4
FLC prediction for warm forming

4.1 Motivation

Though the forming limit curve has been an effective tool in sheet metal forming industry and research laboratories, the experimental determination of an FLC is comparatively expensive as it involves specialized tooling and experienced personnel. It is also very time consuming to perform formability tests, measure the strains and consistently interpret where actually the plastic instability begins with an adequate level of accuracy. Also the selection of forming limit evaluation method is critically important to minimize the subjective nature of the experimental determination of FLCs, since it is used to establish the quality of large production volumes of stamped parts. It is also well known that many industrial stamping operations are multi-stage, i.e., the sheet material undergoes complex nonlinear strain paths during stamping and the as-received experimental FLC cannot be used to assess the forming severity of parts that were formed. Because, each material point in such a component potentially has a different FLC. It is obviously not possible to develop an FLC experimentally for every nonlinear strain path in a given part. Hence, researchers have been encouraged to create reliable theoretical methods to predict sheet forming limits. The main advantage of predictive methods is that an FLC can instantly be obtained at very little cost using known mechanical properties that can easily be determined by standard tests.

A number of theoretical models have emerged for the calculation of forming limit curves (FLCs). In the current work, the effectiveness of the analytical formulation implemented in software form by Kurukuri (2015) to predict formability under warm forming conditions is considered. This software considers the analytical Marciniak-Kuczynski (1967) approach, along with a non-quadratic yield function, the Barlat YLD-2000 (Barlat et al., 2003) and a rate- and temperature-dependent modified Voce hardening model (Rahmaan et al., 2016; Verma, 2016). The predicted forming limits are validated against the experimental FLC data presented in Chapter 3.

4.2 FLC Prediction Methodology

Analytical prediction of the forming limits was undertaken using the MK analysis software called “vFLC” developed by Kurukuri (2015). This section describes the material modelling aspects of the analysis and formulation of the MK (Marciniak and Kuczynski, 1967) predictions. Much of the model development presented herein is due to Kurukuri (2015), but is presented here for completeness.

4.2.1 Constitutive Model (Hardening Response)

The constitutive data utilized in the M-K simulations are based on the tensile experiments by Verma (2016) and by Kurukuri (2016) on the 0.2 mm and 0.5 mm sheet considered in this work, respectively. This tensile data is presented in Chapter 2 of this thesis (Figures 2.4 and 2.5). From that work, it was observed that the AA3003 brazing sheet exhibits a significant amount of thermal softening and strain rate dependency at elevated temperatures. Hence, a material model which is sensitive to temperature and strain rate is needed to capture the observed material response.

Kurukuri (2016) and Verma (2016) found that the Voce (1948) hardening law captured the flow stresses for all the material conditions relatively well, but noted that this model was independent of strain rate. Therefore the constitutive model developed by (Rahmaan et al., 2016) was adopted in which a strain rate-sensitive term was added to the Voce (1948) strain hardening response, the final version referred as the Modified-Voce model. The constitutive equation for Modified-Voce model is as follows:

Original Voce Model: $$\sigma_v(\varepsilon_P) = \left[\sigma_{sat} + (\sigma_y - \sigma_{sat})e^{\left(-\frac{\varepsilon_p}{\varepsilon_r}\right)}\right] \quad 4.1$$

Modified-Voce Model: $$\bar{\sigma}\left(\varepsilon_p, \dot{\varepsilon}\right) = \sigma_v\left(\varepsilon_p\right) x(\dot{\varepsilon}) \quad 4.2$$

Strain rate Term: $$x(\dot{\varepsilon}) = [A \ln(\dot{\varepsilon}) + (1 + \dot{\varepsilon})^B] \quad 4.3$$

where, σ_{sat} represents the saturation stress, σ_y represents the yield stress, ε_r is the relaxation strain, ε_p is the plastic strain, and parameters A and B describe the rate sensitivity.

Kurukuri (2016) used the uniaxial stress-strain data obtained from tensile experiments on the 0.5 mm O temper sheet and the experiments by Verma (2016) on the 0.2 mm sheet to fit the constitutive parameters of the Modified-Voce model for strain rates of 0.002 and 0.02 s^{-1} at RT, 150 °C, 200 °C, and 250 °C. The resulting values of constitutive parameters (Kurukuri, 2016) for each temper condition/sheet thickness (0.5 mm O temper and 0.2 mm O, H22, and H24 temper) are listed in Table 4.1, 4.2, 4.3 and 4.4, respectively. Figures 4.1-4.4, due to Kurukuri (2016), show a comparison of the predicted (solid lines) and measured (dashed lines) flow curves for the corresponding sheet conditions. A reasonable fit between the flow stress response predicted by the Modified-Voce model and the experimental data can be seen in the plots. The variation between the Modified-Voce model and experimental stress-strain response was greater at 250 °C when compared with temperatures less than 200 °C. The maximum variation of 18% between the true stress values at a strain-rate of 0.02 s^{-1} for the strain-hardened H24 temper was observed at 250 °C. It is also noted that as a consequence of adopting the modified Voce model, the observed negative hardening rate for the harder tempers at high temperature cannot be captured since the modified Voce model imposes a saturation hardening rate of zero. This approach was adopted intentionally since a

negative hardening rate causes numerical difficulties when modelling this material, as noted by Verma (2016).

Table 4.1 The Modified-Voce constitutive model parameters for O temper (0.5 mm)

	RT	150 °C	200 °C	250 °C
σ_{sat} (MPa)	166	147	106	68
σ_y (MPa)	82	84	75	52
ε_r	0.06	0.15	0.12	0.13
A	0.004	0.011	0.06	0.062
B	0.2	3	5	6

Table 4.2 The Modified-Voce constitutive model parameters for O temper (0.2 mm)

	RT	150 °C	200 °C	250 °C
σ_{sat} (MPa)	175	138	115	83
σ_y (MPa)	58	65	65	50
ε_r	0.059	0.075	0.065	0.15
A	0.005	0.015	0.07	0.056
B	0.4	5	4	10

Table 4.3 The Modified-Voce constitutive model parameters for H22 temper (0.2 mm)

	RT	150 °C	200 °C	250 °C
σ_{sat} (MPa)	183	143	116.75	85.75
σ_y (MPa)	150	135	116	85.15
ε_r	0.04	0.043	0.008	0.107
A	0.00001	0.008	0.015	0.002
B	0.624	2.437	4	10.243

Table 4.4 The Modified-Voce constitutive model parameters for H24 temper (0.2 mm)

	RT	150°C	200°C	250°C
σ_{sat} (MPa)	250	173.33	144	104
σ_y (MPa)	209.51	175	143.5	101.6
ε_r	0.076	0.07	0.13	0.25
A	0.003	0.007	0.018	0.006
B	0.01	3.81	5.96	13.785

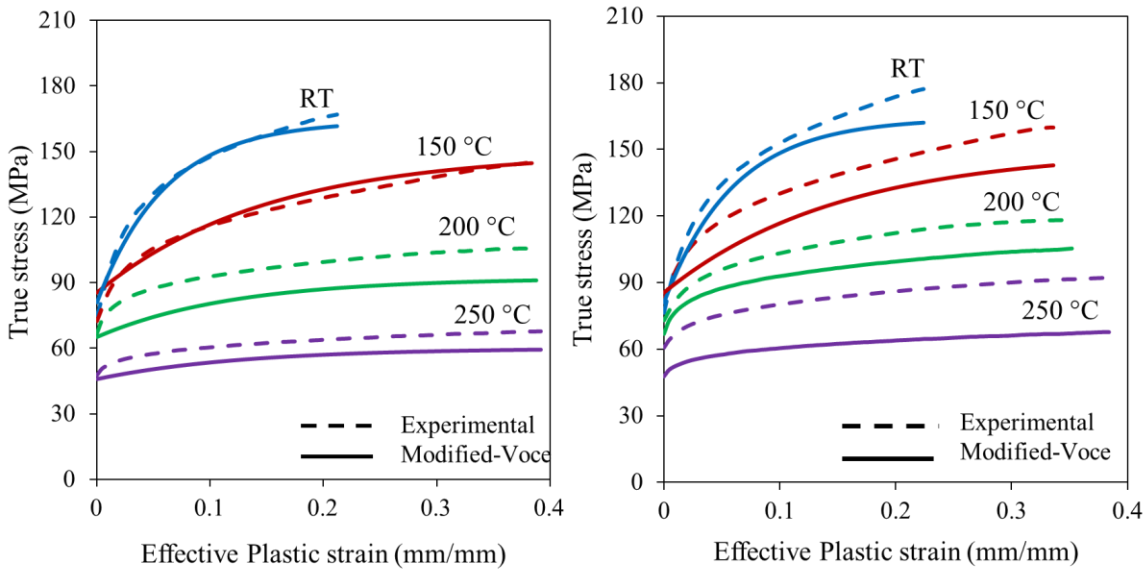

Figure 4.1 Fitted true stress-strain curves for O temper (0.5 mm) at a strain rate of (a) 0.002 s^{-1} and (b) 0.02 s^{-1} for various temperatures.

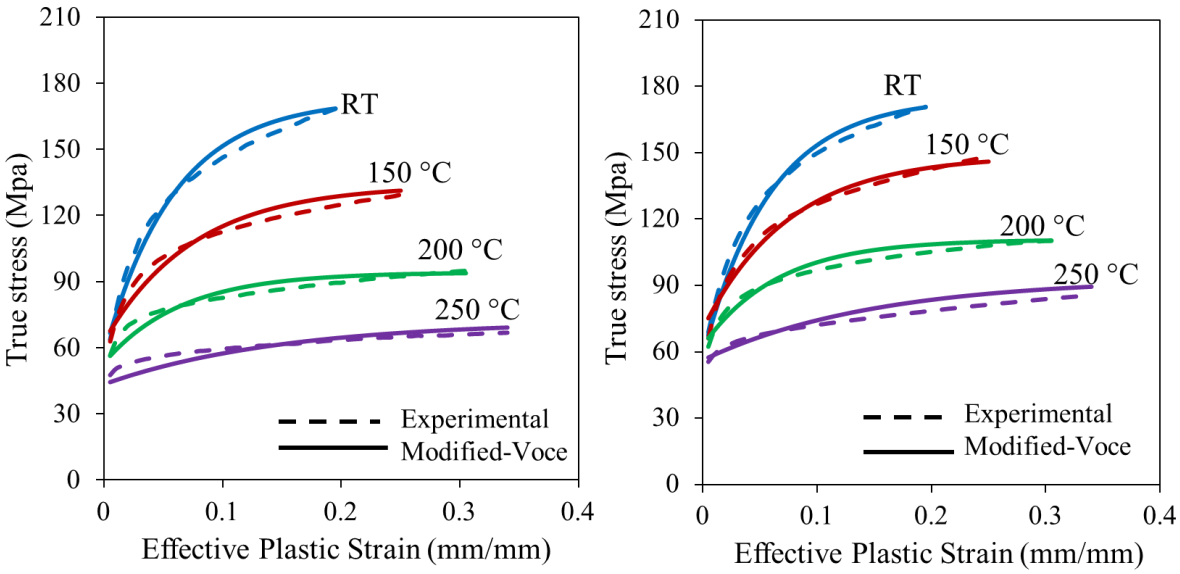

Figure 4.2 Fitted true stress-strain curves for O temper (0.2 mm) at a strain rate of (a) 0.002 s^{-1} and (b) 0.02 s^{-1} for various temperatures.

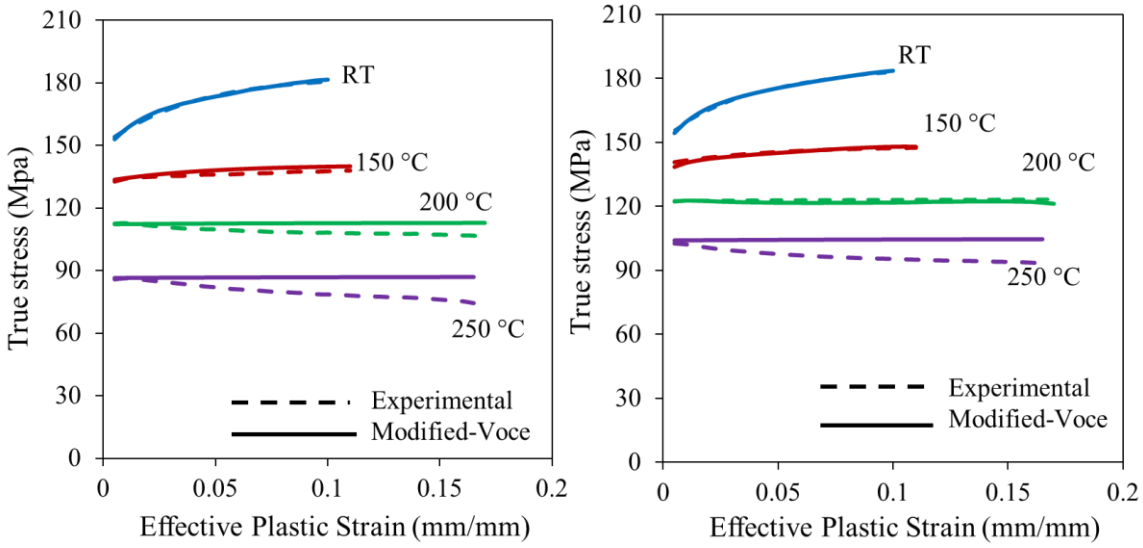

Figure 4.3 Fitted true stress-strain curves for H22 (0.2 mm) at strain rate of (a) 0.002 s^{-1} and (b) 0.02 s^{-1} for various temperatures.

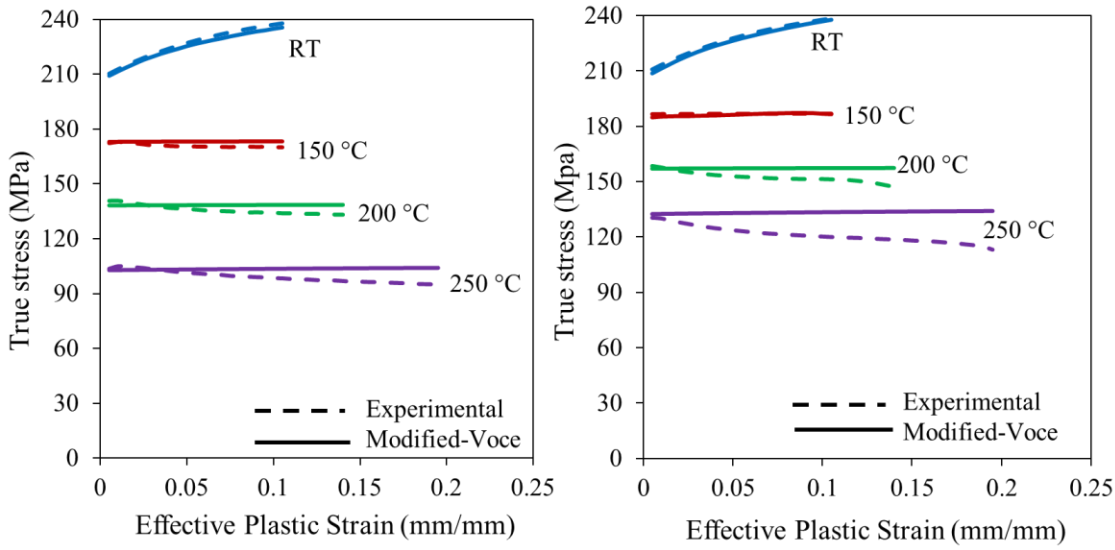

Figure 4.4 Fitted true stress-strain curves for H24 (0.2 mm) at strain rate of (a) 0.002 s^{-1} and (b) 0.02 s^{-1} for various temperatures.

4.2.2 Yield Criterion

Kurukuri (2016) adopted the Barlat Yld2000 yield function (Barlat et al., 2003) to capture the anisotropic yield behavior of the AA3003 brazing sheet. The yield function for plane stress in the x-y (sheet) plane can be expressed in the general form as equation 4.4,

$$\phi = \left|X_1^{'} - X_2^{'}\right|^a + \left|2X_2^{''} + X_1^{''}\right|^a + \left|2X_1^{''} + X_2^{''}\right|^a = 2\bar{\sigma}^a \qquad 4.4$$

where $a = 8$ for FCC material, $\bar{\sigma}$ is the flow stress (given by equations 4.1-4.3) and $X_1^{'}$, $X_2^{'}$, $X_1^{''}$ and $X_2^{''}$ are the principal values of the $\boldsymbol{X}'$ and $\boldsymbol{X}''$, which are the linear transformations of the stress tensor. The linear transformation matrices are defined by eight independent coefficients, α_k (k=1-8), needed to describe the anisotropy of the material (for isotropic case they are equal to 1). These coefficients can analytically be determined based upon the measured flow stress ratios and *r* values in the three sheet orientations (rolling, transverse and diagonal directions) as well as from the biaxial stress and strain ratios. Since the biaxial experimental data was unavailable, biaxial stress and strain ratios are considered as the average of the transverse and diagonal stress and strain ratios, following the approach of Bagheriasl (2012). Figure 4.5 shows Barlat Yld2000 yield loci for the 0.5 mm, O temper AA3003 brazing sheet at different temperatures and a strain rate of 0.002 s^{-1}. The yield surface shows a contraction with

temperature due to thermal softening. The shape of the yield loci was assumed to remain constant with changes in temperature and strain rate.

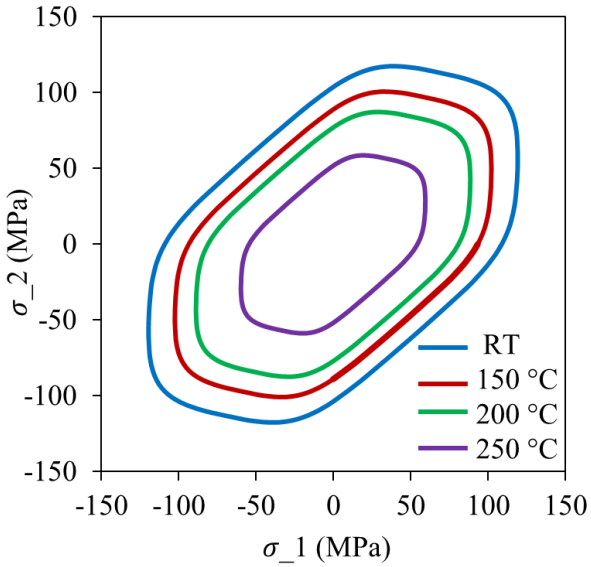

Figure 4.5 Barlat Yld2000 yield loci at different temperatures for 0.5 mm O temper AA3003 brazing sheet (Kurukuri, 2016).

4.2.3 Marciniak and Kuczynski (M-K method)

The FLC predictions developed by Kurukuri (2015) utilize the Marciniak and Kuczynski (1967) analysis to identify the localized necking under biaxial tension. This analysis considers a sheet with an imperfection or initial defect with reduced thickness (Figure 4.6). Parameters referring to the sheet imperfection are given an index *B* and quantities referring to the rest of the sheet are given an index *A*. The thickness of the sheet metal in the imperfection is t_B while the thickness outside the imperfection is t_A. Necking is often observed to run perpendicular to the direction of the major strain (generally for $\varepsilon_2 \geq 0$), thus, the initial imperfection is aligned with the minor strain in the Marciniak-Kuczynski (M-K) analysis.

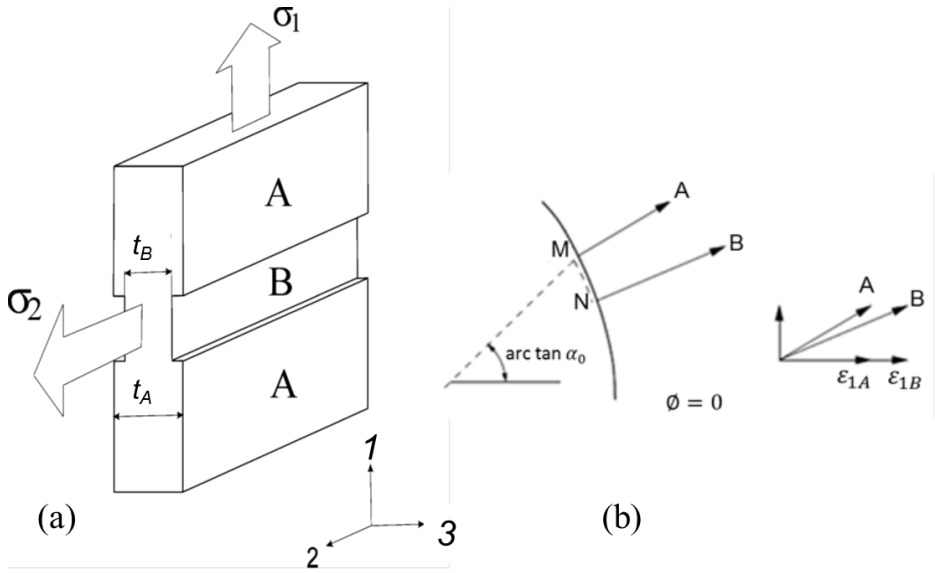

Figure 4.6 Principle of M-K theory (a) plate with defect, and (b) strain increments inside and outside of defect.

Outside the imperfection or groove a proportional deformation path is assumed.

$$\sigma_{2A} = \alpha_0 \sigma_{1A} \qquad \sigma_{3A} = 0$$

$$\varepsilon_{2A} = \beta_0 \varepsilon_{1A} \qquad \varepsilon_{3A} = -(1+\beta_0)\varepsilon_{1A}$$

Here α_0 and β_0 are stress and strain ratios respectively. The compatibility condition between the uniform part A and the imperfection B requires that $d\varepsilon_{2A} = d\varepsilon_{2B}$. The force per unit sheet length in direction 1 (T_1) must be transmitted through the imperfection; hence

$T_1 = \sigma_{1A} t_A = \sigma_{1B} t_B \Rightarrow \sigma_{1B} = \sigma_{1A} / f$,where $f = t_B / t_A$ is the current thickness ratio or coefficient of geometrical non-homogeneity. Provided that $f \approx 1$, the stress ratio α_0 approximately holds for both regions *A* and *B*. As the stress σ_{1B} in the imperfection is greater than σ_{1A} in the uniform part, the material in the imperfection reaches the yield surface first. In Figure 4.6 (b) this is approximately at position *M*. Because of the constraint equation $d\varepsilon_{2A} = d\varepsilon_{2B}$, no yielding takes place, since the uniform region is still fully elastic. The stress state in region *B* will move along the yield locus to position *N*, until also region *A* reaches the yield locus at position *M*. This situation is depicted in Figure 4.6 (b). In that condition σ_{1B}

has increased and σ_{2B} has decreased, hence the stress ratio α has decreased and proportional deformation is not possible in the imperfection (Van den Boogaard et al., 2002).

With the stress state in *A* and *B* at two different positions on the yield locus, the normal to the yield surface is different and because of the constraint $d\varepsilon_{2A} = d\varepsilon_{2B}$, the strain perpendicular to the neck must be larger in the neck than in the uniform part. As a consequence, the thickness decreases more in region *B* ($f < f_0$). The analysis of the deformation can further be developed numerically. The drawing region can be included in the analysis by assuming an inclined imperfection, as predicted by Hill (1952). Strain increments $\Delta\varepsilon_A$ are prescribed on region *A*, respecting the proportionality ratio β_0. For every increment $\Delta\varepsilon_A$, strain increment $\Delta\varepsilon_B$ is calculated iteratively, such that the forces acting in the sheet normal to and tangential to the imperfection in the region *A* and *B* are in equilibrium. The forces acting in the sheet (per unit length) can be calculated from the stresses and the local thickness of sheet as

$$\boldsymbol{T} = \begin{pmatrix} T_{nn} \\ T_{nt} \end{pmatrix} = t \begin{pmatrix} \sigma_{nn} \\ \sigma_{nt} \end{pmatrix}$$

The sheet is considered to have failed if the strain increment in the imperfection is larger than a prescribed multiple of the strain increment in the uniform region. The strain in the uniform region at the time of failure is considered to be the limiting strain for that particular strain ratio β_0. In this work, the analysis will terminate if the strain increment in the imperfection is more than 10 times the strain increment in the uniform region and the corresponding strain in the uniform region is considered as the limiting strain.

4.3 Predictions of FLC

The analytical M-K FLC predictions were performed using the FLC software developed by Kurukuri (2015) which incorporates the Barlat Yld-2000 yield function (Barlat et al., 2003) and rate and the temperature dependent Modified-Voce hardening law constitutive equation (Voce, 1948; Rahmaan, 2015). One of the major concerns of the conventional M-K approach is the somewhat arbitrary determination of initial thickness ratio, since the value of initial thickness ratio (imperfection factor), f_0, chosen in the M-K analysis has a strong influence on the predicted limit strains. For instance, Figure 4.7 depict the predicted forming limit curves using different initial thickness ratios (0.98, 0.985, 0.99 and 0.995) along with the measured experimental limit strains at room temperature for all four materials. It

can clearly be seen that with the imperfection factor of 0.995 yields better room temperature FLC predictions for all materials.

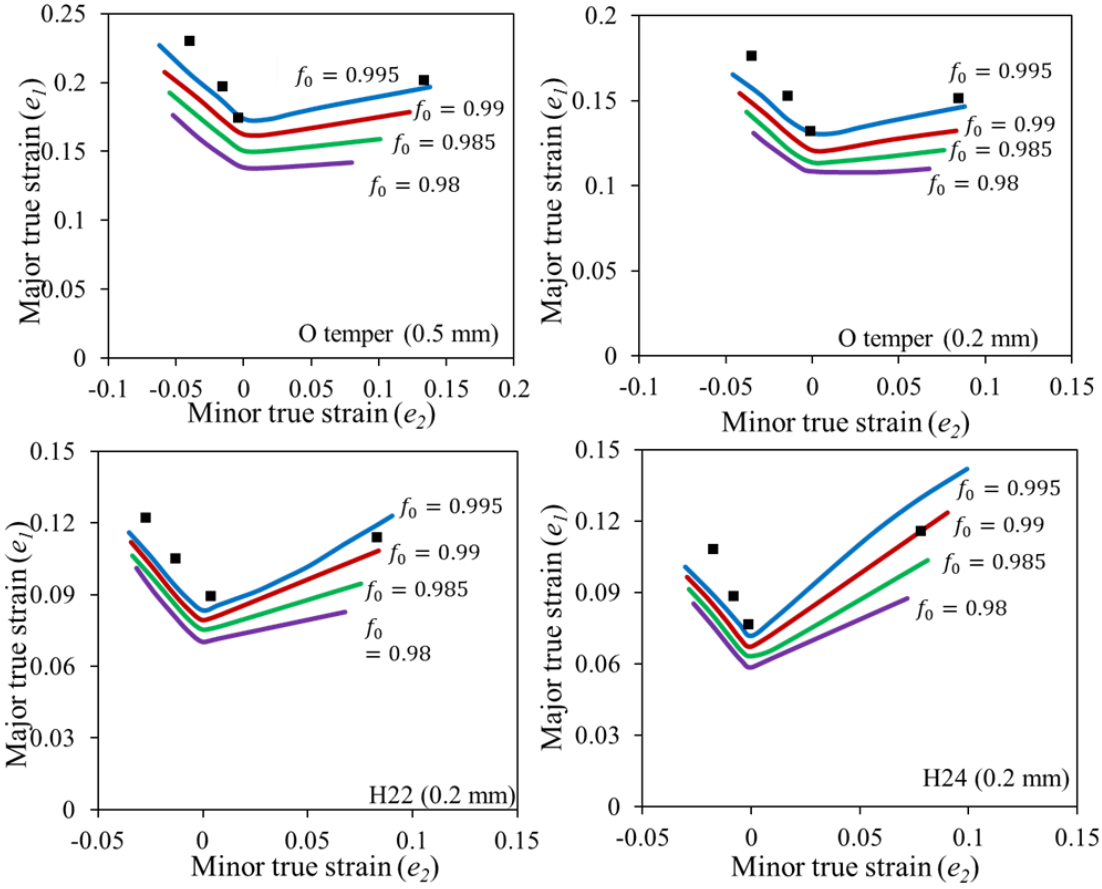

Figure 4.7 Effect of initial thickness ratio in M-K analysis, predicted (solid lines) FLCs using different initial thickness ratios compared with measured limit strains (symbols) at RT.

The FLCs predicted at a temperature of 250 °C with different initial thickness ratios are shown in Figure 4.8, along with the measured limit strains. Comparison between the predicted and measured limit strains indicates that an initial thickness ratio of 0.99 results in a good approximation for H22 and H24 materials, whereas an initial thickness ratio of 0.98 found to be a good choice for O-tempered materials. Hence from this parametric study, it is decided to select an initial thickness ratio, $f_0 = 0.995$, for room temperature predictions for all materials, whereas an initial thickness ratio of 0.99 was adopted for temperatures of 150 °C and above for the H22 and H24 materials. On the other hand, an initial thickness

ratio of *0.98* was adopted for the elevated temperature FLC predictions for O temper materials. Thus, no single value of initial thickness imperfection could be found that was suitable for all material conditions.

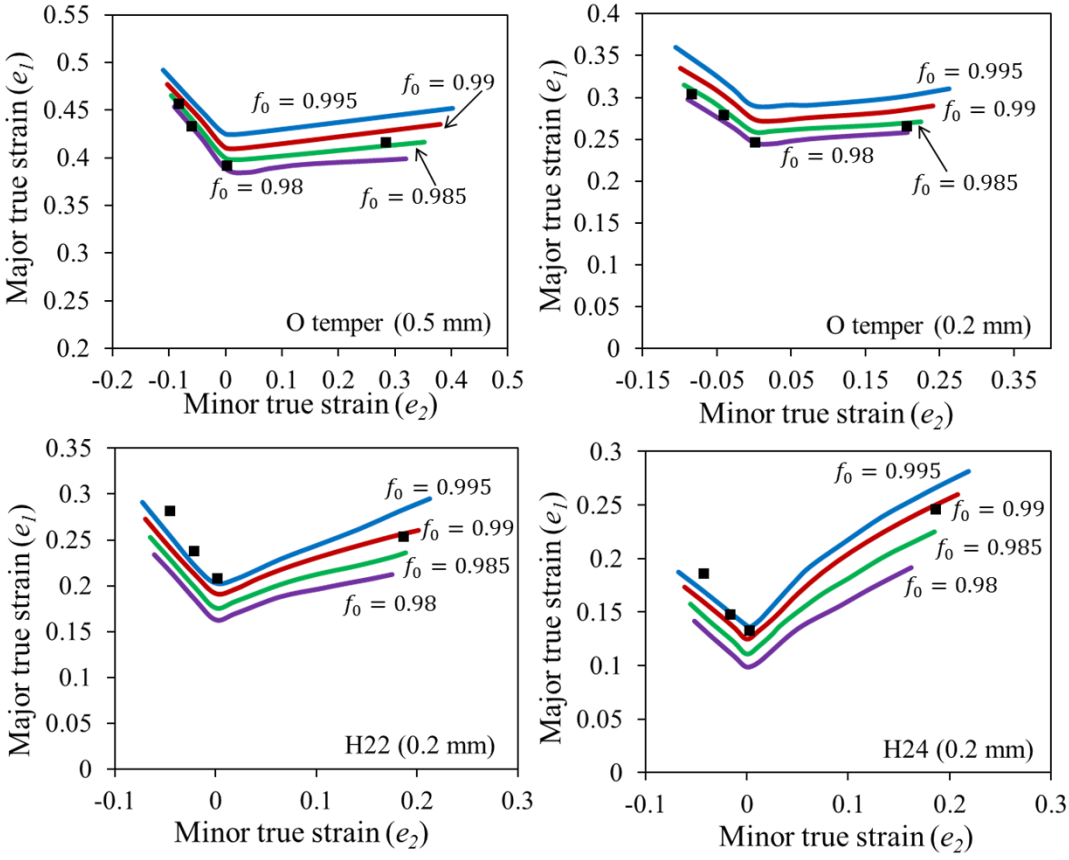

Figure 4.8 Effect of initial thickness ratio in M-K analysis; predicted (solid lines) FLCs using different initial thickness ratios compared with measured limit strains (symbols) at 250 °C.

Figures 4.9-4.12 present comparisons between the predicted FLCs (using M-K analysis with the temperature dependent Modified-Voce hardening model and the Barlat Yld2000 yield function) with the experimental FLCs at RT, 150 °C, 200 °C and 250 °C and forming speed of 0.4 mm/s.

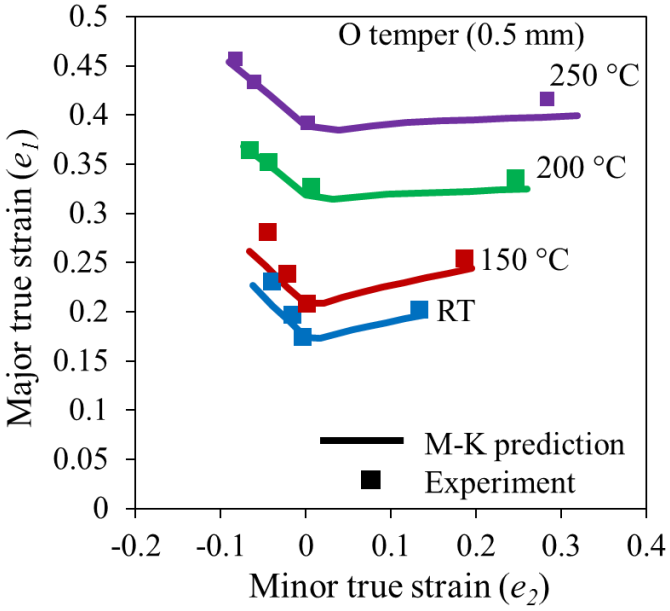

Figure 4.9 Predicted (solid lines) FLCs using M-K analysis compared with experimentally measured limit strains (symbols) for different temperatures at 0.4 mm/s.

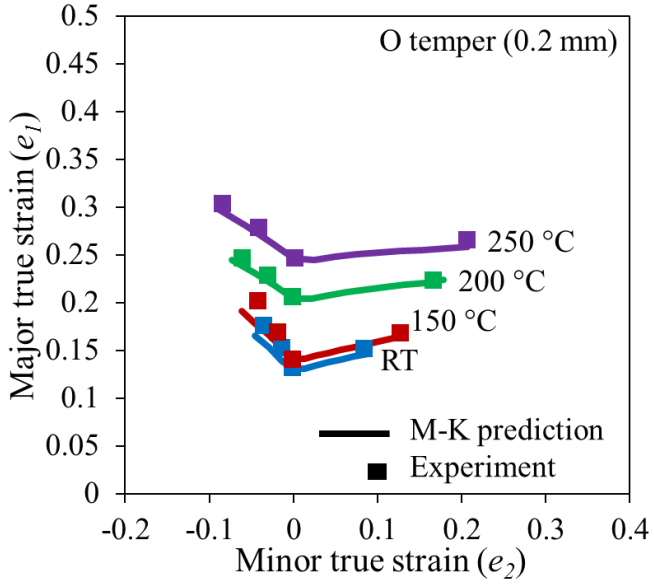

Figure 4.10 Predicted (solid lines) FLCs using M-K analysis compared with experimentally measured limit strains (symbols) for different temperatures at 0.4 mm/s.

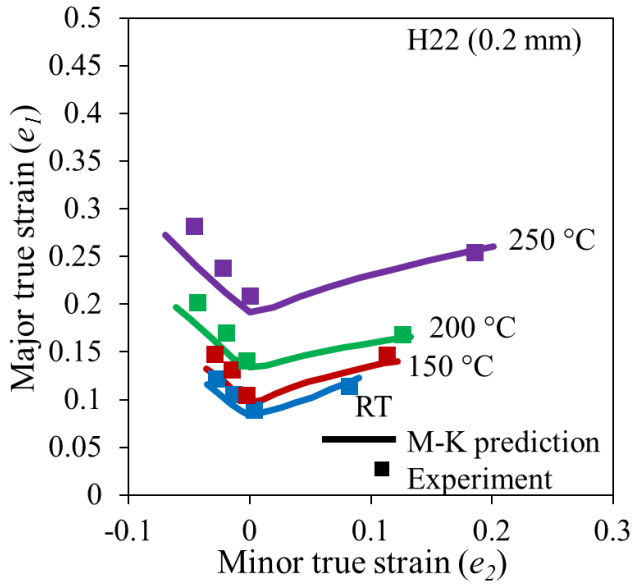

Figure 4.11 Predicted (solid lines) FLCs using M-K analysis compared with experimentally measured limit strains (symbols) for different temperatures at 0.4 mm/s.

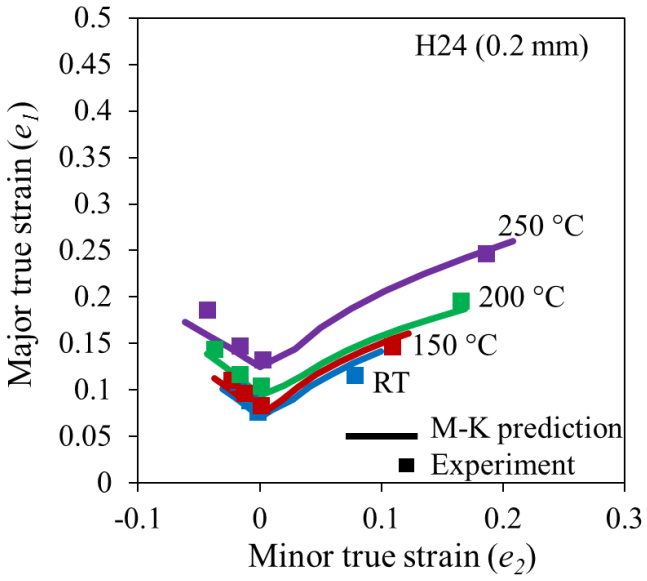

Figure 4.12 Predicted (solid lines) FLCs using M-K analysis compared with experimentally measured limit strains (symbols) for different temperatures at 0.4 mm/s.

From Figures 4.9-4.12, it is evident that the M-K model is able to capture the temperature dependent formability behavior for the considered brazing sheets. It is observed that the limit strains increased significantly when the forming temperature increased from RT to 250 °C. The model is also able to capture the flattening of the FLCs at elevated temperature observed for the softer temper conditions.

Figure 4.13 depicts the effect of punch velocity on the predicted forming limit curves compared with the corresponding measured limit strains for the 0.5 mm thick O-temper sheet at RT and 250 °C. At RT, the effect of punch speed on the predicted FLCs is negligible, in agreement with the experiments. However, at 250 °C, a decrease in the measured limit strains is observed at the higher forming speed of 1.6 mm/s, but only a small change is seen in the predicted FLC. A similarly low predicted rate effect was observed for the other material conditions. Future studies should perhaps consider alternate material models to ascertain whether this lack of rate effect in the model can be corrected.

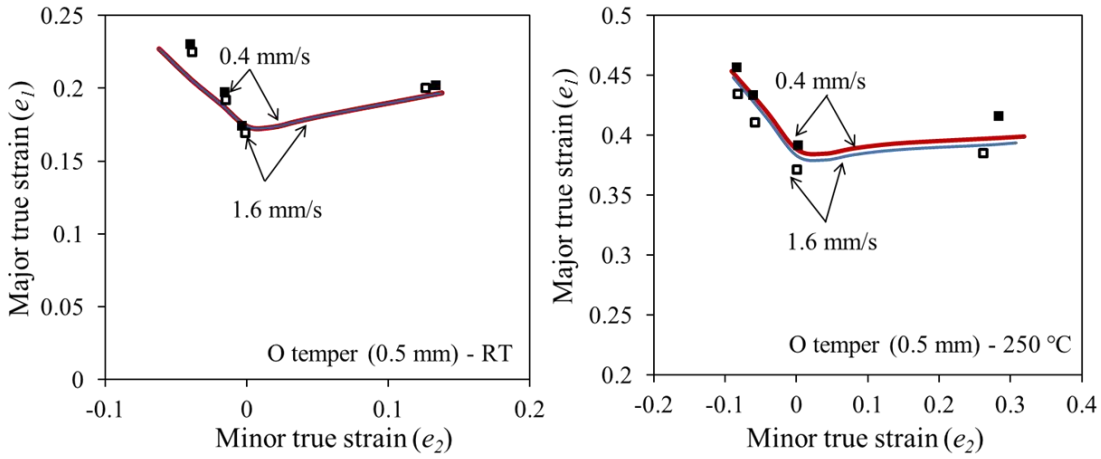

Figure 4.13 Influence of forming speed on the predicted FLCs (solid lines) compared with the experimentally measured limit strains (symbols) for the 0.5 mm thick, O-tempered AA3003 brazing sheet material at RT and 250 °C.

From the results presented in this chapter, the predicted forming limit strains are very sensitive to the value chosen for the initial geometrical imperfection factor used in the M-K method. In order to overcome this shortfall of the M-K method, the thickness imperfection can perhaps be associated with a measurable source of heterogeneity such as the change in surface roughness of the sheet material with forming temperature or material inhomogeneities, for example changing microstructure due to forming conditions.

However, such approaches are left for future work. Nonetheless, the M-K models are able to capture the observed increase in FLC with temperature rather well.

Chapter 5
Conclusions

Limiting dome height experiments were conducted on AA3003 brazing sheet for three different temper conditions (O, H22 and H24) and two thicknesses (0.2 and 0.5 mm) at temperatures in the range RT - 250 °C and forming speeds of either 0.4 mm/s or 1.6 mm/s. The effect of temperature, forming speed, specimen geometry and lubricant on the limiting dome heights was examined. Forming limit curves (FLCs) were developed for each condition and the influence of material temper, forming speed and temperature were studied. The main conclusions resulting from the present investigation are as follows:

1. Five types of dry film lubricants, namely OKS 536, Fuchs Lubrodal F 400, Diacut NCL, MXC 2187 and Teflon sheets were studied in the present work. The OKS and Lubrodal F 400 resulted in a lower dome height than the Teflon. The MXC and Diacut had higher dome heights, but were too smoky at 250 °C. Hence, Teflon was selected as the lubricant over the range of temperatures tested.

2. Limiting dome height (LDH) experiments using 0.5 mm O temper AA3003 brazing sheet revealed that increasing the temperature from RT to 250 °C increases the biaxial dome height from 29.3 mm to 38 mm, a 27.6 % increase.. The corresponding increases for the 0.2 mm material in the O, H22 and H24 tempers were 30%, 29% and 26%, respectively.

3. A reduction in thickness resulted in a decrease in the measured FLCs. For example, the plane strain limit strain or FLC-0 strain of the O temper materials decreased by 24% at RT when the thickness decreased from 0.5 mm to 0.2 mm and a corresponding decrease of 35% was measured at 250 °C.

4. An increase in hardness also caused a reduction in formability. The RT FLC-0 strains for the 0.2 mm H22 and H24 materials were 31% and 39% lower than the corresponding value for the 0.2 mm O temper sheet. The corresponding reductions at 250 °C were 39% and 48%.

5. The effect of an increase in forming speed from 0.4 mm/s to 1.6 mm/s on the RT FLC was small for all material conditions considered. A larger drop in formability, in the range 6-9% was observed at 250 °C for this increase in forming speed.

6. The Marciniak-Kuczynski (M-K) analysis was able to capture the temperature dependent formability behavior, however, the influence of forming speed on the FLCs was not as strong as was observed in the experiments. It was not possible to find a single value of initial imperfection ratio that could be used for all of the material conditions considered. The calibrated M-K predictions, for a given thickness and temper, did capture the increase in the FLC with temperature rather well.

Chapter 6
Future Work

The following future work is proposed based upon the results of the current research:

1. FLCs at higher forming speeds (representative of stamping operations) should be determined to investigate the influence of strain-rate on the formability of AA3003 brazing sheet at higher temperatures. Such efforts would require fast material handling systems and high speed cameras to be used with the DIC system.
2. Further investigation of time-dependent methods for the detection of onset of necking (or limit strain determination) should be pursued for materials with thickness ≤ 0.5 mm.
3. An investigation of appropriate warm forming lubricants that display desirable lubricity without build up on forming dies is necessary. A warm friction testing capability should be developed, likely based upon the current twist compression friction testing apparatus, to better characterize the warm performance of lubricants.
4. There is a need to implement the failure criteria at elevated temperatures, which involves calculation of stress-based FLDs from the current measured strain-based FLDs. Stress-based FLCs may prove useful to capture the effects of changes in strain path.
5. An appropriate material model should be developed that better accounts for strain rate and temperature sensitivity and the negative work hardening behavior observed for the H22 and H24 sheet at elevated temperatures.
6. The predicted forming limit strains are very sensitive to the imperfection value used in the M-K method. A more rationale method for determining the thickness imperfection should be developed, for example, relating the imperfection to measurable sources of heterogeneity such as surface roughness.

References

Abedrabbo, N., Pourboghrat, F., Carsley, J. Forming of AA5182-O and AA5754-O at elevated temperatures using coupled thermo-mechanical finite element models. *International Journal of Plasticity* **2007**, 23, 841 – 875.

Abedrabbo, N., Pourboghrat, F., Carsley, J. Forming of aluminum alloys at elevated temperatures - part 1: Material characterization. *International Journal of Plasticity* **2006**, 22, 314 - 341.

Ayres, R. A., Brewer, E. G., Holland, S. W. *Transactions of the Society of Automotive Engineers* **1979**, 88, 2630-2634.

Bagheriasl, R., Ghavam, K., Worswick, M.J. Effect of temperature and strain rate on warm formability of aluminum alloy sheet, *Proceedings of the 8th International Conference: NUMISHEET*, Seoul, Korea, **2011**.

Bagheriasl, R. Formability of Aluminum Alloy Sheet at Elevated Temperature *PhD Thesis, University of Waterloo* **2012**.

Bagheriasl, R., Ghavam, K., Worswick, M.J. Formability improvement with independent die and punch temperature control, *International Journal of Material Forming*, **2014**, 7, 139-154.

Barlat, F., Brem, J.C., Yoon, W., Chung, K., Dick, R.E., Lege, D.J., Poourboghrat, F. Plane stress function for aluminum alloy sheets - part 1: theory, *International Journal of Plasticity*, **2003**, 19, 1297-1319.

Bolt, P. J., Lamboo, N. A. P. M., Rozier, P. J. C. M. Feasibility of warm drawing of aluminum products Journal of Materials Processing Technology **2001**, 115, 118-121.

Boba, M., Worswick, M.J., Mishra, R.K., Carter, J.T. Formability of AZ31B and ZEK100 Magnesium Alloy Sheets at Elevated Temperatures, *Magnesium Conference 2012*, Vancouver, **2012**.

Boba, M. Warm forming behavior of ZEK100 and AZ31B Magnesium Alloy Sheet *MASc Thesis, University of Waterloo* **2014**.

Bradley, J.R. Bulge Testing of Superplastic AA5083 Aluminum Sheet. *Advances in Superplasticity and Superplastic Forming*, edited by E.M. Taleff et al. (Warrendale, PA) TMS **2004**, 109–118.

Cobden, R. Aluminum: Physical properties, characteristics and alloys, *European Aluminum Association*, **1994**.

Chung, S. Y., and Swift, H. W. Cup Drawing from a Flat Blank, *Proceedings of the Institution of Mechanical Engineers* **1951**, 165, 199.

Cole, G. S., Sherman, A. M. Lightweight materials for automotive applications, *Materials Characterization* **1995**, 35, 3-9.

Dieter, G.E., Kuhn, H.A., Semiatin, S.L. Handbook of workability and process design.ASM International, Metals Park, OH, **2003**.

Dinda, S., James, K. F., Keeler, S. P., Stine, P. A. How to Use Circle Grid Analysis for Die Tryout, *American Society of Metals*, Metals Park, OH **1981**.

Eary, D.F. Techniques of press working sheet metals, Prentice Hall, London, **1974**.

Erichsen, A. M. A new test for thin sheets, *Stahl und Eisen*, **1914**, 34, 879-882 (in German).

Ghavam, K., Bagheriasl, R., Worswick, M. J. Analysis of Non-isothermal Deep Drawing of Aluminum Alloy Sheet With Induced Anisotropy and Rate Sensitivity at Elevated Temperatures, *Journal of Manufacturing Science and Engineering*, **2014**, 136, 011006.

Ghosh, A. K. The Effect of Lateral Drawing- In On Stretch Formability, *Metals Engineering Quarterly* **1975**, 15, 53-64.

Goodwin, G. M. Application of strain analysis to sheet metal forming problems in the press shop, *Transactions of Society of Automotive Engineers* **1968**, 77, 380–387.

Hadianfard, M.J., Smerd, R., Winkler, S., Worswick, M.J. Effect of strain rate on mechanical properties and failure mechanism of structural Al-Mg alloys, *Materials Science and Engineering A*, **2008**, 492, 283-292.

Hasan, R. Z., Kinsey, B. L., Tuskrov, I. Effect of element types on failure prediction using a stress-based forming limit curve, *Journal of Manufacturing Science and Engineering* **2011**, 133, 1002-1010.

Harvey, D. N. Optimizing patterns and computational algorithms for automatic, optical strain measurement in sheet metal, efficiency in sheet metal forming, *Proceedings of the 13th Biennial Congress, Melbourne, Australia, International Deep Drawing Research Group* **1984**, 403-414.

Hecker, S. S. A cup test for assessing stretchability, *Metals Engineering Quarterly* **1974**, 14, 30-36.

Hecker, S.S. Simple technique for determining forming limit curves, *Sheet Metal Industries*, **1975**, 52, 671-676.

Hecker, S. S., Gosh, A. K., Gegel, H. L. Formability: Analysis, Modeling, and Experimentation, *American Institute of Mining, Metallurgical, and Petroleum Engineers, New York* **1978**, 150-182.

Hill, R. On discontinuous plastic states, with special reference to localized necking in thin sheets, *Journal of the Mechanics and Physics of Solids*, **1952**, 1, 19-30.

Hora, P., Tong, L. Prediction methods for ductile sheet metal failure using FE simulation, *In: Barata da Rocha A (ed) Proceedings of the IDDRG Congress, Porto*, **1994**, 363-375.

ISO/DIS 12004-2, Metallic materials - Sheet and strip - Determination of forming limit curves - Part 2: Determination of forming limit curves in laboratory, *ISO copyright office*, **2008**.

Kang, J., Wilkinson, D.S., Jain, M., Embury, J.D., Beaudoin, A.J., Kim, S., Mishira, R., Sachdev, A.K. On the sequence of inhomogeneous deformation processes occurring during tensile deformation of strip cast AA5754, *Acta Materialia*, **2006**, 54, 209-218.

Kabirian, F., Khan, A. S., Pandey, A. Negative to positive strain rate sensitivity in 5xxx series aluminum alloys: Experiment and constitutive modeling, *International Journal of Plasticity* **2014**, 55, 232-246.

Kapij, M. I., Lee, D. Tribological factors in the stamping of coated and uncoated steel sheets, *16th Biennial Congress of the International Deep Drawing Research Group, Borlänge* **1990**.

Kaya, S., Spampinato, G., Altan, T. An Experimental Study on Nonisothermal Deep Drawing Process Using Aluminum and Magnesium Alloys, *Journal of Manufacturing Science and Engineering* **2008**, 130, 1001-1011.

Keeler, S. P., Backofen, W. A. Plastic instability and fracture in sheets stretched over rigid punches, *Transactions of the American Society of Metals* **1963**, 56, 25-48.

Kim, H. S., Koc, M., Ni, J., Ghosh, A. Finite element modeling and analysis of warm forming of aluminum alloys-validation through comparisons with experiments and determination of a failure criterion, *Journal of Manufacturing Science and Engineering* **2006**, 128, 613-621.

King, J.E., You, C.P., Knott, J.F. Serrated yielding and the localized shear failure mode in aluminum alloys, *Acta Metallurgica*, **1981**, 29, 1553-1566.

Kleemola, H.J., Kumpulainen, J.O. Factors influencing the Forming Limit Diagram: Part I -- The experimental determination of the forming limits of sheet steel. *Journal of Mechanical Working Technology* **1980**, 3, 289-302.

Kurukuri, S., Van den Boogaard, A.H., Miroux, A., Holmedal, B. Warm forming simulation of Al-Mg sheet. *Journal of Materials Processing Technology* **2009**, 209, 5636 - 5645.

Kurukuri, S. Simulation of thermally assisted forming of aluminum sheet *PhD Thesis, University of Twente,* **2010**.

Kurukuri, S., Van den Boogaard, A.H., Ghosh, M., Miroux, A. Thermo-mechanical forming of Al-Mg-Si alloys: Modeling and experiments, *AIP Conference Proceedings*, **2010**, 1252, 810-815.

Kurukuri, S., Miroux, A., Wisselink, H.H., Van den Boogaard, A.H. Simulation of stretch forming with intermediate heat treatments of aircraft skins - a physically based modeling approach. *International Journal of Material Forming* **2011**, 4(2), 129-140.

Kurukuri, S. vFLC - A user friendly software for calculating forming limit curves, **2015.**

Kurukuri, S., Jain, E., Worswick, M.J., Winkler, S. Comparison of warm formability assessment methods, *Proceedings of the Forming Technology Forum* , Zurich, **2015**.

Kurukuri, S. *Private communication*, **2016**.

Lademo, O. G., Engler, O., Aegerter, J., Berstad, T., Benallal, A., Hopperstad, O. S. Starin-Rate Sensitivity of Aluminum Alloys AA1200 and AA3103, *Journal of Engineering Materials and Technology* **2010**, 132, 1007-1015.

Li, D., Ghosh, A. Tensile deformation behavior of aluminum alloys at warm forming temperatures, *Materials Science and Engineering A* **2003**, 352, 279-286.

Li, D., Ghosh, A. Biaxial warm forming behavior of aluminum sheet alloys, *Journal of Materials Processing Technology* **2004**, 145, 281-293.

Marciniak, Z. Stability of Plastic shells under tension with kinematic boundary condition, *Archiwum Mechaniki Stosorwanej*, **1965**, 17, 577-592.

Marciniak, Z., Kuczynski, K. Limit strains in processing of stretch forming sheet metal, *International Journal of Mechanical Sciences*, **1967**, 9, 609-620.

Martínez-Donaire, A.J., García-Lomas, F.J., Vallellano, C. New approaches to detect the onset of localized necking in sheets under through-thickness strain gradients. *Materials & Design* **2014**, 57,135-145.

McKinley, J., Abedrabbo, N., Worswick, M.J., Kozdras, M. Effect of independent die and punch temperature control on the formability of 3003 aluminum alloy in warm deep drawing. *Proceedings of the 7th International Conference Numisheet, Interlaken, Switzerland*, **2008**.

McKinley, J. Warm Forming of Aluminum brazing sheet *MASc Thesis*, *University of Waterloo* **2010**.

Mechanical Engineer's Handbook, 2nd edition, **2001** Academic press, USA.

Merklein, M., Kuppert, A., Geiger, M. Time dependent determination of forming limit diagrams, CIRP Annual Manufacturing Technology **2010**, 59, 295-298.

Merklein, M., Kuppert, A., Affronti, E. An improvement of the time dependent method based on the coefficient of correlation for the determination of the forming limit curve, *Advanced Materials Research*, **2014**, 1018, 215-222.

Miller, W. S., Zhuang, L., Bottema, J., Wittebrood, A. J., Smet, P. De, Haszler, A., Vieregge, A. Recent development in aluminium alloys for the automotive industry, *Materials Science and Engineering A* **2000**, 280, 37-49.

Naka, T., Yoshida, F. Deep drawability of type 5083 aluminum–magnesium alloy sheet under various conditions of temperature and forming speed, *Journal of Materials Processing Technology* **1999**, 89-90, 19-23.

Nakazima, K., Kikuma, T., Hasuka, K. Technical report 264, *Yawata Iron & Steel Co.* Sep **1968**, P.141.

Narashimhan, K., Nandedkar, V. M. Formability testing of Sheet metals, *Transactions of the Indian Institute of Metals* **1996**, 49, 659-676.

Olsen, T.Y. Machines for ductility testing, *Proceedings of the American Society for Testing and Materials*, **1920**, 20, 398-403.

Palumbo, G., Tricarico, L. Numerical and experimental investigations on the warm deep drawing process of circular aluminum alloy specimens, *Journal of Materials Processing Technology* **2007**, 184, 115-123.

Picu, R. C., Vincze, G., Ozturk, F., Gracio, J. J., Barlat, F., Maniatty, A. M. Strain rate sensitivity of the commercial aluminum alloy AA5182-O, *Materials Science and Engineering A-Structures* **2005**, 390, 334-343.

Rahmaan, M.T. Low to High Strain Rate Characterization of DP600, TRIP780, AA5182-O *MASc thesis, University of Waterloo* **2015**.

Rahmaan, T., Bardelcik, A., Imbert, J., Butcher, C., Worswick, M. Effect of strain rate on flow stress and anisotropy of DP600, TRIP780, AA5182-O sheet metal alloys, *International Journal of Impact Engineering*, **2016**, 88, 72-90.

Recommended Referee Practice for the Limiting Dome Height (LDH) Test. *North American Deep Drawing Research Group*, **1987**.

Shehata, F., Painter, M. J., Pearce, R. Warm forming of aluminum/magnesium alloy sheet, *Journal of Mechanical Working Technology* **1978**, 2, 279-291.

Smith, B. W., Li, M., Tong, W. Error assessment for strain mapping by Digital Image Correlation, *Experimental Techniques*, **1998**, 22, 19-21.

Story, J. M. Variables Affecting Dome Test Results, *Journal of Applied Metalworking* **1982**, 2, 119-125.

Sutton, M.A., Orteu, J.J., Schreier, H.W. Image Correlation for Shape, Motion and Deformation Measurements, *Springer Science+Business Media*, LLC, New York, USA, **2009**.

Swift, H.W. Plastic instability under plane stress, *Journal of the Mechanics and Physics of Solids*, **1952**, 1, 1-18.

Takashina, K. Relation between the manufacturing conditions and the average strain according to the scribed circle tests in steel sheets, *La Metallurgia Italiana*, **1968**, 18, 757-765.

Takuda, H., Mori, K., Masuda, I., Abe, Y., Matsuo, M. Finite element simulation of warm deep drawing of aluminum alloy sheet when accounting for heat conduction, *Journal of Materials Processing Technology* **2002**, 120, 412-418.

Tebbe, P. A., Kridli, G. T. Warm forming of aluminum alloys: an overview and future directions, *International Journal of Materials and Product Technology* **2004**, 21, 24-40.

Toros, S., Ozturk, F., Kacar, I. Review of warm forming of aluminum–magnesium alloys. *Journal of Materials Processing Technology* **2008**, 207, 1-12.

Van den Boogaard, A.H. Thermally enhanced forming of aluminium sheet – Modelling and experiments, *PhD thesis*, University of Twente, **2002**.

Van den Boogaard, A. H., Huétink, J. Modelling of aluminium sheet forming at elevated temperatures. *Materials Processing and Design: Modeling, Simulation and Applications, NUMIFORM 2004. In: Proceedings of the 8th International Conference on Numerical Methods in Industrial Forming Processes* **2004** vol. 712, *AIP Conference Proceedings*, pp. 893–898.

Van den Boogaard, A. H., Huétink, J. Simulation of aluminum sheet forming at elevated temperatures, *Computational Methods in Applied Mechanical Engineering* **2006**, 195, 6691–6709.

Verma, R. Effect of elevated temperature on mechanical behavior and springback of aluminum alloy brazing sheets *MASc thesis, University of Waterloo* **2016**.

Vegter, H., Dane, C. M. *Proceedings of the 15th Biennial Congress of the International Deep Drawing Research Group, Amsterdam* **1985**.

Voce, E. The relationship between stress and strain for homogenous deformation, *Journal of the Institute of Metals*, **1948**, 74-11, 537-562.

Vogel, J. H., Lee, D. *Journal of Materials Shaping Technology* **1989**, 6, 205-216.

Volk, W., Hora, P. New algorithm for a robust user-independent evaluation of beginning instability for the experimental FLC determination, *International Journal of Material Forming* **2010**, 4, 339-346.

Wilson, D. V. Aluminum versus steel in the family car-The formability factor. *Journal of Mechanical Working Technology* **1988**, 16, 257-277.

www.nhtsa.gov. Retrieved from http://www.nhtsa.gov/Laws+&+Regulations/Vehicles

www.aluminiumleader.com. Retrieved from http://www.aluminiumleader.com/application/transp ort/

www.drivealuminum.org**.** Retrieved from http://www.drivealuminum.org/research-resources/speech-and-presentations/

www.plateandfinheatexchanger.com. Retrieved from http://www.plateandfinheatexchanger.com/sale-2778779-finned-tube-heat-exchanger-automotive-oil-coolers-for-car-transmission.html

www.aluminium-brazing.com. Retrieved from http://www.aluminium-brazing.com/2010/09/cladding-alloys/